Master's thesis

NTNU
Norwegian University of Science and Technology
Faculty of Natural Sciences
Department of Physics

Per Arne Sevle

Multi-Messenger Modelling of Active Galactic Nuclei

Master's thesis in Physics
Supervisor: Foteini Oikonomou
June 2023

NTNU
Norwegian University of
Science and Technology

Per Arne Sevle

Multi-Messenger Modelling of Active Galactic Nuclei

Master's thesis in Physics
Supervisor: Foteini Oikonomou
June 2023

Norwegian University of Science and Technology
Faculty of Natural Sciences
Department of Physics

NTNU
Norwegian University of
Science and Technology

ABSTRACT

Active Galactic Nuclei (AGN) are the most powerful, continuous sources in the Universe. To obtain a deeper understanding of these intricate objects, the entirety of their multi-messenger emissivity needs to be explored. This thesis investigates the cosmic evolution and total energy output of AGN through the use of luminosity functions. We study the luminosity distribution, number density evolution and redshift distribution of AGN sub-populations, and compare their redshift evolution to the star formation rate. It is shown that the luminosity distribution tends to increase with decreasing luminosity and the number density of most sub-populations evolves positively with redshift. Through comparison of the radio, X-ray and gamma-ray source emissivity with the local emissivity of ultra-high energy cosmic rays, it is found that most AGN populations can produce the measured flux. Compared to the diffuse flux of high-energy neutrinos, we find that most AGN populations are sufficient sources assuming their neutrino emissivity is comparable to either X-rays or gamma-rays.

In the second part of this thesis, we investigate the possible emission processes in powerful, high-redshift blazars. Adopting a single-zone model for the non-thermal emission region, we model and fit the spectral energy distribution in accordance with multi-wavelength observations. Introducing to this model a population of ultrarelativistic protons, we estimate the production of secondary neutrinos. It is found to overproduce neutrinos at high energies.

SAMMENDRAG

Aktive galaktiske kjerner (AGN) er de kraftigste, kontinuerlige kildene i Universet. For å oppnå en dypere forståelse for disse intrikate objektene hele deres multi-messenger emissivitet utforskes. Denne avhandlingen undersøker den kosmiske utviklingen og den totale energiproduksjonen til AGN ved bruk av lysstyrkefunksjoner. Vi studerer lysstyrkedistribusjonen, tettheten og rødforskyvningsfordelingen til AGN del-populasjoner og sammenligner deres rødforskyvningsutvikling med stjernedannelseshastigheten. Det er vist at lysstyrkefordelingen har en tendens til å øke med synkende lysstyrke og at talltettheten til de fleste del-populasjonene øker med positiv rødforskyvning. Gjennom sammenligning av radio-, røntgen- og gammastråling emissiviteten til kildene med den lokale emissiviteten av ultrahøyenergi kosmisk stråling er det funnet at de fleste AGN populasjonene kan produsere den lokale fluksen. Sammenlignet med den diffuse fluksen av høyenerginøytrinoer finner vi at de fleste AGN populasjonene er tilstrekkelige kilder under forutsetning av at deres nøytrino-emissivitet kan sammenlignes med enten røntgenstråling eller gammastråling.

I den andre delen av oppgaven undersøker vi mulige utslippsprosesser i kraftige blasarar med stor rødforskyvning. Ved bruk av en enkeltsonemodell for den ikke-termiske utslipp sonen, modellerer og tilpasser vi den spektrale energifordelingen i samsvar med multibølgelengde observasjoner. Ved å introdusere en populasjon av ultrarelativistiske protoner estimerer vi produksjonen av sekundære nøytrinoer. Modellen viser seg å overprodusere nøytrinoer ved høye energier.

ACKNOWLEDGEMENTS

I would like to express my sincerest gratitude to my supervisor, Professor Foteini Oikonomou, for allowing me to work on such an interesting assignment and for her excellent guidance along the way. Her patience and insights have been invaluable throughout the project. I furthermore appreciate her experience and willingness to help with non-thesis-related occurrences, for always being welcoming, and for introducing me to the academic lifestyle.

I would also like to extend my gratitude to Domenik Ehlert and Egor Podlesnyi for answering all my stupid questions, and for helping me put all the pieces together towards the end of this project.

Finally, I would like to thank all my fellow master's students, especially my cosmic ray partner-in-crime Finley Alexander Quinton, for all the memorable moments during these last few months. If we didn't have fun along the way, then what's even the point?

CONTENTS

Abstract i

Sammendrag iii

Acknowledgements v

List of Figures xi

List of Tables xii

1 Introduction 1

2 Non-Thermal Messengers of the High-Energy Universe 3
- 2.1 High-energy photons 3
  - 2.1.1 Diffuse photon fields 3
  - 2.1.2 Gamma-ray propagation 5
- 2.2 High-energy cosmic rays 6
  - 2.2.1 Detection 8
  - 2.2.2 Propagation and interactions 9
  - 2.2.3 Candidate sources 10
- 2.3 Neutrinos 12
  - 2.3.1 Production and interaction 12
  - 2.3.2 Astrophysical neutrinos 14
  - 2.3.3 Neutrino detection 15
  - 2.3.4 Waxman-Bachall bound 17

3 Active Galactic Nuclei 19
- 3.1 AGN classification 19
  - 3.1.1 Radio-quiet AGN 20
  - 3.1.2 Radio-loud AGN 21
- 3.2 AGN unification models 21
- 3.3 AGN regions 24
  - 3.3.1 Accretion disk 25
  - 3.3.2 Broad-line region 29
  - 3.3.3 Dust torus 29
  - 3.3.4 Jet 31

4 AGN Emission Processes **33**
4.1 Blackbody radiation 33
4.2 Non-thermal leptonic processes 34
  4.2.1 Electron spectra 34
  4.2.2 Synchrotron radiation 34
  4.2.3 Synchrotron self-absorption 35
  4.2.4 Inverse Compton radiation 36
4.3 Photomeson processes 38
  4.3.1 Gamma-ray production 38
  4.3.2 Lepton production 40

5 Luminosity Functions and AGN Surveys **43**
5.1 General luminosity function 43
5.2 Radio luminosity function 44
  5.2.1 Radio surveys 45
5.3 X-ray luminosity function 45
  5.3.1 X-ray surveys 47
5.4 Gamma-ray luminosity function 47
  5.4.1 Gamma-ray surveys 48

6 Cosmological Evolution and Multi-Messenger Emissivity **49**
6.1 AGN population evolution 49
  6.1.1 Distance measures 49
  6.1.2 Luminosity distribution and population evolution 50
  6.1.3 Number density and redshift distribution 55
  6.1.4 Redshift evolution 58
  6.1.5 Characteristic luminosity 60
6.2 UHECR emissivity 63
6.3 Neutrino emissivity 65
6.4 Population unification 67

7 High Redshift Blazar emission **69**
7.1 Spectral energy distribution 69
  7.1.1 Flux from the accretion disk and dust torus 69
  7.1.2 Flux from synchrotron emission 70
  7.1.3 Flux from external Compton processes 70
7.2 Data fit 71
7.3 Neutrino production 72

8 Take-Home Multi-Messages **77**
8.1 Conclusion 77
8.2 Future outlook 78

A Coordinate Transformations **79**
A.1 Coordinate transforms 79
A.2 Covariant electrodynamics 80
A.3 Whittaker functions 80

B Supplementary plots **81**

B.1 Luminosity distribution for varying redshift bins 81
B.2 Cosmic ray emissivity at higher redshifts 85

Bibliography **89**

LIST OF FIGURES

2.1 Energy spectrum of the diffuse background light 4
2.2 Spectrum of cosmic rays 7
2.3 *Left:* The Pierre Auger Observatory. 8
2.4 Comparison of the different mechanisms 10
2.5 Adaptation of original Hillas plot 11
2.6 Spectrum of astrophysical (and terrestrial) neutrinos. 15
2.7 *Left:* Illustration of the IceCube observatory. 16

3.1 Images of different AGN. 22
3.2 Illustration of the AGN unification model. 24
3.3 Image showing the different geometries 27

6.1 XLF of two different AGN populations 51
6.2 Luminosity distribution of all considered AGN populations. 53
6.3 Number density (left) and redshift distribution (right) 56
6.4 Density evolution index for different AGN categories 60
6.5 Characteristic luminosity (left) and luminosity density (right) 62
6.6 Emissivity of X-ray source populations 63
6.7 Emissivity of gamma-ray and radio source populations 64
6.8 Predicted neutrino emissivity of all AGN populations 66
6.9 Comparison of number density evolution of X-ray 68

7.1 SED of PKS 0537-286 (left) and PKS 0836+710 (right) 71
7.2 SED after performing the fit to observational data 72
7.3 Production spectra of electrons and photons 74
7.4 The same as for Figure 7.3 but for different values of E_0 75
7.5 Predicted neutrino energy flux on Earth from PKS 0537-286 76

B.1 Luminosity distribution of the non-evolving (left) 81
B.2 The same as for Figure B.1 but for the 2 - 10 keV (left) 82
B.3 The same as for Figure B.1 but for the 14–195 keV blazar (left) 82
B.4 The same as for Figure B.1 but for the 15–55 keV (left) 83
B.5 The same as for Figure B.1 but for the 0.1–300 GeV radio galaxy (left) . . 83
B.6 The same as for Figure B.1 but for the 0.1–100 GeV FSRQ (left) 84
B.7 Cosmic ray emissivity for all X-ray-detected populations at z=0.1 85
B.8 Cosmic ray emissivity for radio and gamma-ray sources at z=0.1 86
B.9 Cosmic ray emissivity for all X-ray-detected populations at z=1 86

B.10 Cosmic ray emissivity for radio and gamma-ray sources at z=1 87
B.11 Cosmic ray emissivity for all X-ray-detected populations at z=5 87
B.12 Cosmic ray emissivity for radio and gamma-ray sources at z=5 88

LIST OF TABLES

6.1 Luminosity ranges considered in the different models 52
6.2 Overview of the fitted parameters for all considered XLF models 54
6.3 Overview of fitted parameters for the considered GLF models 55
6.4 Overview of fitted parameters for all considered RLF models 55
6.5 Density evolution index for all considered models 59

7.1 Parameters used to construct the SED 71
7.2 Parameters modified by the fitting procedure 72

A.1 Relativistic transformations between the host galaxy 79

CHAPTER

ONE

INTRODUCTION

The studies of cosmic rays and neutrinos as complementary messengers to high-energy photons have greatly improved our understanding of astrophysical environments. High energy processes happen in regions possibly opaque to electromagnetic radiation, and thus studying the accompanying different messengers gives insight into previously unavailable regions of the Universe.

High-energy neutrinos and photons are believed to be secondary products of an energetic population of cosmic rays. Therefore, there is reason to believe that the most energetic sources produce all three messengers. Photons and cosmic rays are strongly affected by radiation and magnetic fields both within their source environments and as they traverse through the Universe, whereas neutrinos point directly back to their sources and travel uninterruptedly through the Universe.

Active Galactic Nuclei (AGN) are the most luminous, continuous objects in the Universe. They are powered by a supermassive black hole (SMBH) and are likely sources of high-energy messengers. They are additionally characterised by their broad spectra, stretching over wavelengths from radio to high-energy gamma rays. AGN are persistent over cosmological epochs, and studying their behaviour and energy output can give great insight into the evolution of the Universe in general.

The main goal of this work is to study the correlation between different messengers from AGN. By considering surveys performed by radio, X-ray and gamma-ray telescopes, we will use luminosity functions to explore the behaviour of different AGN categories. Further, we will compare their emissivity to the local flux of ultra-high energy cosmic rays (UHECRs) and the diffuse flux of high-energy neutrinos. Further, a single-zone model for non-thermal radiation from distant AGN will be considered. We will study if purely leptonic emission can explain the observed spectral energy density (SED) of high-redshift blazars and estimate the secondary neutrinos produced by a corresponding population of high-energy protons.

We start out in Chapter 2 by giving an introduction to the non-thermal messengers, including possible sources, propagation processes and modern detectors. In Chapter 3 we thoroughly explore the different regions of AGN and make simplifications required for modelling the SED. Additionally, the morphological differences between different AGN will be reviewed and possible unification schemes will be discussed. Chapter 4 reviews the important physical processes required to produce the full observed AGN spectra. In Chapter 5, we define all the different luminosity functions and the surveys used to construct them. In Chapter 6, we use the luminosity functions to study how different AGN populations evolve in luminosity and number density over cosmological epochs. Additionally, we compare their radio, X-ray and gamma-ray emissivity to the local flux of UHECRs and to the diffuse neutrino flux and finish with a short look at the possibility of unifying some populations. In Chapter 7, we present the results of fitting the SED of high-redshift blazars to our one-zone model and calculate the neutrinos produced through proton-photon interactions. Finally, a conclusion and outlook are given in Chapter 8.

CHAPTER

TWO

NON-THERMAL MESSENGERS OF THE HIGH-ENERGY UNIVERSE

The recent development of telescopes probing higher energy radiation than previously accessible has enabled us to see the Universe in a new light. Through the studies of X-rays and gamma-rays, our understanding of high-energy environments has greatly increased. Complementary, the detection of high-energy neutrinos, cosmic rays and gravitational waves has provided new windows through which we can study powerful, astrophysical processes.

2.1 High-energy photons

Photons are the traditional messenger for astronomical studies. Spanning over 20 decades in energy, they have enabled us to explore large parts of the Universe. With the launch of EGRET in 1991 (Radecke & Kanbach 1992), which was able to detect gamma rays in the 20 MeV-30 GeV range, the first-ever sky survey in gamma rays was performed. Since then, several other sky surveys have been performed in different gamma-ray energies, significantly increasing our understanding of the high-energy Universe.

2.1.1 Diffuse photon fields

Astrophysical processes produce radiation at all wavelengths. The integrated intensity of all the light emitted throughout the entire history of the Universe makes up the total diffuse electromagnetic background. In high-energy astrophysical processes, this background radiation plays an important role in interactions with gamma rays and UHECRs.

Extragalactic background light

The extragalactic background light (EBL) is the combined radiation from astrophysical processes. This includes photons emitted by stars, galaxies and AGN, as well as radiative processes from e.g. dust. The full EBL can be decomposed into constituent radiation fields corresponding to each individual part of the electromagnetic spectrum. The individual parts making up the full EBL are shown in Figure 2.1.

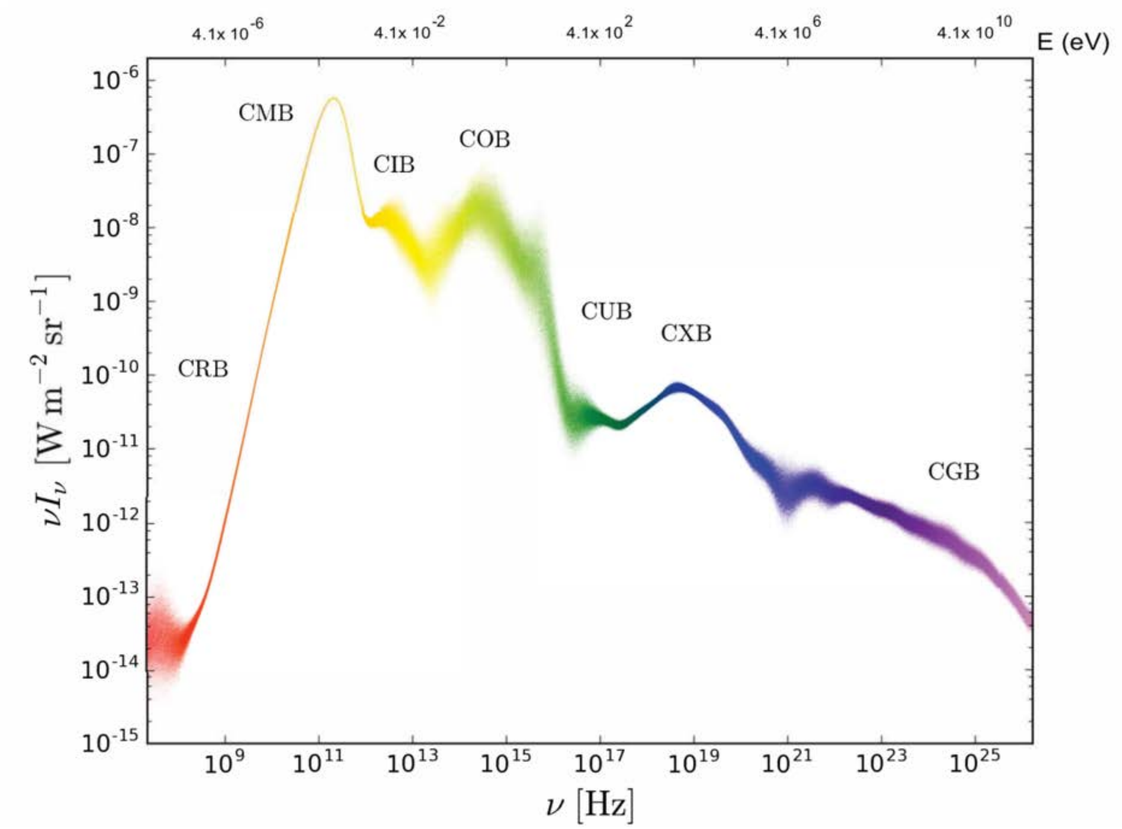

Figure 2.1: Energy spectrum of the diffuse background light at different energies. The full spectrum shows the CMB and the EBL. The thickness of the spectrum corresponds to the uncertainty. Image adapted from Hill et al. (2018).

Cosmic microwave background

The cosmic microwave background (CMB) is the most energetic diffuse radiation field and peaks in the weak IR/microwave range of the electromagnetic spectrum. The CMB is a relic of the early Universe, consisting of light emitted when the Universe first became transparent to radiation. The CMB has been cosmologically redshifted since and has now a thermal spectrum corresponding to a temperature of ∼2.7 K (Fixsen 2009).

Other EBL fields

The cosmic radio background (CRB) consists of all frequencies below 10^{10} Hz. It consists of synchrotron radiation produced by charged particles in diffuse galactic and extragalactic fields along with the steady emission of AGN. The cosmic infrared background (CIB) contains radiation emitted by stars throughout the history of the Universe as well as the radiation emitted by dust that has been heated by stars. The cosmic optical background (COB) consists of the direct emission from stars. The cosmic ultraviolet background (CUB) originates mostly from young, hot stars as well as interstellar nebulae. The cosmic X-ray background (CXB) is generally believed to be dominated by the accretion process around black holes in AGN. These environments are energetic enough that thermal emission is observed in the X-ray range. The final component of the EBL is the cosmic gamma-ray background (CGB), encompassing frequencies above 10^{19} Hz. Its primary contributors are quasars and blazars, as well as supernovae.

2.1.2 Gamma-ray propagation

When traversing intergalactic space, high-energy photons, as well as electrons and positrons, interact with the background radiation fields introduced above. The relevant elementary processes are briefly introduced below.

Pair production

Photons of sufficient energy E_γ undergo pair production when colliding with a background photon of energy E_bg

$$\gamma + \gamma_\mathrm{bg} \longrightarrow \mathrm{e}^+ + \mathrm{e}^-. \tag{2.1}$$

This process limits the mean free path of gamma-rays abiding by the threshold condition (Biteay & Meyer 2022)

$$E_\gamma \geq \frac{2m_\mathrm{e}^2c^4}{E_\mathrm{bg}(1-\cos\theta)} \overset{\theta\,=\,\pi/2}{\approx} 5\times10^{11}\,\mathrm{eV}\left(\frac{E_\mathrm{bg}}{1\,\mathrm{eV}}\right). \tag{2.2}$$

Here, θ is the angle between the momenta of the two photons and m_e is the electron (and positron) mass. As seen from Equation (2.2), the Universe essentially becomes opaque to gamma-rays with energies above $\sim 10^{11}$ eV, whereas gamma-rays with lower energies propagate with close to no interactions with the EBL (Dado & Dar 2015).

Depending on the energy of the gamma-ray photon, it will interact with different parts of the EBL. At energies around 10^{14} eV, interactions with the CMB dominate. At lower energies, interactions with the optical and IR part of the EBL become more important. Going even lower in gamma-ray energy, we see from Figure 2.1 a drastic decrease in energy density for the background radiation field above 1 eV. The secondary electrons again interact with the background radiation fields through inverse Compton scattering.

Inverse Compton scattering

High energy electrons interact with the background photon fields through inverse Compton scattering,

$$\mathrm{e}^- + \gamma_\mathrm{b} \longrightarrow \mathrm{e}^- + \gamma. \tag{2.3}$$

If the energy of the background photon is small, $E_\mathrm{bg} << m_\mathrm{e}c^2$, the inverse Compton scattering proceeds in the Thompson regime. In this case, the energy loss rate of the incident electron is (Longair 2011)

$$\frac{dE}{dt} = \frac{4}{3}\sigma_\mathrm{T} c U_\mathrm{EBL}\left(\frac{v^2}{c^2}\right)\gamma^2, \tag{2.4}$$

where U_EBL is the energy density of the background photon field, σ_T is the Thompson scattering cross section and γ is the electron Lorentz factor.

The combination of pair production and inverse Compton scattering results in electromagnetic cascades for the most energetic photons. These electromagnetic cascades stop when the energy of the secondary photons decreases below the threshold for pair production on the EBL. The inverse Compton process proceeds until the electrons have cooled down to MeV energies.

2.2 High-energy cosmic rays

Cosmic rays consist mainly of elementary particles and some heavier nuclei with energies between 10^9 - 10^{20} eV. The spectrum of cosmic rays follows a power law of the form $dN/dE = E^{-\alpha}$, where the spectral index α varies towards the higher energies, but $\alpha \simeq 2.7$ for $E < 10^{15}$ eV. In this range, the cosmic-ray flux is thought to originate mainly from the Sun, with a composition of both protons and electrons/positrons, but dominated by protons (Zweibel 2013). At energies above 10^{15} eV, the spectrum steepens to $\alpha \sim 3.1$. The break where this transition happens is often called the “knee”. It is thought that this abrupt steepening is the limit of how much acceleration energy can be extracted from supernovae. At energies of about 5×10^{18} eV, the spectrum flattens again, before it drops off at $\sim10^{20}$ eV. This flattening of the spectrum is called the “ankle”, and its cause is still up for debate.

The highest-energy cosmic rays, known as ultra-high energy cosmic rays (UHECRs), are too energetic to be confined by the Galactic magnetic field. There is no consensus on exactly where this galactic-extragalactic transition occurs. Still, the evidence seems to point towards energies of $\sim10^{17}$ eV (e.g. Kachelriess 2019), i.e. below the ankle. Towards the highest energies, the cosmic ray composition seems to favour heavier nuclei, with masses approaching Iron (Kampert & Unger 2012). At present, it is unknown whether the 10^{20} eV cutoff is due to this being the maximum energy available in the cosmic ray accelerators, or if this is a consequence of energy losses as they propagate.

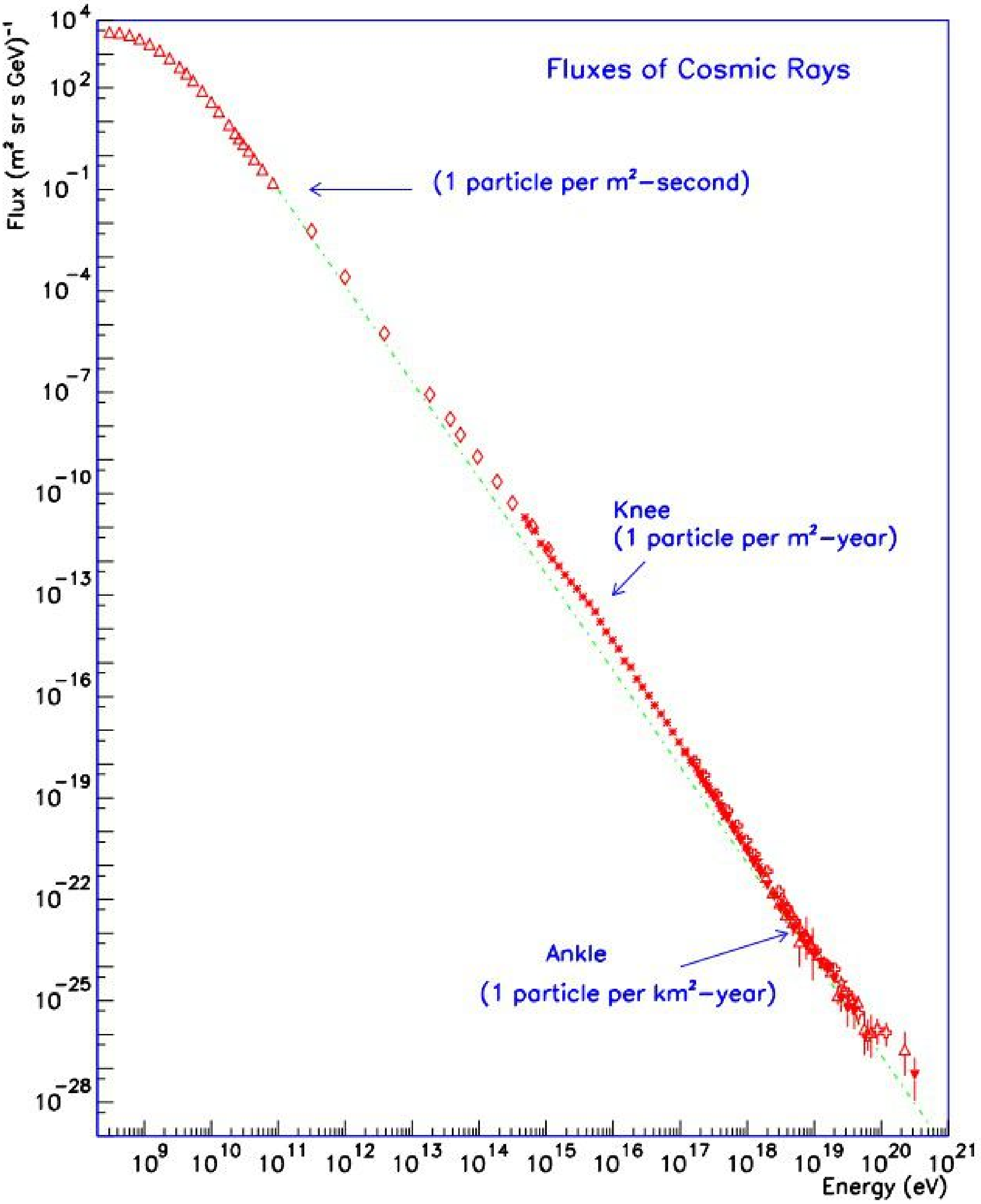

Figure 2.2: Spectrum of cosmic rays as a function of particle energy. The green dotted line shows an E^{-3} power-law for comparison. Image from Bhattacharjee & Sigl (2000), originally adapted from Guérard (1999).

2.2.1 Detection

Cosmic rays of sufficiently large energy are too sparse for us to detect directly. Instead, we rely on the extended air showers created when they interact with the atmosphere. Single high-energy cosmic rays produce extensive cascades of particles that spread over a large area. Since the incident flux at energies above 10^{19} eV is less than one particle per km^2 per year (see Figure 2.2), a large detection area is required to catch enough events.

Current generation UHECR detectors

The Pierre Auger Observatory is the largest cosmic ray detector built to date (Pierre Auger Collaboration 2015). Located in Malargüe, Argentina, the installation is designed to detect UHECR-induced air showers over a 3000 km^2 area. The Observatory consists of 1660 ground-based Cherenkov detectors spread out in a hexagonal grid and 27 fluorescence telescopes at four different sites. Combining these two techniques enables the best reconstruction of cosmic ray air showers yet.

The observatory is designed to detect UHECRs with energy greater than 10^{18} eV with a favourable incident angle. Additionally, Auger has a blind spot on the celestial sphere (Figure 1 in Abreu et al. 2022). It is therefore complemented by the Telescope Array, located in the desert of Utah, USA (Abu-Zayyad et al. 2012). The Telescope Array consists of 507 scintillation ground detectors and 3 fluorescence telescopes over an area of 680 km^2. Together, the Pierre Auger Observatory and the Telescope Array scan the full sky for UHECRs.

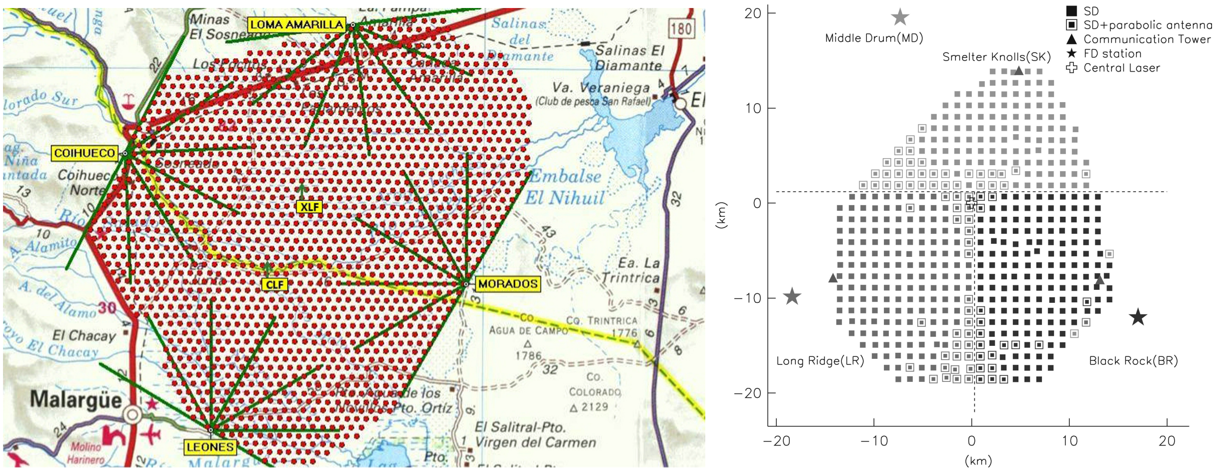
LOMA AMARILLA
COIHUECO
XLF
CLF
MORADOS
LEONES
Malargüe
Embalse El Nihuil
Salinas El Diamante
SD
SD+parabolic antenna
Communication Tower
FD station
Central Laser
Middle Drum(MD)
Smelter Knolls(SK)
Long Ridge(LR)
Black Rock(BR)
20
10
0
−10
−20
(km)
−20
−10
0
10
20
(km)

Figure 2.3: *Left:* The Pierre Auger Observatory. Each red dot corresponds to a water Cherenkov detector. Green lines show the range of the atmosphere fluorescence detectors. Image from Pierre Auger Collaboration 2015. *Right:* The Telescope Array. Squares show the individual scintillation detectors. Stars show the location of the fluorescence detectors. Image from Abu-Zayyad et al. 2012.

2.2.2 Propagation and interactions

Cosmic rays are charged particles and therefore interact with the Galactic and intergalactic magnetic fields. This results in both deflections of arrival directions and time delays when compared to other messengers. As a result of magnetic deflections, cosmic rays detected on Earth would not trace back to their original sources even if we had instruments with sufficient angular resolution. Dependent on the charge of the cosmic ray particle, its energy, and the strength of the magnetic fields, the amount of deflection varies.

Cosmic rays suffer interaction losses depending on their chemical composition. For heavier nuclei, *photodisintegration* becomes relevant. In this process, the cosmic ray interacts with a background photon and decays into lighter nuclei (Stecker & Salamon 1999). In the following section, interactions of UHECR protons will be considered.

Photo-pair production

Similar to the gamma-ray case discussed in Section 2.1.2, protons with sufficiently high energy can produce electron-positron pairs through interactions with the EBL,

$$\mathrm{p} + \gamma_{\mathrm{bg}} \longrightarrow \mathrm{p} + \mathrm{e}^{+} + \mathrm{e}^{-}. \tag{2.5}$$

This is known as the Bethe-Heitler process (Bethe & Heitler 1934) and occurs for proton energies above

$$E_p \geq 10^{18}\,\mathrm{eV}\left(\frac{E_{\mathrm{bg}}}{10^{-3}\,\mathrm{eV}}\right)^{-1}, \tag{2.6}$$

where E_p is the proton energy and E_{bg} is the thermal energy of the EBL. The energy loss through one interaction is relatively small, $2m_{\mathrm{e}}/m_{\mathrm{p}} \sim 10^{-3}$. At energies below the Bethe-Heitler threshold, cosmic rays lose energy only due to the adiabatic expansion of the Universe. At the highest proton energies observed, another process dominates the proton energy loss.

Pion-photo production

The highest-energy protons in the cosmic-ray spectrum have energies above the threshold for pion production. They may therefore collide with photons from the CMB and produce pions through the *Delta resonance*

$$\mathrm{p} + \gamma_{\mathrm{bg}} \longrightarrow \Delta^{+} \longrightarrow \mathrm{n}\pi^{+}/\mathrm{p}\pi^{0}, \tag{2.7}$$

where Δ^{+} is the Delta baryon (see e.g. Workman et al. 2022). This is known as the GZK process, proposed independently by both Graisen (1966) and Zatsepin & Kuz'min (1966). They predicted that the GZK process places an upper limit on the cosmic ray spectrum.

Protons can interact through the Delta resonance with other parts of the EBL, but since the energy density of the CMB is much larger than the rest, interactions with the other background radiation fields are less frequent. If UHECRs are produced at sources far away, the energy loss through the GZK process is significant, as the loss per interaction is $m_{\pi}/m_{\mathrm{p}} \simeq 0.14$. When considering a head-on collision between a proton and a CMB photon, the GZK energy threshold is $E_{\mathrm{p}} \gtrsim 5 \times 10^{19}$ eV. Protons above this energy have an expected energy loss length of ~ 17 Mpc (Kachelriess 2008). Subsequently, the length required for a proton of energy $E_{\mathrm{p}} \gtrsim 10^{20}$ eV to lose enough energy to fall below the GZK threshold is comparable to the distance to M81, the closest galaxy cluster (Karachentsev 2005). This is an important conclusion, as it restricts the sources of the highest energy UHECRs to be in the nearby Universe.

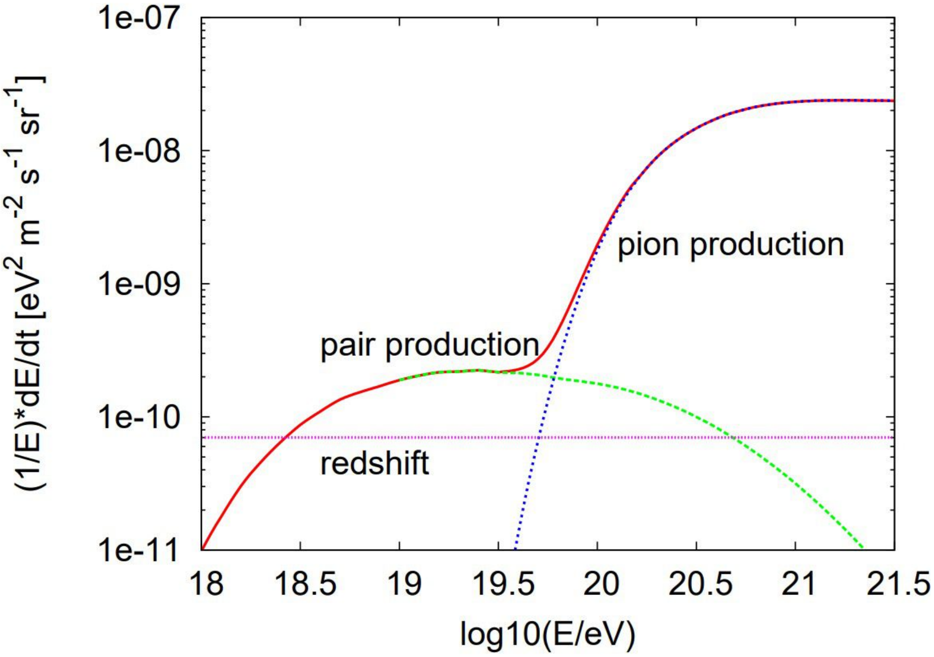

Figure 2.4: Comparison of the different mechanisms contributing to the proton energy loss. Image from Kachelriess 2008.

2.2.3 Candidate sources

For any astrophysical object to be considered a possible source for UHECRs, they both need to accelerate the particles to sufficient energies, as well as be able to contain the charged particles for the duration of the acceleration process. The physics governing the acceleration process is still under investigation, although there exist some well-accepted models like first- or second-order Fermi acceleration (see e.g. Axford et al 1997; Bell 1978; Lichtenberg et al. 1980).

Even without knowing the exact acceleration process, we are still able to put some constraints on the candidate sources for UHECRs. In the relativistic case, the Larmor radius for particles with energy E and atomic number Z is

$$R_{\mathrm{L}} = \frac{E}{ZeB} \approx 1.08\,\mathrm{Mpc}\left(\frac{\mathrm{nG}}{B}\right)\left(\frac{E}{Z \times 10^{18}\,\mathrm{eV}}\right) \tag{2.8}$$

where B is the perpendicular magnetic field strength (equation 1.1 in Kachelriess 2008).

The Larmor radius is crucial when considering a necessary condition for the acceleration of UHECRs known as the *Hillas Criterion* (Hillas 1984). It states that any potential accelerator must have a radius larger than the Larmor radius in order to magnetically confine the particle for the duration of the acceleration process. This criterion relates the

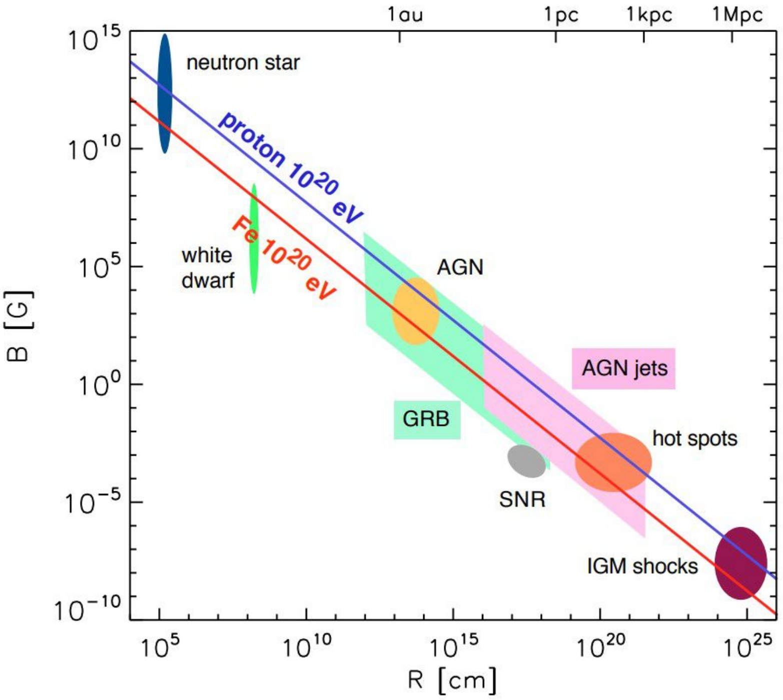

Figure 2.5: Adaptation of original Hillas plot for proton (blue line) and iron nuclei (red line) energy. Only sources above the blue (red) line can confine protons (iron nuclei) with energy 10^{20} eV. The region covered by each source corresponds to the uncertainty in their parameters. Image from Kotera & Olinto (2011).

magnetic-field strength B with the radius R and gives the maximal achievable energy as

$$E_{\max} \leq qBR \approx 1\,\mathrm{EeV} \times Z \times \left(\frac{B}{1\,\mu\mathrm{G}}\right)\left(\frac{R}{1\,\mathrm{kpc}}\right). \tag{2.9}$$

Categorization of different astrophysical sources according to the Hillas criterion is shown in Figure 2.5. The main astrophysical environments that can be considered accelerators of UHECRs are neutron stars, gamma-ray bursts (GRBs), active galactic nuclei and shocks in the intergalactic medium (IGM). In the following, we will shortly comment on each of these candidates.

Neutron stars

Neutron stars have for some time been candidates for UHECRs (Gunn & Ostriker 1969). Some neutron stars, known as pulsars, are quickly rotating, strongly magnetized and produce relativistic outflows. These young neutron stars can accelerate particles to the required energy scales (Blasi et al. 2000). Additionally, work done by Fang et al.(2012) shows that the UHECR Auger spectrum and composition can be reasonably well explained by a population of extragalactic pulsars. A significant neutrino flux is expected to accompany the UHECRs produced in pulsar outflows. However, the possibility of pulsars being the dominant UHECR source population has been ruled out by the upper limits of the diffuse neutrino flux determined by IceCube (Fang et al. 2016).

Gamma-ray bursts

Gamma-ray bursts are the most luminous events in the Universe but last only very briefly. Recently, the brightest gamma-ray burst ever was detected (Malesani et al. 2023), with an isotropic energy release of $E_{\mathrm{iso}} > 5 \times 10^{54}$ erg. Some of this energy was released in the form of gamma rays, and if a comparable amount of energy goes into the production of cosmic rays, GRBs can explain the detected diffuse UHECR flux. UHECRs produced in GRBs should interact in their immediate surroundings and produce neutrinos. Due to GRBs being transient objects, it should be possible to detect neutrinos in coincidence with gamma-ray signals from the same event (Aartsen et al. 2015). The arrival of UHECRs is significantly delayed and therefore not expected in coincidence. GRBs have also been ruled out as a dominant source for high-energy neutrinos (Aartsen et al. 2017).

Active galactic nuclei

AGN are the most powerful continuous objects in the Universe. They are located at the centre of some galaxies and are characterized by their strong non-thermal emission. AGN as sources for UHECRs as well as other high-energy messengers is the main focus of this thesis and will be more thoroughly explained in Chapter 3.

Shocks in the intergalactic medium

The largest structures in the Universe are galaxy clusters and filaments (e.g. Springel et al. 2006). The acceleration of gas within these structures produces shocks likely capable of accelerating cosmic rays. With sufficient magnetic field strength, the size of these regions can confine UHECRs with energies of 10^{21} eV (Norman et al. 1995).

2.3 Neutrinos

Neutrinos are subatomic particles belonging to the leptonic sector of the standard model. They are split into three generations based on mass, similar to their companion heavier leptons (e, μ, τ). For more details on neutrino physics, see Athar et al. 2022.

2.3.1 Production and interaction

In this section, we will review some of the processes that produce neutrinos at different energies.

Nuclear interactions

Neutrinos were first discovered by studying the energy released in radioactive decay (Cowan et al. 1956). The typical weak interaction resulting in neutrino production is the β^--decay

$$\mathrm{n} \longrightarrow \mathrm{p} + \mathrm{e}^- + \bar{\nu}_\mathrm{e}. \tag{2.10}$$

The β^--decay happens in neutron-rich environments, like the nuclei of heavier elements. The ”opposite” reaction, $\mathrm{p} \longrightarrow \mathrm{n} + \mathrm{e}^+ + \nu_\mathrm{e}$, is also possible and is known as the β^+-decay. Other processes, like electron capture (Bambynek et al. 1977), also contribute to the production of neutrinos.

These three processes all occur within atomic nuclei, where the total energy released is represented by the Q-value (p.380-381, Krane 1988). The Q-value is determined by the binding energy in the atomic nuclei, and as a result, the kinetic energy of the neutrino released cannot exceed the binding energy of the nuclei and therefore must be below a few MeV.

Hadronic processes

The production of high-energy neutrinos happens through the interactions and decay of hadrons in energetic environments. The interactions of protons with ambient radiation and matter fields produce neutrinos through decays of secondary neutrons and pions.

The largest contributor to the neutrino flux at Earth is the proton-proton chain occurring in the sun (Bahcall 1964). This produced a neutrino flux reaching $\sim 10^{13}$ GeV^{-1} sr^{-1} s^{-1} cm^{-2} (see Figure 2.6). The energies of these neutrinos however are limited to a few hundred keV.

Higher energy neutrinos are produced in decays of pions. In proton-rich environments, the dominant pion production reaction is

$$\mathrm{p} + \mathrm{p} \longrightarrow \begin{cases} \mathrm{n} + \mathrm{p} + \pi^+ \\ \mathrm{p} + \mathrm{p} + \pi^+ + \pi^- \\ \mathrm{p} + \mathrm{p} + \pi^0 \end{cases} . \tag{2.11}$$

At energies above $\sim$ GeV however, intermediate delta-baryons are produced through their corresponding resonances and this process becomes more complicated. In photon-rich environments, another process starts to dominate proton cooling, namely proton-photon interactions.

Protons with sufficient energy interact with ambient radiation fields through the Δ^+-resonance leading to photomeson production. The full Δ^+-resonance is, similar to Equation (2.7),

$$\mathrm{p} + \gamma \longrightarrow \Delta^+ \longrightarrow \begin{cases} \mathrm{p} + \pi^0 + \xi_0(\pi^0) + \xi_\pm(\pi^+ + \pi^-) \\ \mathrm{n} + \pi^+ + \xi_0(\pi^0) + \xi_\pm(\pi^+ + \pi^-) \end{cases} , \tag{2.12}$$

where ξ is the number of pions produced, also known as the pion multiplicity (see e.g. Adam et al. 2016). It is close to zero at low energies and increases at higher energies.

The secondaries of pγ- and pp-interactions are predominantly neutrons, protons and pions. With sufficient proton energies, heavier mesons like kaons and eta mesons are possible products, however, their production rate is quite low and neutrinos produced in their decay are not detectable by current observatories (Asano & Nagataki 2006). Secondary protons can escape the source environment as cosmic rays, or be confined and continue to suffer energy losses through repeated hadronic interactions, creating more pions. Secondary neutrons also lose energy through photomeson production, similar to Equation (2.12), resulting in further pion production.

The pions created in these reactions will subsequently decay into neutrinos, along with other particles. Pions decay through the weak force into muons and neutrinos through

$$\begin{cases} \pi^+ \longrightarrow \mu^+ + \nu_\mu \\ \pi^- \longrightarrow \mu^- + \bar{\nu}_\mu \\ \pi^0 \longrightarrow 2\gamma \end{cases} . \tag{2.13}$$

From this, we see that charged pions contribute to the cosmic neutrino flux, whereas neutral pions contribute to the emission of gamma-ray sources, as well as the CGB.

Processes such as the Bethe-Heitler process Equation (2.5), gamma-ray pair production and annihilation must all be taken into account when studying hadronic interactions in high-energy astrophysical environments, as they should all be present for sources producing both gamma-rays, cosmic rays and neutrinos. Muons produced by decaying pions subsequently decay themselves through

$$\begin{cases} \mu^+ \longrightarrow \mathrm{e}^+ + \nu_\mathrm{e} + \bar{\nu}_\mu \\ \mu^- \longrightarrow \mathrm{e}^- + \bar{\nu}_\mathrm{e} + \nu_\mu \end{cases} , \tag{2.14}$$

producing more neutrinos that contribute to the diffuse neutrino flux.

Neutrino interactions

As seen in the previous section, only electron and muon neutrinos are produced in hadronic decays. However, as neutrinos propagate through space, they oscillate between the different flavour states. This phenomenon is known as *neutrino oscillations* (Schwetz et al. 2008). As a consequence, the detected flux of neutrinos is more evenly divided between the different flavours than what is to be expected from pion decay. For instance, the initial neutrino flavour ratio $\nu_\mathrm{e} : \nu_\mu : \nu_\tau \simeq 1 : 2 : 0$ evolves into a mix of all three flavours $\nu_\mathrm{e} : \nu_\mu : \nu_\tau \simeq 1 : 1 : 1$ by the time it reaches our detectors (Farzan & Smirnov 2008).

High-energy neutrinos interact with matter mainly by inelastic scattering off nucleons. The neutrinos exchange neutral Z or charged W bosons through weak interaction with quarks in the target nucleus. These processes are referred to as *neutral currents* and *charged currents* respectively (Ahlers & Halzen 2018). In both cases, the struck nuclei do not remain intact but rather initiate hadronic showers measurable with Cherenkov detectors, similar to cosmic ray-induced air showers (Section 2.2.1).

2.3.2 Astrophysical neutrinos

The search for neutrinos from extra-terrestrial sources has been ongoing since the first detection of solar neutrinos in the late 1960s (Bahcall 1969). Astrophysical neutrinos span large orders in both energy and observed flux, as can be seen in Figure 2.6.

Similar to the CMB, there exists also a cosmic neutrino background (CνB). Whereas the CMB dates from when the universe was roughly 380,000 years old (Fixsen 2009), the CνB decoupled from the matter only two seconds after the Big Bang (Athar et al. 2022). These neutrinos are sometimes referred to as relic or cosmological neutrinos and peak at energies of $\sim 10^{-4}$ eV, far below the sensitivity of current generation neutrino detectors.

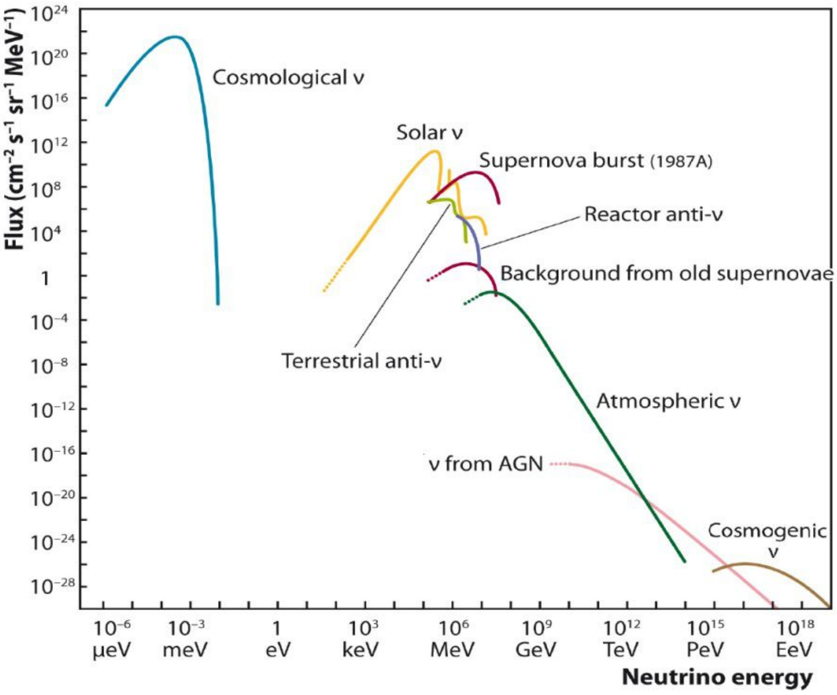

Figure 2.6: Spectrum of astrophysical (and terrestrial) neutrinos. The lowest energy component is the CνB. Solar neutrinos are shown at keV-MeV energies and supernovae (SN) neutrinos at slightly higher energies. The atmospheric neutrinos dominate at energies above GeV. The UHE neutrinos ($\geq 10^5$ GeV) are presumably produced in the most energetic sources known, like GRBs or AGN. The highest-energy neutrinos are the cosmological neutrinos created by propagating cosmic rays. Image from Spiering (2012).

Atmospheric neutrinos are neutrinos created in cosmic-ray air showers. When UHECRs interact with the upper atmosphere, large cascades of secondary pions, kaons and muons are created, which decay into neutrinos (Gaisser et al. 1978). The spectrum of atmospheric neutrinos follows the energy spectrum of UHECRs and thus spans many orders in magnitude. Differentiating extragalactic neutrinos from the background of atmospheric neutrinos is one of the biggest challenges of high-energy neutrino detectors like IceCube (see Section 2.3.3).

At the very end of the neutrino spectrum in Figure 2.6, we find the cosmogenic neutrinos. These are the neutrinos produced when UHECRs interact with the EBL whilst propagating in intergalactic space. These neutrinos should be extremely energetic, as they carry away a significant fraction of the original proton energy. The extremely low flux makes these neutrinos also undetectable with current observatories.

2.3.3 Neutrino detection

Current and future-generation neutrino detectors look for neutrinos by detecting the light emitted by secondary particles. As neutrinos only interact through the weak force, their interaction cross sections, and consequently the probability of interaction, is very low. Due to the low interaction probability, neutrino detectors need to cover a large volume in hopes to catch a few events. Previous and ongoing water Cherenkov detectors (e.g. the

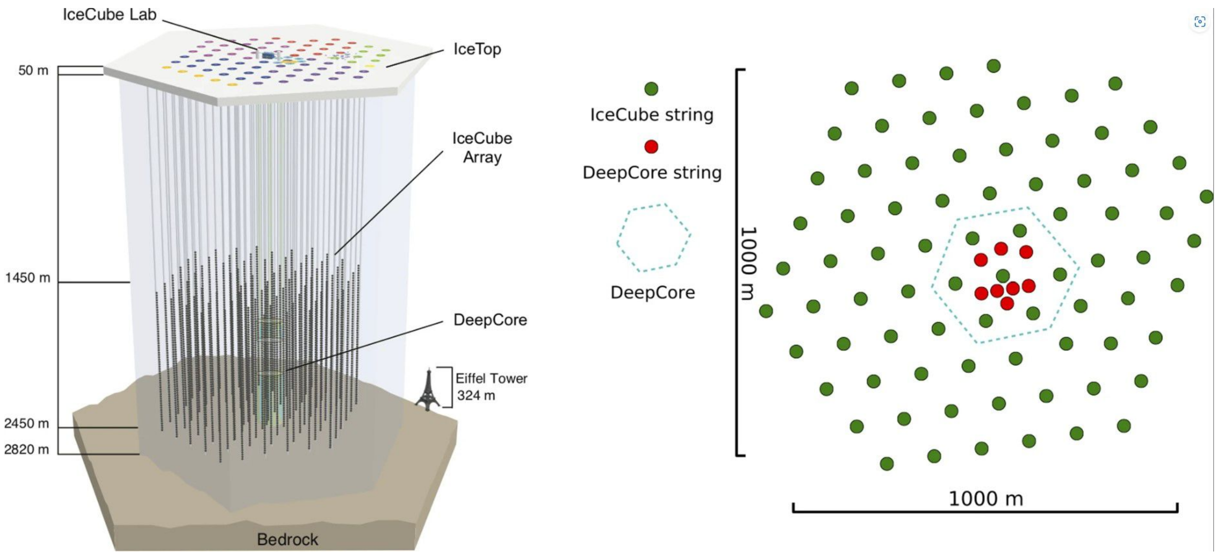

Figure 2.7: *Left:* Illustration of the IceCube observatory. To each of the 86 strings, there are attached 60 PMTs. *Right:* Distribution of string seen from above. Each green dot corresponds to a standard IceCube string, separated by a distance of 125 m, and the red ones show a more densely packed photomultiplier section with higher efficiency. Image from Ahlers et al. (2018).

Super-Kamiokande or AMANDA detector, Fukuda et al. 2003; Andres et al. 2001) have had great success in detecting terrestrial, solar, atmospheric and Galactic SN neutrinos.

IceCube

The largest neutrino observatory to date is the IceCube Neutrino Observatory. The aptly named observatory is located at the South Pole and monitors a cubic kilometre of Antarctic ice looking for neutrinos from 0.1 TeV to 1 EeV. The detector consists of 5160 optical sensors spread across 86 strings submerged in the antarctic ice between 1450 m and 2450 m deep. Each string holds 60 optical modules containing a photomultiplier. Being located at the south pole, IceCube looks for neutrinos predominantly from the northern hemisphere.

The first important result from IceCube was the confirmation of extragalactic neutrinos (IceCube Collaboration 2013). Since then, many more extragalactic neutrinos have been detected, including one neutrino in 2017 in coincidence with a flaring blazar (Aartsen et al. (2018)), indicating blazars as strong candidates for neutrino production. IceCube has provided the best and only estimate on the diffuse neutrino flux to date, estimating a best-fit flux spectrum for astrophysical neutrinos of

$$\Phi_\nu = 1.44 \times 10^{-18}\,\mathrm{GeV}^{-1}\mathrm{cm}^{-2}\mathrm{s}^{-1}\mathrm{sr}^{-1} \tag{2.15}$$

in the 15 TeV to 5 PeV energy range (Abbasi et al. 2022).

Whereas IceCube is observing the northern sky, the southern sky remains to be observed by a modern, large-scale neutrino observatory. However, this unbalance is close to being fixed by a cubic-kilometre observatory under construction in the Mediterranean

Sea, named *KM3NeT* (Adrián-Martínez et al. 2016). The KM3NeT will also bring an improved resolution and energy range compared to IceCube, bringing neutrino astronomy another step forward.

2.3.4 Waxman-Bachall bound

In 1998, Eli Waxmann and John Bachall predicted a model-independent upper bound on the high-energy diffuse neutrino flux (Waxman & Bachall, 1998). Assuming neutrinos are created in the same source environments as cosmic rays and that the sources are not much larger than the proto-meson (or proton-proton) mean-free-path, they showed that the observed extragalactic cosmic rays imply a neutrino flux of

$$E_\nu^2 \Phi_{\nu_\mu} \approx 1.5 \times 10^{-8} \xi_\mathrm{z} \mathrm{GeV cm^{-2} s^{-1} sr^{-1}}. \tag{2.16}$$

The ξ_z term describes the possible contribution of unobserved sources and accounts for the cosmological energy loss of the neutrinos and is close to unity.

Modern research and observations favour high-energy neutrinos to be produced in astrophysical environments opaque to both high-energy cosmic rays and gamma rays. One would therefore expect to dismiss this prediction. However, this upper neutrino limit matches the recently predicted diffuse neutrino by IceCube, Equation (2.15), almost perfectly. Whether this is simply a coincidence or if we need to consider the Waxmann-Bachall arguments a serious constraint on the diffuse neutrino flux remains inconclusive.

CHAPTER

THREE

ACTIVE GALACTIC NUCLEI

Some galaxies show a significant increase in energy emitted from a tiny region located at the centre of the galaxy. These galaxies are said to be active and are relatively sparse in the local universe. The compact, luminous region located at the centre of active galaxies is called an active galactic nucleus (AGN). This region outshines the entire host galaxy in multiple parts of the electromagnetic spectrum. The radiation produced by an AGN can be orders of magnitude greater than the host galaxy, making AGN the brightest continuous objects in the universe.

At the centre of all AGN, there resides a supermassive black hole (SMBH) with an accretion disk. The SMBH and its accretion disk are often referred to as the *central engine*. The central engine is often surrounded by a region of relatively dense clouds called the broad line region (BLR) contained within about 0.1 pc from the SMBH. The BLR is responsible for the broad emission lines visible in the optical spectra of AGN. The central engine and BLR are surrounded by an optically thick torus of dense dust and molecular gas. Beyond the dust torus, at a distance up to $\sim$1 kpc from the nucleus, a less dense region of gas clouds known as the narrow line region (NLR) orbits the SMBH. The NLR is responsible for the narrower emission lines in the optical spectra (FWHM $\lesssim 10^3$ km s^{-1}). Finally, in some cases, powerful, collimated jets are observed extending from the central engine to beyond even the host galaxy.

Section 3.1 introduces the different types of AGN and the differences between them. Then, Section 3.2 presents a possible unified view of the different AGN categories. Finally, in Section 3.3, the individual parts of AGN are explored in more detail and the extent of their contribution to the energy density of the external photon fields relevant for the non-thermal processes of Chapter 4 is derived.

3.1 AGN classification

As is the case for most astrophysical objects, differences and classifications of AGN are based on observations. Emissions from AGN span almost 20 orders of magnitude, with wavelengths ranging from radio to gamma rays. As a consequence, observations in different wavebands have led to multiple different classification schemes. In the following, we will adopt a simple and commonly used classification based on radio and optical studies (Tadhunter 2008). Based on observations in the optical band, AGN can be split into three categories.

Type-I

Type-I AGN shows two distinct sets of emission lines in their spectra. A narrower set consisting mainly of forbidden lines with widths of ∼400 km/s, and a set of broader emission lines with widths reaching ∼10,000 km/s.

Type-II

Type-II AGN only shows prominent narrow lines. The broad lines are either absent or very weak in the optical spectra.

This Type-I/II classification is not absolute as we observe AGN that seems to have some broad line emission, but not enough to be strictly classified as a Type-I. The Type-I/II classification should instead be considered as the extreme ends of a range of AGN (see e.g. Singh et al. 2011).

Although Type-I/II should be considered the main optical classification, there are some AGN that fit neither of them. These AGN are known as Type-0, and show in some cases show no emission lines at all. The defining feature of Type-0 AGN is their rapid variability at optical wavelengths.

A second broad distinction can be found by considering their radio emissions instead. Sources with a high radio flux are called radio-loud, whereas sources with weaker emission in the radio band are said to be radio-quiet.

3.1.1 Radio-quiet AGN

AGN that does not show particularly strong radio emissions are said to be radio-quiet. Since radio emission comes mainly from the extended jets, these galaxies were for a long time thought to be jet-less. More recent work has however shown that also the radio-quiet AGN host jets (see e.g. Ghisellini et al. 2004), but they do not extend beyond the host galaxy.

Radio-quiet AGN are the largest group of active galaxies and are split into two main subgroups. Seyfert galaxies are the most numerous type of active galaxy and account for about 10% of all galaxies (Maiolino & Rieke 1995). Seyfert galaxies are further split into two subcategories based on the optical Type-I/II scheme, namely Seyfert 1 and Seyfert 2, respectively. The morphology of the Seyferts host galaxy is predominantly found to be either spiral or irregular.

The second category of radio-quiet AGN is radio-quiet quasars. Their spectra resemble that of Seyfert 1-type galaxies but with much greater core luminosity. Whereas Seyfert galaxies dominate the local population of AGN, quasars are usually found at higher redshifts, meaning they must be quite luminous in order for us to observe them. As a result of their large redshift and luminous core, studying the properties of their host galaxy is challenging, as it is often not resolvable. Although a satisfactory correlation between quasars and their host galaxy is yet to be found, observations show that the most luminous quasars, both radio-quiet and radio-loud, tend to reside in massive elliptical host galaxies (Dunlop et al. 2003).

3.1.2 Radio-loud AGN

Radio-loud AGN are active galaxies that show a large and extended jet structure. The collimated jets powered by the central engine extend far beyond the host galaxy, ending in large radio lobes. These regions, as well as the jet itself, radiate strongly in the radio band. Radio-loud AGN are divided into two main categories, radio galaxies (RG) and blazars.

Radio galaxies

Radio galaxies dominate the sky at radio wavelengths. Similar to Seyfert galaxies, radio galaxies can be divided into broad-line radio galaxies (Type-I) or narrow-line radio galaxies (Type-II) based on their optical spectra. Narrow-line radio galaxies can be further distinguished based on the structure of their extended radio jets. A jet is said to be edge-darkened if the brightest radio emissions occur in brightened regions along the jet or close to the supermassive black hole. If the radio emission is relatively weak close to the core, but very bright in the end lobes, the jet is edge-brightened. Radio galaxies with edge-darkened jets are classified as a Fanaroff-Riley I (FRI) radio galaxy, and radio galaxies with an edge-brightened radio structure are known as an FRII type (Fanaroff & Riley 1974a).

In addition to the two main FR categories, recent work has shown there exists a third category called FR0. FR0 are less powerful than their FRI/FRII counterpart and are limited in their jet structure, but in turn, are much more numerous in the local universe (Baldi et al. 2019).

The more powerful Type-I radio bright AGN are known as radio-loud quasars. Based on the shape of their radio spectra, they are classified as either steep spectrum radio quasars (SSRQ) or flat spectrum radio quasars (FSRQ). FSRQs tend to be more core dominant than the often lobe-dominant SSRQ, and show greater variability in the optical spectra.

Blazars

The final type of radio-loud active galaxies is blazars. Blazars show high variability in their optical spectra and are classically split into BL Lacertae (BL Lac), which show weak or no emission lines in their optical spectra, and what used to be referred to as optical violent variables (OOV), which show broad optical spectral lines. OOV blazars and other old blazar categories have essentially become unified with FSRQs (Urry & Padovani 1995), and for the work performed in this thesis, we will consider BL Lacs and FSRQs as blazar sub-populations.

3.2 AGN unification models

The two types of classification discussed in the previous section were based on optical and radio emissions. By considering different wavelengths, other classifications arise in

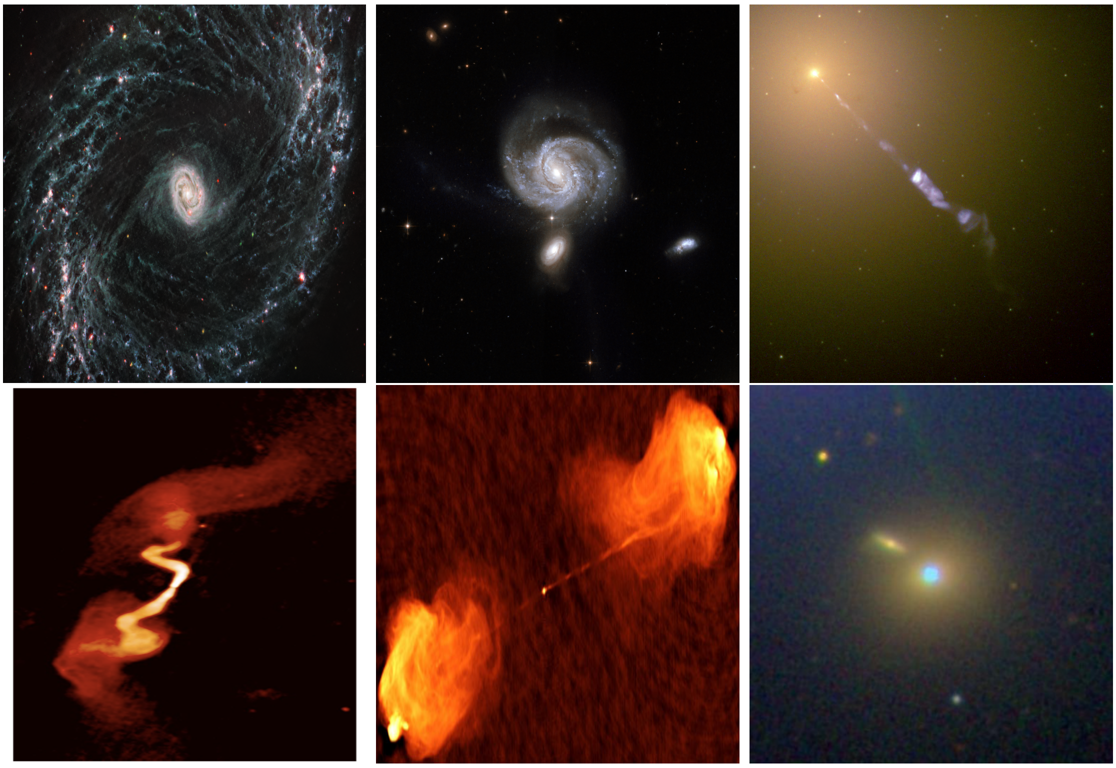

Figure 3.1: Images of different AGN. *Upper left*: Seyfert galaxy NGC 1433 imaged by NASA/ESA/CSA James Webb Space Telescope. *Upper center*: Optical image of Seyfert 2 type galaxy NGC 7674, also known as Markarian 533. Image credit ESA/Hubble. *Upper right*: Radio galaxy M87 and its extended jet. Image by NASA and the Hubble Heritage Team (STScl/AURA). *Lower left*: 1.4 GHz Very Large Array (VLA) radio image of FRI radio galaxy 3C 31 with jet plumes extending to 300 kpc from the center of the galaxy. Image courtesy of NRAO/AUI. *Lower center*: VLA observation of FRII type radio galaxy Cygnus A. Image credit NRAO/AUI. *Lower right*: One of the closest blazars, Markarian 421, located in the Ursa Major installation. Image from the Sloan Digital Sky Survey (SDSS).

conflict with these two. The lack of an absolute classification capable of distinguishing different types of AGN from one another has led to the possibility for AGN unification models (e.g. Singh et al. 2011; Urry 2004).

The most successful radio-loud unification model (Urry & Padovani 1995) argues that the inclination angle of the extended jet axis to our line of sight, in addition to the efficiency of the central engine, determines what type of AGN we observe. For a radiatively efficient central engine, if the jet axis is pointed along our line of sight, i.e. the observation angle $\theta \sim 0°$, we see a blazar. Increase the viewing angle and we would observe a Type-I radio galaxy, and as the viewing angle approaches 90°, a Type-II radio galaxy would be observed. In this type of AGN model, the dust torus plays an important role. It is assumed to be optically thick, and thus, if viewed edge-on, the central engine and BLR emission will be obscured, and only narrow lines characteristic of a Type-II AGN will be observed. By reducing the viewing angle, more and more of the central regions will come into view, and the emission from the accretion disk and the BLR will be visible in addition to the narrow line emission and a Type-I AGN will be observed. At the smallest of viewing angles, the bulk motion of the plasma in the jet is beamed and the strong anisotropic radiation of the BL Lacs and the more powerful FSRQs are observed (Blandford & Königl 1979). If the AGN hosts a less efficient central engine, the structure of the accretion disk could be different, and a broad-line-emitting region could be completely absent (Heckman & Best 2014).

The FRI/FRII radio galaxy categories can also be made sense of in such a unification model. The FRII radio galaxies are considered to be the unbeamed counterparts of the FSRQ population, i.e. viewed at larger angles, and the FRI radio galaxies, with their less powerful jets, are the same objects as the BL Lac population but viewed at larger angles (Antonucci & Ulvestad 1985).

A similar unification model is applicable to the radio-quiet AGN populations as well. As these objects show no large extended jet structure, they only differ by what is obscured by the dust torus. Viewing a radio-quiet AGN close to edge-on, one would observe a Seyfert 2 AGN as the emission of the central engine and the BLR are hidden by the dust torus. Decreasing the viewing angle, the BLR and accretion disk radiation would come into view, and a Seyfert 1 AGN is observed. The radio-quiet quasars would then be the equivalent of a Seyfert-type AGN just viewed at an angle where all the core emission is detectable and overpowering the host galaxy. A summary of these unification models is found in Figure 3.2, showing all different AGN as a result of whether or not it possesses an extended jet, the viewing angle of the observer and the radio power of the source. These aforementioned models show that depending on the viewing angle, the radio power of the sources and the accretion efficiency (greater accretion efficiency is thought to launch more powerful, extended jets Tchekhovsky et al., 2011), all AGN sources essentially have the same physical nature.

Another unifying sequence known as the *blazar sequence* was introduced in 1998 with the intent of unifying the observed broad-band emission from different blazars (Ghisellini et al. 1998). The blazar sequence looks for physical connections based on the shape of the full spectral energy distribution. Even though the blazar sequence has been successful in some regards, regularly updated blazar catalogues at different wavelengths have caused the blazar sequence to constantly adapt and change with the improved observations. There is, as of today, no definite conclusion as to whether the blazar sequence is related to the physical processes in blazars, or if it is nothing more than an artefact of imperfect observations.

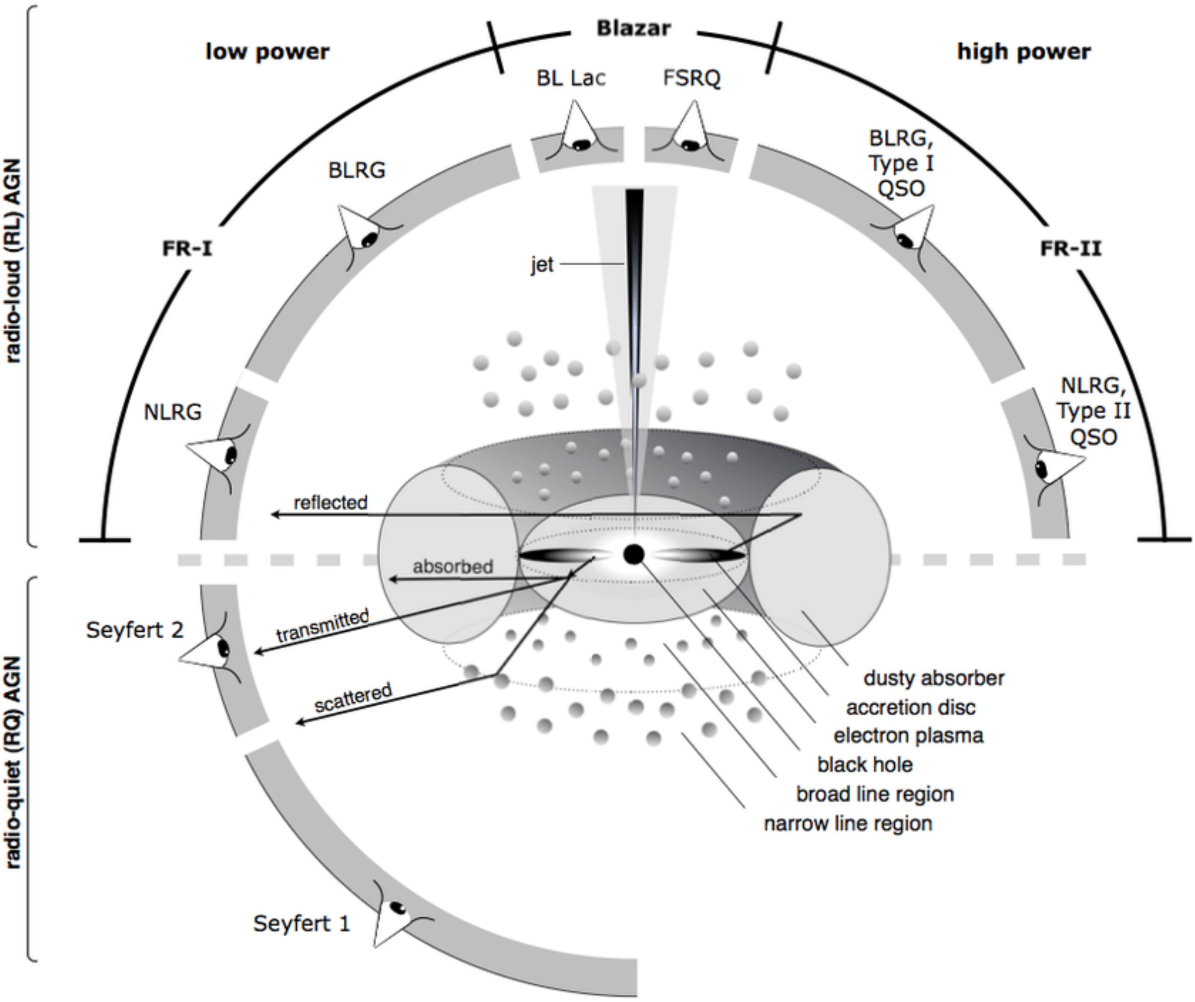
radio-loud (RL) AGN
radio-quiet (RQ) AGN
low power
Blazar
high power
BL Lac
FSRQ
BLRG
BLRG, Type I QSO
FR-I
FR-II
jet
NLRG
NLRG, Type II QSO
reflected
absorbed
transmitted
scattered
Seyfert 2
Seyfert 1
dusty absorber
accretion disc
electron plasma
black hole
broad line region
narrow line region

Figure 3.2: Illustration of the AGN unification model. The model shows that the different types of AGN are physically similar and the different categories are an artefact of our viewing angle, whether or not the AGN produces a significant jet and the power of the central engine. Note that strong radio sources are generally observed to have opposite jets. Figure not to scale. Image from Beckmann & Shrader (2013).

3.3 AGN regions

AGN consist of multiple distinct regions which all play an important role in understanding the total emission picture. In what follows, we will consider the blackbody emission from both the accretion disk and the dust torus, as well as the line emission from the BLR, to play an important role in the IR and optical range of the SED. Additionally, high energy non-thermal radiation will be considered to originate in a spherical plasmoid, hereafter referred to as the emitting "blob", located within the jet. The physical processes within the blob responsible for most of the SED is synchrotron, synchrotron self-Compton and inverse Compton interactions, and will be discussed in more detail in Chapter 4.

The inverse Compton process requires an external field of seed photons. The three most important sources for this external radiation field are the accretion disk, the BLR and the dust torus[1]. The following section introduces these regions and their contribution to the total energy density of this radiation field.

In the following derivations, we adapt the notation of Dermer & Menon (2009). The dimensionless energy is given as $\epsilon = h\nu/(m_\mathrm{e}c^2)$, where ν is the photon frequency, $m_\mathrm{e}c^2$ is the electron rest energy and h is the Planck constant. A semicolon within function arguments will be used to differentiate between differential variables and parameters. Additionally, differentials will be marked with an underline, e.g. for the spectral energy density, we write

$$\underline{u}(\epsilon, \Omega; r) d\epsilon d\Omega \equiv \frac{\partial u}{\partial\epsilon\partial\Omega}(r) d\epsilon d\Omega. \tag{3.1}$$

3.3.1 Accretion disk

The central black hole exerts a massive gravitational pull on stellar material close to the galactic centre. Due to the conservation of angular momentum, surrounding matter spirals inwards and forms a disk around the black hole. This process is known as accretion, and the disk of orbiting material is called an accretion disk. If the accretion disk reaches high enough densities, viscous processes start to consume angular momentum and heat up the disk, causing it to thermally radiate strongly in UV- and X-rays. The *accretion efficiency* η is defined as the fraction of the infalling particles' rest mass energy converted into radiation through the accretion process. Denoting the *mass accretion rate* by $\dot{m}$, we can express the total luminosity of the accretion disk as

$$L_\mathrm{disk} = \eta \dot{m} c^2, \tag{3.2}$$

where c is the speed of light.

Accretion disk luminosity is bound by an upper limit, known as the *Eddington luminosity* (Eddington 1925). It was derived by balancing the gravitational force with the radiation pressure on the infalling particles (see e.g. Dermer & Menon (2009), eq. 6.133) and reads

$$L_\mathrm{Edd} \equiv \frac{4\pi c G M m}{\sigma_\mathrm{T}} \simeq 1.26 \times 10^{38} \frac{M}{M_\odot} \mathrm{erg\ s^{-1}}, \tag{3.3}$$

where M is the mass of the black hole, $m = m_\mathrm{p} + m_\mathrm{e}$ is the mass of the infalling particles, and σ_T is the Thomson cross section.

If the accretion rate surpasses its Eddington limit, the increased radiation pressure will blow away any excess infalling gas, halting the accretion process. By equating the disk and Eddington luminosities, we find that the accretion efficiency for a Schwarzschild black hole is $\eta \simeq 1/12$.

Despite the Eddington luminosity placing an upper limit on all luminous objects, super-Eddington accretion is physically possible for extended periods if the accreting matter is optically thick or if the escaping radiation is collimated. Some efficient massive black holes in nearby AGN have been observed to radiate in the super-Eddington regime (Du et al. 2015).

---

[1] In some AGN jet models, contributions from both the CMB and the starlight background play an important role in modelling the SED. This is mainly the case when the emitting region of the jet becomes very large and extends into the radio lobes. In our case, the emitting blob is located close to the central engine, rendering the contributions from these background fields negligible.

Blackbody radiation from a Shakura-Sunyaev disk

Throughout this thesis, we will consider an optically thick, geometrically thin accretion disk, known as a Shakura-Sunyaev (SS) disk (Shakura & Sunyaev 1973), accreting around a black hole. The infalling matter has to dissipate angular momentum and potential energy, and subsequently, more energy has to be dissipated close to the black hole than further away. As a result, the temperature T^{SS} of the SS-disk increases as the radius R decreases. Consider in the following the accretion disk to be a collection of rings, each with a surface area of $2 \times 2\pi R dR$ and radiating like a blackbody. Adopting a monochromatic approximation for the mean photon energy, the temperature profile of a SS-disk is given by

$$T^{\mathrm{SS}}(R) = \left(\frac{3GM\dot{m}\varphi(R)}{8\pi R^3 \sigma_{\mathrm{SB}}} \right)^{1/4}, \tag{3.4}$$

where G is the gravitational constant, m is the mass of the black hole, $\dot{M}$ is the mass accretion rate, σ_{SB} is the Stefan-Boltzmann constant and

$$\varphi(R) = 1 - \beta_{\mathrm{i}} \left(\frac{R_i}{R} \right)^{1/2} \tag{3.5}$$

(Dermer & Menon (2009), p.106-107). The innermost stable orbit circular of a Schwarzschild black hole is $R_{\mathrm{i}} = 6R_{\mathrm{g}}$, where $R_{\mathrm{g}} = GM/c^2$ is the gravitational radii. The β_{i} parameter describes the fraction of angular momentum transferred from the accretion disk to the black hole at the inner radius. In our case, we will set $\beta_{\mathrm{i}} = 1$.

Consider now an observer at a luminosity distance $d_{\mathrm{L}} \gg R$ (see Section 6.1.1). The total accretion disk flux measured by this by this observer is

$$\nu_{\mathrm{obs}} F^{\mathrm{SS}}_{\nu_{\mathrm{obs}}} = \mu_0 \nu_{\mathrm{obs}} \frac{2\pi}{d_{\mathrm{L}}^2} \int_{R_{\mathrm{in}}}^{R_{\mathrm{out}}} dR\, R\, I_{\nu_{\mathrm{obs}}}(T^{\mathrm{SS}}(R)), \tag{3.6}$$

where I_ν is Planck's radiation law, Equation (4.3), with the temperature profile defined in Equation (3.4), and μ_0 is the cosine of the angle between the accretion disk axis and the observer's line of sight, $\mu_0 = \cos(\theta_0)$. We are interested in the total flux measured in the observer reference frame and note that the frequency transforms as

$$\nu_{\mathrm{obs}} = \frac{\nu}{(1+z)}. \tag{3.7}$$

By now, it will be helpful to introduce some notation regarding the coordinate systems we will consider. Quantities expressed in the "stationary" frame of the black hole and the host galaxy are unmarked, quantities expressed in the observer frame are marked with subscript "obs", and quantities expressed in the comoving frame of the jet will be denoted with a prime, e.g. ν'. For a full list of relevant coordinate transformations, see Chapter A.

Photon field energy density

The radiation field produced by the accretion disk will act as a target photon field for external Compton processes in the jet. Consider then the accretion disk with an inner radius R_{in} extending to the outer radius R_{out}. The full geometry is shown in Figure 3.3. The angle of photons incident on the jet is related to the radial distances as

$$\mu = \left(1 + \frac{R^2}{r^2} \right). \tag{3.8}$$

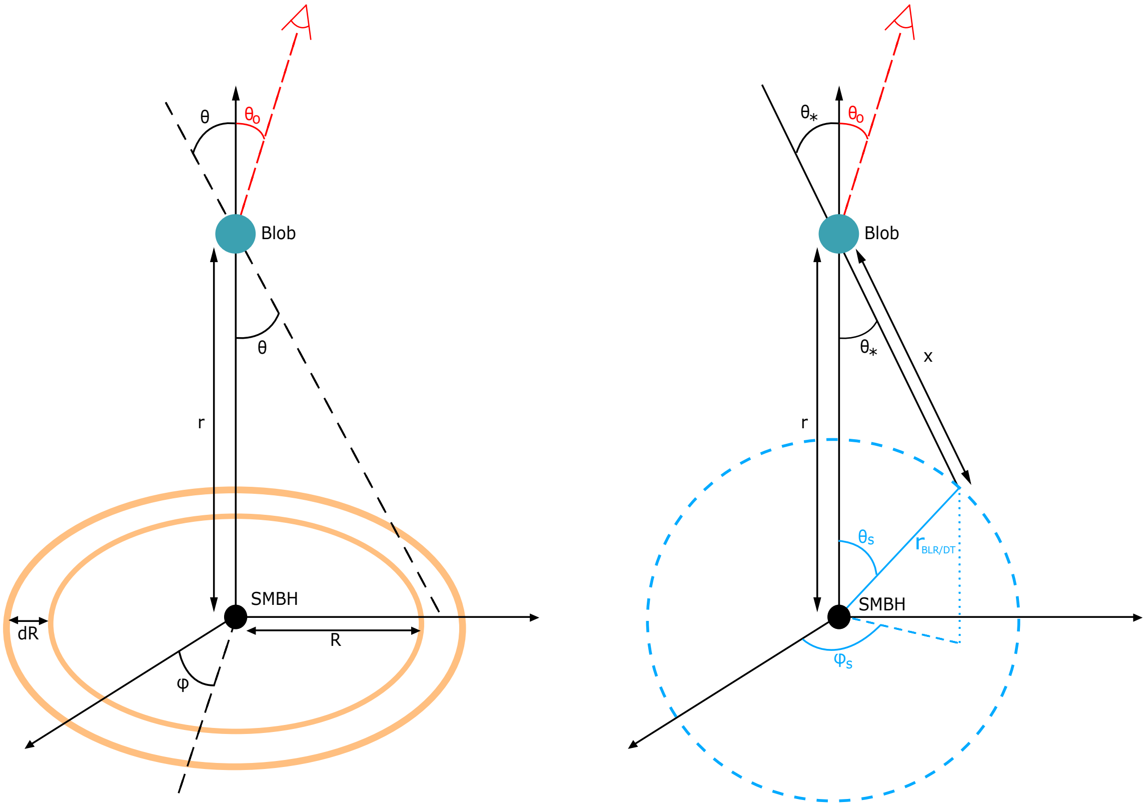

Figure 3.3: Image showing the different geometries explained in the text. *Left:* Geometry used when considering the energy density from the accretion disk. The accretion disk is considered to be a collection of rings located at a distance R from the SMBH. *Right:* Geometry used when considering the BLR to be an infinitesimally thin spherical shell located at a distance r$_{BLR}$. The same geometry is applicable to the dust torus case by setting $\theta_\mathrm{s} = \pi/2$.

With an extended accretion disk, the photons will be incident on the jet from angles varying between $\mu_{\min} = \mu(R_{\max})$ and $\mu_{\max} = \mu(R_{\min})$.

The spectral energy density of photons from a SS-disk has been parameterized by (Dermer et al. 2009) as

$$\underline{u}(\epsilon, \Omega; r) = \frac{3GM\dot{m}}{(4\pi)^2 c R^3} \varphi(R) \delta(\epsilon - \epsilon_0(R)), \tag{3.9}$$

with $\varphi(R)$ from Equation (3.5). The δ-function argument $\epsilon_0(R)$ is the monochromatic approximation for the mean photon energy emitted by the SS-disk

$$\epsilon_0(R) \cong \frac{2.70 k_{\rm B} T(R)}{m_{\rm e} c^2}, \tag{3.10}$$

where $T(R)$ is given by Equation (3.4) and $k_{\rm B}$ is Boltzmann's constant (Dermer & Menon (2009), eq. 6.137).

To find an expression for the energy density, we need to take into consideration that photons emitted at different disk radii will have different incident angles on the jet region. This is done my replacing $\varphi(R) \longrightarrow \varphi(\mu; r)$, and similarly for the photon energy $\epsilon_0(R) \longrightarrow \epsilon_0(\mu; r)$. Inserting these into Equation (3.9) and performing an integral over energy and θ gives the energy density as

$$u(r) = \frac{3}{8\pi c} \frac{GM\dot{m}}{r^3} \int_{\mu_{\min}}^{\mu_{\max}} d\mu \frac{\varphi(\mu; r)}{(\mu^{-2} - 1)^{3/2}}. \tag{3.11}$$

In the blob comoving frame, the energy density transforms into

$$u'(r) = \frac{3}{8\pi c} \frac{GM\dot{m}}{r^3} \int_{\mu_{\min}}^{\mu_{\max}} d\mu \frac{\varphi(\mu; r)}{\Gamma^6 (1 - \beta\mu)^2 (1 + \beta\mu')^4 (\mu^{-2} - 1)^{3/2}}, \tag{3.12}$$

where β is the velocity of the jet particles and Γ is the jet Lorentz factor

$$\Gamma = (1 - \beta^2)^{-1/2}. \tag{3.13}$$

Finally, the incident angle in the blob comoving frame is related to the incident angle in the host galaxy frame by

$$\mu = \frac{\mu' + \beta}{1 + \beta\mu'}. \tag{3.14}$$

The radiation field produced by the accretion disk is partially absorbed and re-emitted at different energies in both the BLR and the dust torus. In the BLR, the disk radiation is absorbed and re-radiated as Doppler-broadened line emission. In contrast, in the dust torus, the disk radiation is absorbed and re-radiated in the infrared as an approximate blackbody. In both cases, we simplify the procedure by assuming the disk radiation originates from a single point at the location of the black hole.

X-ray corona

Due to the strong X-ray emission ubiquitous in AGN observations, it is believed that the accretion disk is accompanied by a corona. This region is thought to consist of hot electrons on which photons originating from the accretion disk undergo inverse Compton scattering up to X-ray energies. The geometry or full function of the X-ray corona is unknown, but general AGN models require such a region to account for the observed emission at X-ray wavelengths. For the emission processes considered in this thesis, the X-ray corona has not been taken into consideration as its contribution would be negligible.

3.3.2 Broad-line region

The BLR is an area surrounding the central engine in which large gas clouds orbit the black hole with high angular velocity. These gas clouds are illuminated by the X-ray and UV radiation from the central engine and emit the characteristic lines of their composite particles. The broad emission lines in AGN optical spectra are caused by the Doppler motion of these gas clouds orbiting in the BLR.

It is thought that the different emission lines of the BLR occur at different radii (Peterson & Wandel 1999). We will instead consider the BLR to be an infinitesimally thin, monochromatic shell as described by Finke, 2016. The geometry is shown in Figure 3.3. Despite this being a much-simplified model, a more complex model with a broader range of emission energies can be constructed by superimposing several of these shells. From Figure 3.3, we note the geometric relations

$$\mu_*^2 = 1 - \left(\frac{r_\mathrm{s}}{x}\right)^2 (1 - \mu_\mathrm{s}^2) \tag{3.15}$$

and

$$x^2 = r_\mathrm{s}^2 + r^2 - 2 r r_\mathrm{s} \mu_\mathrm{s}, \tag{3.16}$$

where $\mu_* = \cos(\theta_*)$, $\mu_\mathrm{s} = \cos(\theta_\mathrm{s})$ and r_s is the distance from the black hole to the spherical shell BLR.

Assuming the BLR reprocesses a fraction ξ_BLR of the accretion disk luminosity, its spectral energy density can be written

$$\underline{u}(\epsilon, \Omega; r) = \frac{\xi_\mathrm{BLR} L_\mathrm{disk}}{(4\pi)^2 c} \delta(\epsilon - \epsilon_\mathrm{s}) \int_{-1}^{1} \frac{d\mu_\mathrm{s}}{x^2} \delta(\mu - \mu_*), \tag{3.17}$$

where ϵ_s is the energy of the emitted spectral line at the shell (Finke, 2016, A.21). Inserting the geometric relations from Equation (3.15) and Equation (3.16) and integrating over ϕ gives the energy density

$$u(r) = \frac{\xi_\mathrm{BLR} L_\mathrm{disk}}{8\pi c} \int_{-1}^{1} \frac{d\mu_\mathrm{s}}{x^2}. \tag{3.18}$$

Transforming this expression into the blob comoving frame, we arrive at

$$u'(r) = \frac{\xi_\mathrm{BLR} L_\mathrm{disk}}{8\pi c} \Gamma^2 \int_{-1}^{1} \frac{d\mu_\mathrm{s}}{x^2} (1 - \beta\mu_*)^2 \tag{3.19}$$

for the final energy density of the BLR photon field. The distance to the BLR is determined by the luminosity of the accretion disk through (Ghisellini & Tavecchio, 2009)

$$r_\mathrm{s} = r_\mathrm{BLR} = 10^{17} \sqrt{\frac{L_\mathrm{disk}}{10^{45} \mathrm{erg/s}}} \ \mathrm{cm}. \tag{3.20}$$

3.3.3 Dust torus

When observing AGN, we often see strong thermal emissions in the infrared range that cannot be produced by the central engine or the BLR. To account for this radiation, it is common to consider a torus consisting of dust and gas located beyond the BLR. The exact geometry of the dust torus is uncertain and may vary between different AGN categories.

The dust particles in the torus will be heated by the accretion disk radiation until they reach thermal equilibrium by re-emitting blackbody radiation in the infrared range. We can put an upper limit on the temperature of the dust torus by considering that it sublimates at around 1500 K (Kishimoto et al. 2007). Thus, the temperature of the dust torus cannot exceed this limit. Since the torus is heated by the accretion disk, the temperature will depend on the distance between the dust torus and the central engine. This can be used to derive a rough estimate of the inner radius of the dust torus, as the temperature is inversely proportional to the distance from the accretion disk. This distance is known as the *sublimation radius*.

Similar to the previous cases, we will also consider the dust torus radiation to be monochromatic with energy corresponding to the peak of the blackbody distribution.

Blackbody radiation

The dust torus contributes to the infrared emission of the SED. By considering the dust torus at a distance R_{DT} and with temperature $T^{\mathrm{DT}} \lesssim 1500$ K, the total dust torus flux measured by an observer at distance d_{L} is

$$\nu_{\mathrm{obs}} F^{\mathrm{DT}}_{\nu_{\mathrm{obs}}} = \pi \nu_{\mathrm{obs}} \left(\frac{R_{\mathrm{DT}}}{d_{\mathrm{L}}} \right)^2 I_{\nu_{\mathrm{obs}}}(T^{\mathrm{DT}}). \tag{3.21}$$

Photon field energy density

Similar to both the accretion disk radiation field and the BLR radiation field, the dust torus radiation field produces seed photons for the inverse Compton scattering processes within the jet. In what follows, we will consider yet again the approach of Finke, 2016 and consider the dust torus to be an infinitesimally thin annulus with radius R_{DT}. This geometry corresponds to that of Figure 3.3 with R_{DT} and $\theta_{\mathrm{s}} = \pi/2$. This simplifies the relevant geometric relations compared to that of the BLR case to

$$\mu_* = \frac{r}{x}, \quad x^2 = R_{\mathrm{DT}}^2 + r^2. \tag{3.22}$$

The spectral energy density for the dust torus is

$$\underline{u}(\epsilon, \Omega; r) = \frac{\xi_{\mathrm{DT}} L_{\mathrm{disk}}}{(4\pi)^2 c x^2} \delta(\mu - \mu_*) \delta(\epsilon - \epsilon_{\mathrm{DT}}), \tag{3.23}$$

where ξ_{DT} is the fraction of accretion disk luminosity reprocessed by the dust torus and ϵ_{DT} is the peak energy of the monochromatic radiation, Equation (3.10) with $T(R) = T_{\mathrm{DT}}$. Inserting the geometry from Equation (3.22) into this expression and integrating over energy and ϕ gives the energy density

$$u(r) = \frac{\xi_{\mathrm{DT}} L_{\mathrm{disk}}}{4\pi c x^2}. \tag{3.24}$$

In the jet comoving frame, this becomes

$$u'(r) = \Gamma^2 \left(1 - \beta \mu_*\right)^2 \frac{\xi_{\mathrm{DT}} L_{\mathrm{disk}}}{4\pi c x^2}. \tag{3.25}$$

The radius of the dust torus is also determined from the luminosity of the accretion disk and reads (Ghisellini & Tavecchio, 2009)

$$R_{\mathrm{DT}} = 2.5 \times 10^{18} \sqrt{\frac{L_{\mathrm{disk}}}{10^{45} \mathrm{erg/s}}} \ \mathrm{cm}. \tag{3.26}$$

3.3.4 Jet

As previously discussed, radio-loud active galaxies possess narrow features known as jets. The exact structure or composition of the jets is not fully understood, but we know that they carry extreme amounts of energy away from the central region up to Mpc distances. The jets are thought to come in pairs, as there is no reason to think that one direction is preferred and extend in directions perpendicular to the accretion disk. Observations showing only one prominent jet can be explained through relativistic beaming, increasing the luminosity of the jet pointing in our direction whilst dimming the oppositely oriented jet (Fanaroff & Riley 1974a). The jets are highly collimated and carry particles out from the central region at ultrarelativistic velocities.

Observations show that jets usually have some internal structure. Regions within the jet that show a surplus of radio emission are called knots. These regions are highly relevant candidates to explain the complex SED of active galaxies. The single zone emission region considered in this thesis works reasonably well to explain most of the SED, however, a more realistic model taking into consideration the more intricate structure of the jet and unifying emission regions close to the black hole and at the far end radio lobes is required for a more satisfactory description of AGN. Other detailed jet models and geometries exist, describing a more complex jet structure (e.g. Romero et al. 2017; Potter & Cotter 2012).

One of the largest unanswered questions in astrophysics is what powers these jets. The jets are tightly connected to the physical processes at work in the innermost part of the accretion disk, very close to the black hole. It is believed that the jets are powered by the accretion disk and the transfer of energy from the accretion disk into the root of the jet is commonly accredited to magnetically driven acceleration (Blandford & Znajek, 1977). Further complications to the understanding of the physical processes powering the jets arose with the observations of AGN with a jet power larger than the accretion disk luminosity (Ghisellini et al. 2014).

CHAPTER

FOUR

AGN EMISSION PROCESSES

The total AGN energy spectrum observed is a combination of different radiative processes from different regions. The accretion disk, accompanying X-ray corona and the dust torus all radiate like a blackbody and are important for the IR, optical and X-ray parts of the spectral energy distribution (SED). The collimated jets produce strong synchrotron and synchrotron self-Compton emissions and act like calorimeters for charged particles to scatter on ambient photon fields through external Compton processes. In order to explain the full SED, all these processes must be taken into consideration. In this chapter, we will first give a quick review of blackbody radiation, before considering the different non-thermal processes responsible for the higher energy emissions.

4.1 Blackbody radiation

German physicist Max Planck derived a formula describing the observed spectra from any blackbody at thermal equilibrium. He found that the energy density of the emitted blackbody radiation is

$$u_\nu = \frac{8\pi\nu^2}{c^3}\frac{h\nu}{\exp\left(h\nu/k_\mathrm{B}T\right) - 1}, \tag{4.1}$$

where ν is the frequency of the emitted radiation, c is the speed of light, h is Planck's constant, k_B is Boltzmann's constant and T is the temperature in Kelvin. In cgs units, u_ν has dimension erg cm^{-3} Hz^{-1}, so by differentiating with respect to the solid angle and multiplying by the velocity c, we end up with the flux

$$I_\nu = c\frac{du_\nu}{d\Omega}. \tag{4.2}$$

Considering the blackbody radiation to be isotropic, the energy density per solid angle is simply given as

$$\frac{du_\nu}{d\Omega} = \frac{u_\nu}{4\pi}.$$

Hence, the blackbody intensity is

$$I_\nu(T) = \frac{2h\nu^3}{c^2[\exp{(h\nu/k_\mathrm{B}T)} - 1]}. \tag{4.3}$$

Inserting this expression into Equation (3.6) and Equation (3.21) with their respective temperature profiles gives the total thermal contribution from both the accretion disk and the dust torus.

4.2 Non-thermal leptonic processes

The SED of AGN is dominated by non-thermal radiative processes. Energetic particles in the jet transfer their kinetic energy into radiation through two different physical mechanisms, synchrotron and Compton emissions. We continue to consider the emitting region to be a spherical blob within the jet. Detailed derivations leading to the key equations can be found in Dermer & Menon (2009).

4.2.1 Electron spectra

In order to produce high-energy radiation, we need a population of highly energetic charged particles. This is achieved by introducing a spectrum of energetic electrons accelerated in the central engine and streaming along the jet axis. By assuming a uniform and isotropic distribution, the spectral energy density of these electrons in the blob comoving frame is parametrized solely by their Lorentz factor γ' and denoted $\underline{n}'_\mathrm{e}$. We will consider this electron distribution to be a log-parabolic power law of the form

$$\underline{n}'_\mathrm{e}(\gamma') = k \left(\frac{\gamma'}{\gamma'_0}\right)^{-[p+q\log(\gamma'/\gamma'_0)]} H(\gamma'; \gamma'_\mathrm{min}, \gamma'_\mathrm{max}) \tag{4.4}$$

where k is a normalization constant, γ'_0 is the reference Lorentz factor, p and q determine the behaviour of the distribution and H is the Heaviside function, ensuring zero contribution beyond the range $\gamma'_\mathrm{min} \leq \gamma' \leq \gamma'_\mathrm{max}$.

From this electron energy distribution, it follows that the differential number of electrons, i.e. the total number of electrons per range in γ', is found by multiplying with the volume of the emitting blob

$$\underline{N}'_\mathrm{e}(\gamma') = \underline{n}'_\mathrm{e}(\gamma')V'_\mathrm{b}. \tag{4.5}$$

4.2.2 Synchrotron radiation

In the presence of a magnetic field, charged particles are accelerated and emit synchrotron radiation. The electromagnetic force on a relativistic charged particle is given by the Lorentz force equation

$$\vec{F}_\mathrm{L} = \frac{d}{dt}(\gamma m\vec{v}) = Q\left(\vec{E} + \frac{1}{c}\vec{v}\times\vec{B}\right), \tag{4.6}$$

where m and Q are the mass and charge of the particle, $\vec{v}$ is the velocity and $\vec{E}$ and $\vec{B}$ are the electric and magnetic fields. For a general derivation, see Chapter A. In most astrophysical plasmas, the mobility of charged particles causes a shortening of the electric field, and thus we may proceed with $\vec{E} = 0$.

The acceleration of charged particles is always perpendicular to their velocity. Thus, the total radiation loss rate for an electron moving with angle α relative to the magnetic field B is (eq. 8.2 Longair 2011)

$$-\left(\frac{dE}{dt}\right) = \frac{e^4 B^2}{6\pi\epsilon_0 c m_\mathrm{e}^2}\frac{v^2}{c^2}\gamma^2 \sin^2\alpha, \tag{4.7}$$

where e is the electron charge and ϵ_0 is the vacuum permittivity. Since the energy loss rate is a Lorentz invariant quantity, this expression is the same in the blob comoving frame, $(dE/dt) = (dE/dt)'$.

Introducing now the dimensionless energy $\epsilon = h\nu/(m_\mathrm{e}c^2)$ for the emitted synchrotron photons, where ν is the photon frequency and h is Planck's constant, and following the derivation of Dermer & Menon (2009), the energy flux observed on Earth from synchrotron processes in the jet blob is

$$\nu_\mathrm{obs}F^\mathrm{synch}_{\nu_\mathrm{obs}} = \frac{\delta_\mathrm{D}^4}{4\pi d_\mathrm{L}^2}\epsilon'\frac{\sqrt{3}e^3 B}{h}\int_1^\infty d\gamma' N'_\mathrm{e}(\gamma')R(x). \tag{4.8}$$

Here, δ_D is the Doppler factor regulating transformations to and from the reference frame of the blob and d_L is the luminosity distance to the source. The $R(x)$ function accounts for the pitch-angle-averaged spectral power of a single electron and is given as

$$R(x) = \frac{1}{2}\pi x\left[W_{0,\frac{4}{3}}(x)W_{0,\frac{1}{3}}(x) - W_{\frac{1}{2},\frac{5}{6}}(x)W_{-\frac{1}{2},\frac{5}{6}}(x)\right], \tag{4.9}$$

where $W_{\kappa,\lambda}$ are Whittaker functions (see Chapter A) with the function argument

$$x = \frac{4\pi\epsilon' m_\mathrm{e}^2 c^3}{3eBh\gamma'^2}. \tag{4.10}$$

It is practical to instead have an expression for R that does not depend on any special functions. Aharonian et al. (2010) proposed such an approximation,

$$\tilde{R}(x) \approx \frac{1.808x^{1/3}}{\sqrt{1+3.4x^{2/3}}}\frac{1+2.21x^{2/3}+0.347x^{4/3}}{1+1.353x^{2/3}+0.217x^{4/3}}e^{-x}. \tag{4.11}$$

This numerical approximation $\tilde{R}$ is valid to within 0.2% of R and will be used when calculating the synchrotron radiation from AGN.

4.2.3 Synchrotron self-absorption

So far, we have assumed that all the emitted photons from the synchrotron process reach the observer. This, however, might not always be the case. As a photon created through the synchrotron process propagates through the plasma of its source environment, it may scatter off the synchrotron electrons. This process is known as synchrotron self-absorption (SSA).

This effect is taken into account by multiplying Equation (4.8) with an absorption factor

$$\nu_{\mathrm{obs}} F_{\nu_{\mathrm{obs}}}^{\mathrm{SSA}} = \nu_{\mathrm{obs}} F_{\nu_{\mathrm{obs}}}^{\mathrm{synch}} \times \frac{3}{\tau_{\mathrm{SSA}}} \left(\frac{1}{2} + \frac{\exp(-\tau_{\mathrm{SSA}})}{\tau_{\mathrm{SSA}}} - \frac{1-\exp(-\tau_{\mathrm{SSA}})}{\tau_{\mathrm{SSA}}^2} \right), \tag{4.12}$$

where τ_{SSA} is an energy-dependent SSA opacity and reads

$$\tau_{\mathrm{SSA}}(\epsilon') = -\frac{R'_{\mathrm{b}}}{8\pi m_{\mathrm{e}} \epsilon'^2} \left(\frac{\lambda_{\mathrm{C}}}{c} \right)^3 \int_1^\infty d\gamma' R(x) \left[\gamma'^2 \frac{\partial}{\partial \gamma'} \left(\frac{\underline{n}'_{\mathrm{e}}}{\gamma'^2} \right) \right], \tag{4.13}$$

where R_{b} is the radius of the blob and $\lambda_{\mathrm{C}} = h/(m_{\mathrm{e}} c)$ is the Compton wavelength.

4.2.4 Inverse Compton radiation

The textbook approach to Compton scattering is to imagine an electron in its rest frame being hit by a high-frequency incident photon. The electron gains some energy, whereas the photon is scattered to larger wavelengths. In highly energetic astrophysical environments, the inverse process is more important. In inverse Compton scattering, relativistic electrons scatter incident photons to higher frequencies. This, together with the previously discussed synchrotron radiation, is believed to be the dominant progenitor for high-energy radiation in the Universe. In the following derivations, we will consider both *Klein-Nishina* regime (see e.g. Longair 2011, p. 237) when in the blob comoving frame, where the dimensionless energy of the scattered photon $\epsilon = \lambda_{\mathrm{C}}/\lambda \gg 1$, and the *Thomson* regime when in the host galaxy comoving frame, where $\epsilon = \ll 1$.

Synchrotron self-Compton

In the synchrotron self-Compton (SSC) process, photons created through synchrotron radiation from electrons are scattered to higher energies by the same electron population.

To calculate the flux from the SSC process we must first define the energy density of the ambient photon field created through the synchrotron process. This can be obtained from Equation (4.8) as

$$\underline{u}'_{\mathrm{synch}}(\epsilon') = \frac{3}{4} \frac{3 d_{\mathrm{L}}^2 \nu_{\mathrm{obs}} F_{\nu_{\mathrm{obs}}}^{\mathrm{synch}}}{c R_{\mathrm{b}}'^2 \delta_{\mathrm{D}}^4 \epsilon'}, \tag{4.14}$$

where the additional factor of 3/4 comes from averaging over the radiation within a sphere (Finke et al. 2008).

With this, we can compute observed flux from the SSC process as

$$\nu_{\mathrm{obs}} F_{\nu_{\mathrm{obs}}}^{\mathrm{SSC}} = \frac{\delta_{\mathrm{D}}^4}{4\pi d_{\mathrm{L}}^2} \frac{3}{4} c \sigma_{\mathrm{T}} \epsilon_{\mathrm{s}}'^2 \int_0^\infty d\epsilon' \frac{\underline{u}'_{\mathrm{synch}}(\epsilon')}{\epsilon'^2} \int_0^\infty d\gamma' \frac{\underline{N}'_{\mathrm{e}}(\gamma')}{\gamma'^2} F_{\mathrm{C}}(q', \Gamma'_{\mathrm{e}}), \tag{4.15}$$

where σ_{T} is the Thompson cross-section and ϵ is the energy of the synchrotron photon. F_{C} is an integration kernel representing the Compton cross-section for electrons and photons assuming a uniform distribution for both. It takes the form

$$F_{\mathrm{C}}(q', \Gamma'_e) = \left[2q' \ln q' + (1+2q')(1-q') + \frac{1}{2} \frac{(\Gamma'_{\mathrm{e}} q')^2}{1+\Gamma'_{\mathrm{e}} q'} (1-q') \right] H\left(q'; \frac{1}{4\gamma'^2}, 1 \right), \tag{4.16}$$

where

$$q' = \frac{\epsilon'_{\mathrm{s}}/\gamma'}{\Gamma'_{\mathrm{e}}(1-\epsilon'_{\mathrm{s}}/\gamma')}, \tag{4.17}$$

and $\Gamma'_{\mathrm{e}} = 4\epsilon'_{\mathrm{s}}\gamma'$.

External Compton

In the external Compton (EC) process, high-energy photons are created through scattering events of collimated jet electrons on ambient photon fields created in regions external to the jet. In Chapter 3, we derived the energy density of such photon fields created by the accretion disk, broad-line region and dust torus. We will now consider how photons from these fields gain energy from electrons in the jet.

In order to simplify the calculation of the spectra from external Compton emission for external photon targets, we consider the "head-on" approximation, i.e. $\gamma' \gg 1$ and, due to the relativistic transformation of the angles, photons scatter back at approximately the same angels as the incident electrons. Under this assumption,

$$\frac{d\sigma_{\mathrm{C}}}{d\epsilon_{\mathrm{s}} d\Omega_{\mathrm{s}}} \approx \frac{d\Omega_{\mathrm{C}}}{d\epsilon_{\mathrm{s}}} \delta(\Omega_{\mathrm{s}} - \Omega_{\mathrm{e}}), \tag{4.18}$$

where σ_{C} is the Compton cross section, Ω_{s} is the direction of the scattered photons and Ω_{e} is the direction of the electrons.

The external Compton emission is calculated in the reference frame stationary with respect to the AGN host galaxy. To transform the electron distribution to this frame, we note the transform

$$\underline{N}_{\mathrm{e}}(\gamma, \Omega_{\mathrm{e}}) = \delta_{\mathrm{D}}^3 \underline{N}'_{\mathrm{e}}(\gamma/\delta_{\mathrm{D}}). \tag{4.19}$$

Given all these assumptions, the energy flux produced by the blob electrons scattering on external photon fields is given as

$$\nu_{\mathrm{obs}} F^{\mathrm{EC}}_{\nu_{\mathrm{obs}}} = \frac{c\pi r_{\mathrm{e}}^2}{4\pi d_{\mathrm{L}}^2} \epsilon_{\mathrm{s}}^2 \delta_{\mathrm{D}}^3 \int d\Omega \int_0^{\epsilon_{\mathrm{high}}} d\epsilon \frac{\underline{u}(\epsilon, \Omega; r)}{\epsilon^2} \int_{\gamma_{\mathrm{low}}}^{\infty} d\gamma \frac{\underline{N}'_{\mathrm{e}}(\gamma/\delta_{\mathrm{D}})}{\gamma^2} \Xi_{\mathrm{C}}, \tag{4.20}$$

where r_{e} is the electron radius and $\underline{u}$ is the energy density of the external photon field. The Compton kernel Ξ_{C} reduces in the head-on approximation to the integration kernel

$$\Xi_{\mathrm{C}} \equiv y + y^{-1} - \frac{2\epsilon_{\mathrm{s}}}{\gamma\bar{\epsilon}y} + \left(\frac{\epsilon_{\mathrm{s}}}{\gamma\bar{\epsilon}y}\right)^2, \tag{4.21}$$

with

$$y = 1 - \frac{\epsilon_{\mathrm{s}}}{\gamma} \tag{4.22}$$

and

$$\bar{\epsilon} = \epsilon\gamma(1 - \cos\psi), \tag{4.23}$$

where ψ is the angle between the incident photon and the scattering electron. For the accretion disk, BLR and dust torus,

$$\begin{aligned} \cos\psi_{\mathrm{disk}} &= \mu\mu_0 + \sqrt{1-\mu^2}\sqrt{1-\mu_0}\cos\phi, \\ \cos\psi_{\mathrm{BLR}} &= \mu_*\mu_0 + \sqrt{1-\mu_*^2}\sqrt{1-\mu_0^2}\cos\phi_{\mathrm{s}}, \\ \cos\psi_{\mathrm{DT}} &= \frac{r}{x}\mu_0 + \sqrt{1-(r/x)^2}\sqrt{1-\mu_0^2}\cos\phi_{\mathrm{s}}, \end{aligned} \tag{4.24}$$

respectively (see Figure 3.3).

The integration limits in Equation (4.20) are imposed by kinetic limits for both the target energy

$$\epsilon_{\text{high}} = \frac{2\epsilon_{\text{s}}}{1 - \cos\psi}, \tag{4.25}$$

and for the electron Lorentz factor

$$\gamma_{\text{low}} = \frac{\epsilon_{\text{s}}}{2}\left[1 + \sqrt{1 + \frac{2}{\epsilon\epsilon_{\text{s}}(1 + \cos\psi)}}\right]. \tag{4.26}$$

To compute the contribution from external Compton emission to the full SED, the energy density of the photon fields derived in Chapter 3 are inserted for $\underline{u}$ in Equation (4.20).

4.3 Photomeson processes

The production of high-energy neutrinos usually requires a source population of energetic protons. Under the proper conditions, these protons interact with ambient photon fields and create pions that further decay into muons and electrons, with accompanying neutrinos. In the following section, we adopt the methodology of Kelner & Anaronian (2008) to describe the subsequent electrons, gamma-rays and neutrinos produced when pions are created through proton-photon interactions.

We restate the proton-photon process from Equation (2.12),

$$\text{p} + \gamma \longrightarrow \xi_0\pi^0 + \xi_+\pi^+ + \xi_-\pi^- + ..., \tag{4.27}$$

where ξ_0, ξ_+, and ξ_- are the number of different pions produced. To simplify the calculations required in our model, we make the following three assumptions.

- We assume that the density of the ambient medium is low enough for the pions to decay before interacting with surrounding matter, radiation or magnetic field.
- Both the protons and the ambient target photons are isotropically distributed.
- The energy of the target photons and the energetic protons are

  $$\epsilon \ll m_\pi c^2, \quad E_{\text{p}} \gg m_{\text{p}}c^2, \tag{4.28}$$

  where ϵ is the photon energy, $m_\pi = m_{\pi^\pm} = m_{\pi^0}$ is the mass of the pion and E_{p} and m_{p} are the energy and the mass of the proton.

4.3.1 Gamma-ray production

Whereas the charged pions decay further into leptons, the neutral π-mesons primary decay channel is to a pair of gamma rays,

$$\pi^0 \longrightarrow 2\gamma. \tag{4.29}$$

As we have assumed an isotropic distribution of the initial particles, the resulting gamma rays will also be isotropically distributed. The more detailed derivation of Kelner & Anaronian (2008) gives the production rate of gamma-rays as

$$\frac{dN_\gamma}{dE_\gamma} = \int f_{\text{p}}(E_{\text{p}})f_{\text{ph}}(\epsilon)\Phi_\gamma(\eta, x)\frac{dE_{\text{p}}}{E_{\text{p}}}d\epsilon, \tag{4.30}$$

where f_p and f_ph are the proton and photon distributions, respectively. The Φ function describes the energy distribution for the neutral pion decay process. Its function arguments are given as

$$\eta = \frac{4\epsilon E_\mathrm{p}}{m_\mathrm{p}^2 c^4} \tag{4.31}$$

and x is the dimensionless relative energy between the produced photon and incident proton,

$$x = \frac{E_\gamma}{E_\mathrm{p}}. \tag{4.32}$$

For the creation of a single π^0-meson, the energy of the incident proton must satisfy

$$2\epsilon E_\mathrm{p}(1 - \beta_\mathrm{p}\cos\theta) > (2m_\pi m_\mathrm{p} + m_\pi^2)c^4, \tag{4.33}$$

where β_p is the velocity of the incoming proton and θ is the angle between the momentum of the colliding particles. Since the jet protons are ultrarelativistic, we set $\beta_\mathrm{p} = 1$. If this condition is not satisfied, the proton carries insufficient energy and the energy distribution $\Phi_\gamma = 0$. The integral of Equation (4.30) must therefore be performed for

$$\eta \geq \eta_0 \equiv 2\frac{m_\pi}{m_\mathrm{p}} + \frac{m_\pi^2}{m_\mathrm{p}} \approx 0.313. \tag{4.34}$$

The energies of the produced pions will vary between $E_{\pi,\mathrm{min}} = E_\mathrm{p} x_-$ and $E_{\pi,\mathrm{max}} = E_\mathrm{p} x_+$, with

$$x_\pm = \frac{1}{2(1+\eta)}\left[\eta + r^2 \pm \sqrt{(\eta - r^2 - 2r)(\eta - r^2 + 2r)}\right], \tag{4.35}$$

where $r = m_\pi/m_\mathrm{p} \approx 0.146$. The general case where the total mass of the secondary particles exceeds m_π is more complicated and will not be explored further.

Calculating the energy distribution Φ_γ is a complicated process, so we will make a simplification. To within 10%, Φ_γ can be approximated by the analytical formulae (Kelner & Anaronian (2008), eq. 31-33)

$$\tilde{\Phi}_\gamma(\eta, x) = \begin{cases} B_\gamma (\ln 2)^{2.5+0.4\ln(\eta/\eta_0)}, & x < x_-, \\ B_\gamma \exp\left(-s_\gamma\left[\ln\left(\frac{x}{x_-}\right)\right]^{\delta_\gamma}\right) \times \left[\ln\left(\frac{2}{1+y^2}\right)\right]^{2.5+0.4\ln(\eta/\eta_0)}, & x_- < x < x_+, \\ 0, & x > x_+, \end{cases} \tag{4.36}$$

where ln is the natural logarithm and

$$y = \frac{x - x_-}{x_+ - x_-}. \tag{4.37}$$

The three parameters B_γ, s_γ, and δ_γ are all functions of η and their values are listed in Table I of Kelner & Anaronian (2008). We note that $\tilde{\Phi}_\gamma$ has dimension cm^3/s.

4.3.2 Lepton production

The production of leptons in proton-photon interactions happens mainly through the decay of the secondary $\pi^{\pm}$-mesons. We can write their production rate in the same way as for the gamma rays,

$$\frac{dN_\gamma}{dE_\gamma} = \int f_{\mathrm{p}}(E_{\mathrm{p}}) f_{\mathrm{ph}}(\epsilon) \Phi_{\mathrm{l}}(\eta, x) \frac{dE_{\mathrm{p}}}{E_{\mathrm{p}}} d\epsilon, \tag{4.38}$$

where the subscript "l" corresponds to one of the e^+, e^-, ν_{e}, $\bar{\nu}_{\mathrm{e}}$, ν_μ, $\bar{\nu}_\mu$ symbols. In a similar manner to the gamma-ray case, the Φ_{l} is a complicated expression found by considering the kinematics of the process. We find instead a simple analytical expression for the energy distribution of leptons as

$$\tilde{\Phi}_{\mathrm{l}}(\eta, x) = \begin{cases} B_{\mathrm{l}} (\ln 2)^{\psi(\eta)}, & x < x_-^*, \\ B_{\mathrm{l}} \exp\left(-s_{\mathrm{l}} \left[\ln\left(\frac{x}{x_-} \right) \right]^{\delta_{\mathrm{l}}} \right) \times \left[\ln\left(\frac{2}{1+y^{*2}} \right) \right]^{\psi(\eta)}, & x_-^* < x < x_+^*, \\ 0, & x > x_+^*, \end{cases} \tag{4.39}$$

where now

$$y^* = \frac{x - x_-^*}{x_+^* - x_-^*} \tag{4.40}$$

and ψ and $x_\pm^*$ depend on what leptons are being produced. The numerical values of B_{l}, s_{l} and δ_{l} depend on η and can be found in Table II and Table III of Kelner & Anaronian (2008).

Positrons, muon antineutrinos and electron neutrinos

For the creation of e^+, $\bar{\nu}_\mu$ and ν_{e}, the starred quantities $x_\pm^*$ take the form

$$x_-^* = \frac{x_-}{4} \quad \text{and} \quad x_+^* = x_+, \tag{4.41}$$

and

$$\psi(\eta) = 2.5 + 1.4 \ln\left(\frac{\eta}{\eta_0} \right), \tag{4.42}$$

where η_0 is given by Equation (4.34) and $x_\pm^*$ by Equation (4.35).

When $\eta < 4m_\pi/m_{\mathrm{p}} + 4(m_\pi/m_{\mathrm{p}})^2 = 2.14\eta_0$, only a single π^+-meson can be produced which decays into $\pi^+ \longrightarrow \mu^+\nu_\mu$. The subsequent antimuon decays into $\mu^+ \longrightarrow e^+\bar{\nu}_\mu\nu_{\mathrm{e}}$. However, when $\eta > 2.14\eta_0$, the additional channel for the production of π^--mesons opens. The π^--meson decays into $\pi^- \longrightarrow \mu^-\bar{\nu}_\mu$. Thus, when η surpasses $2.14\eta_0$, the production of $\bar{\nu}_\mu$ increases compared to e^+ and ν_{e}.

Muon neutrinos

For the production of ν_μ, the relevant process is the decay of the muon $\mu^- \longrightarrow e^-\nu_\mu\bar{\nu}_{\mathrm{e}}$. In this case, the $x_\pm^*$ parameters differ due to the different limitations for the maximal energy of ν_μ compared to $\bar{\nu}_\mu$. For a more detailed discussion, see Kelner & Anaronian (2008) and references therein. The new $x^*_\pm$ parameters are

$$x^*_+ = \begin{cases} 0.427x_+, & \rho < 2.14, \\ (0.427 + 0.0729(\rho - 2.14))x_+, & 2.14 < \rho < 10, \\ x_+, & \rho > 10, \end{cases} \tag{4.43}$$

and

$$x^*_- = 0.427x_-, \tag{4.44}$$

where $\rho = \eta/\eta_0$. For ν_μ. The same ψ-function as for e^+, $\bar{\nu}_\mu$ and ν_e is used.

Electrons and electron antineutrinos

The production of e^- and $\bar{\nu}_e$ happens through the decay of μ^-. Thus, to produce e^- and $\bar{\nu}_e$, the initial proton-photon interaction needs to produce at least two pions. This only happens for $\eta > 2.14\eta_0$, and thus the production of e^- and $\bar{\nu}_e$ should be suppressed compared to the other leptons, especially at lower proton energies. For this case, the limits of the pion energy change to

$$x_{\mathrm{min/max}} = \frac{1}{2(1+\eta}\left(\eta - 2r \pm \sqrt{\eta(\eta - 4r(1+r))}\right), \tag{4.45}$$

and the $x^*_\pm$ required for Equation (4.39) are now $x^*_+ = x_{\mathrm{max}}$ and $x^*_+ = x_{\mathrm{min}}/2$. Finally, we also need to modify the ψ factor for the e^- and $\bar{\nu}_e$ case to

$$\psi(\eta) = 6\left(1 - \exp^{1.5(4-\rho)}\right) H(\rho - 4), \tag{4.46}$$

where ρ is still $\rho = \eta/\eta_0$ and H is the Heaviside function.

To calculate the final number of gamma rays, electrons and neutrinos produced, we put the aforementioned expressions into Equation (4.30) for gamma rays, and Equation (4.38) for the different leptons. However, instead of performing the integral over the photon energy ϵ, it is more convenient to consider an integral in η. The spectra of produced photons and leptons are then given by

$$\frac{dN}{dE} = \int_{\eta_0}^{\infty} \mathcal{H}(\eta, E) d\eta, \tag{4.47}$$

where the $\mathcal{H}$ function is

$$\mathcal{H}(\eta, E) = \frac{m_\mathrm{p}^2 c^4}{4} \int_E^\infty \frac{dE_\mathrm{p}}{E_\mathrm{p}^2} f_\mathrm{p}(E_\mathrm{p}) f_\mathrm{ph}\left(\frac{\eta m_\mathrm{p}^2 c^4}{4E_\mathrm{p}}\right) \tilde{\Phi}\left(\eta, \frac{E}{E_\mathrm{p}}\right). \tag{4.48}$$

The $\tilde{\Phi}$ function is $\tilde{\Phi}_\gamma$ when E is the gamma-ray energy and $\tilde{\Phi}_\mathrm{l}$ when E is energy of the leptons. Equation (4.47) will be used in Chapter 7 to calculate the neutrinos produced in our blob model for high-redshift blazars.

CHAPTER

FIVE

LUMINOSITY FUNCTIONS AND AGN SURVEYS

In this chapter, we will introduce general luminosity functions and why they are useful for population studies. Further, we will consider the individual cases of the radio luminosity function (RLF), the X-ray luminosity function (XLF) and the gamma-ray luminosity function (GLF) and the corresponding surveys used when constructing them.

5.1 General luminosity function

A common way of representing the number density of astrophysical populations is with the use of luminosity functions. Luminosity functions describe the number of objects within a given population N, per unit volume V, and per unit luminosity L. The differential luminosity function has the form

$$\frac{d\Psi(L,V(z))}{dL} = \frac{d^2N(L,V(z))}{dLdV(z)}. \tag{5.1}$$

By multiplying with the co-moving volume, the luminosity function can be expressed as a function of redshift instead of volume,

$$\frac{d\Psi(L,z)}{dL} = \frac{d^2N(L,V(z))}{dLdV(z)} \times \frac{dV(z)}{dz} = \frac{d^2N(L,z)}{dLdz}. \tag{5.2}$$

In parts of the literature, luminosity functions are expressed as a base-10 logarithm in luminosity. We will consider the non-logarithm case, but to easier compare with previous works, we note the simple conversion between the two,

$$\frac{\Psi(L,z)}{d\log L} = \ln(10)L\frac{\Psi(L,z)}{dL}, \tag{5.3}$$

where "log" refers to the base-10 logarithm and "ln" refers to the natural logarithm.

The full luminosity function, describing the complete evolution of the population, is usually defined as a product between the local ($z = 0$) luminosity function and an additional evolution term. How this evolution term is added to the local luminosity function depends on the model that best fits the observations. The pure luminosity evolution (PLE) model evolves the luminosities with a redshift-dependent evolution function $e(z)$. In contrast, the pure density evolution (PDE) model evolves the local number density with a similar evolution function. For these two models, the full luminosity function can be expressed as

$$\frac{d\Psi(L,z)}{dL} = \begin{cases} \dfrac{d\Psi(L/e(z), z=0)}{dL} & \text{(PLE)} \\ \dfrac{d\Psi(L, z=0)}{dL} \times e(z) & \text{(PDE)} \end{cases} . \tag{5.4}$$

The PLE and PDE models are the most basic expressions for the luminosity function, and at times fail to represent the observational data. It is therefore useful to also consider the luminosity dependent density evolution (LDDE) model. The LDDE model introduces an evolution term dependent on both redshift and luminosity, resulting in the total, evolving luminosity function

$$\frac{d\Psi(L,z)}{dL} = \frac{d\Psi(L, z=0)}{dL} \times e(L,z) \quad \text{(LDDE)}. \tag{5.5}$$

5.2 Radio luminosity function

The radio luminosity function we will consider was first defined by Willott et al. 2001. It was constructed by considering steep-spectrum radio sources and we will use it to model radio galaxies. It splits the total luminosity function in two, allowing for two different populations to have different properties. The low-luminosity population is described by a Schechter function (Schechter, 1976) combining a power law with an exponential cutoff,

$$\frac{d\Psi_\mathrm{l}(L_\mathrm{R}, z=0)}{dL_\mathrm{R}} = \frac{A_\mathrm{l}}{\ln(10) L_\mathrm{R}} \left(\frac{L_\mathrm{R}}{L_{\mathrm{l}^*}}\right)^{-\alpha_\mathrm{l}} \exp\left(\frac{-L_\mathrm{R}}{L_{\mathrm{l}^*}}\right). \tag{5.6}$$

Here, L_R is the radio luminosity, A_l is a normalization term, L_{l^*} is the break luminosity, and α_l is the slope of the power law. The subscript “l” refers to the low luminosity population. A redshift dependence of the population is introduced by multiplying Equation (5.6) with

$$e_\mathrm{l}(z) = \begin{cases} (1+z)^{k_\mathrm{l}} & \text{for } z < z_\mathrm{l} \\ (1+z_\mathrm{l})^{k_\mathrm{l}} & \text{for } z \geq z_\mathrm{l} \end{cases} . \tag{5.7}$$

This additional term describes the redshift evolution of the source population up to a maximal redshift z_l, after which there is no evolution.

The high-luminosity population is described with a similar Schecter function, with the only difference being the behaviour of the exponential term,

$$\frac{d\Psi_\mathrm{h}(L_\mathrm{R}, z=0)}{dL_\mathrm{R}} = \frac{A_\mathrm{h}}{\ln(10) L_\mathrm{R}} \left(\frac{L_\mathrm{R}}{L_{\mathrm{h}^*}}\right)^{-\alpha_\mathrm{h}} \exp\left(\frac{-L_{\mathrm{h}^*}}{L_\mathrm{R}}\right), \tag{5.8}$$

where the subscript “h” now refers to the high luminosity population. It is assumed that $L_{\mathrm{l}^*} \approx L_{\mathrm{h}^*}$, such that the decline in one of the populations is compensated by an increase in the other. The redshift dependence of the high-luminosity population is introduced by multiplying Equation (5.8) with

$$e_{\mathrm{h}}(z) = \begin{cases} \exp\left[-\frac{1}{2}\left(\frac{z - z_{\mathrm{h},0}}{z_{\mathrm{h},1}}\right)^2\right] & \text{for } z < z_{\mathrm{h},0} \\ \\ \exp\left[-\frac{1}{2}\left(\frac{z - z_{\mathrm{h},0}}{z_{\mathrm{h},2}}\right)^2\right] & \text{for } z \geq z_{\mathrm{h},0} \end{cases} . \tag{5.9}$$

In total, the low-luminosity population is described by five parameters, whereas the high-luminosity population is described by six. By combining the two of them,

$$\frac{d\Psi(L_{\mathrm{R}}, z)}{dL_{\mathrm{R}}} = \frac{d\Psi_l(L_{\mathrm{R}}, z = 0)}{dL_{\mathrm{R}}} \times e_{\mathrm{l}}(z) + \frac{d\Psi_{\mathrm{h}}(L_{\mathrm{R}}, z = 0)}{dL_{\mathrm{R}}} \times e_{\mathrm{h}}(z), \tag{5.10}$$

the final radio luminosity function describes the entire radio-detected AGN population with 11 free parameters.

5.2.1 Radio surveys

We consider three different radio surveys. The faint population is described by the sources detected in the 7C Redshift Survey (Blundell et al. 2002; Lacy et al. 1999). The 7C Redshift Survey contains radio sources with a low-frequency flux-density, $S \geq 0.5$ Jy, at the 151 MHz radio frequency. Excluding some of the sources, we are left with 128 radio sources for the low-luminosity radio population (Willott et al. 2001).

The high-luminosity samples are the 3CRR sample of Laing et al. (1983) and a revised version of the 6C sample of Eales (1985). The 3CRR sample contributes with 170 radio sources at 151 MHz radio frequency, as the survey is flux limited at 12.4 Jy. The 6C sample consists of 58 radio sources within $2 \leq S \leq 3.93$ Jy at the 151 MHz radio frequency.

In total, there are 356 radio detected sources with virtually complete redshift information used to fit the 11 parameters of the radio luminosity function.

5.3 X-ray luminosity function

We will consider X-ray luminosity functions of multiple different AGN, including Seyferts, radio galaxies, general blazar populations and the FSRQ and BL Lac blazar sub-populations. The X-ray luminosity function (XLF) is expressed locally (z=0) as a power law of the form (Ajello et al. 2009)

$$\frac{d\Psi(L_{\mathrm{X}}, z = 0)}{dL_{\mathrm{X}}} = \frac{A}{L_*}\left(\frac{L_{\mathrm{X}}}{L_*}\right)^{-\gamma_2} . \tag{5.11}$$

However, at a high enough source count, a break appears and the XLF is better fitted by a broken power law (e.g. Ueda et al. 2003)

$$\frac{d\Psi(L_{\mathrm{X}}, z = 0)}{dL_{\mathrm{X}}} = \frac{A}{\ln(10)L_X}\left[\left(\frac{L_{\mathrm{X}}}{L_*}\right)^{\gamma_1} + \left(\frac{L_X}{L_*}\right)^{\gamma_2}\right], \tag{5.12}$$

which splits the behaviour of the luminosity function at the break luminosity L_*.

The evolution of the XLF depends on the chosen model. For the PLE and PDE case, the form of the evolution factor additionally depends on which AGN population surveys have been considered. Ajello et al. 2009 presented the evolution factor

$$e(z) = (1+z)^{p_1+p_2 z}, \tag{5.13}$$

whose behaviour is determined by the indices p_1 and p_2. In the simplest case, $p_2 = 0$, and the evolution factor becomes a simple power law. To better fit the data however, the evolution factor requires the extra redshift dependence.

Ueda et al. 2003 introduced a different behaviour for the evolution term. To better fit the data, he required the evolution function to behave differently with respect to a characteristic redshift z_c, and so

$$e(z) = \begin{cases} (1+z)^{p_1} & \text{if } z < z_\mathrm{c} \\ e(z_\mathrm{c})\left(\dfrac{1+z}{1+z_\mathrm{c}}\right)^{p_2} & \text{if } z \geq z_\mathrm{c} \end{cases}, \tag{5.14}$$

where the indices p_1 and p_2 now determine the evolution before and after the redshift break z_c respectively.

The most recent attempt at determining an evolution function to the PLE and PDE models was done by Marcotulli et al. 2022. Similar to Ajello et al. 2009, they used a single redshift-dependent power law, but modified it with an exponential term

$$e(z) = (1+z)^{p_1} e^{z/p_2}, \tag{5.15}$$

where the p_2 index now functions as an exponential cut-off term.

Both the PLE and the PDE models have provided difficulties when trying to describe the evolving luminosity function. The PLE model has a tendency to underestimate the number of sources at lower ($\log L_\mathrm{X} < 45$) luminosities, whereas the PDE model does the same at higher luminosities ($\log L_\mathrm{X} \geq 44.5$) (Ueda et al. 2003). Therefore, the LDDE model gives in many cases a better description of the evolution of the XLF. In the LDDE model, the evolution term becomes a function of both luminosity and redshift,

$$e(L_X, z) = \begin{cases} (1+z)^{p_1} & \text{if } z \leq z_*(L_\mathrm{X}) \\ e[z_*(L_\mathrm{X})]\left(\dfrac{1+z}{1+z_*(L_\mathrm{X})}\right)^{p_2} & \text{if } z > z_*(L_\mathrm{X}) \end{cases}, \tag{5.16}$$

where the break redshift depends on the luminosity through

$$z_*(L_\mathrm{X}) = \begin{cases} z_\mathrm{c}\left(\dfrac{L_\mathrm{X}}{L_\mathrm{c}}\right)^{\alpha} & \text{if } L_\mathrm{X} \leq L_\mathrm{c} \\ z_\mathrm{c} & \text{if } L_\mathrm{X} > L_\mathrm{c} \end{cases}, \tag{5.17}$$

which again depends on the characteristic redshift cut-off z_c. All parameters required to construct the full XLF are model dependent, changing depending on the X-ray population survey.

Marcotulli et al. 2022 introduced a slightly different way of parameterizing the evolution term in the LDDE model. Instead of splitting the evolution function based on some characteristic redshift, they instead adapted a broken power law

$$e(L_{\mathrm{X}}, z) = \left[\left(\frac{1+z}{1+z_*(L_{\mathrm{X}})} \right)^{-p_1} + \left(\frac{1+z}{1+z_*(L_{\mathrm{X}})} \right)^{-p_2} \right]^{-1}, \tag{5.18}$$

where the luminosity dependent characteristic redshift is

$$z_*(L_{\mathrm{X}}) = z_{\mathrm{c}} \left(\frac{L_{\mathrm{X}}}{L_{\mathrm{c}}} \right)^{\alpha}. \tag{5.19}$$

In Chapter 6, we will consider all the different aforementioned models for the XLF.

5.3.1 X-ray surveys

For the different XLF models, we consider surveys conducted in four different X-ray bands, selecting AGN populations with different observed properties.

The (2-8 keV) X-ray survey by Silverman et al. 2008 measured the hard XLF of AGN from a sample provided by the *Chandra* telescope (Weisskopf et al. 2002). Additionally, sources found in the *XMM-Newton* observations and the *ASCA* survey were added for a more complete sample. For further details on the surveys, see Silverman et al. 2008. In total, the 2-8 keV survey consists of 682 identified AGN and we will use this to model the radio galaxy population.

The (2-10 keV) X-ray survey by Ueda et al. 2003 contains a total of 247 detected AGN. This survey considers a flux-limited, hard X-ray selected sample based on the *HEAO1* survey, the *ASCA* survey and observations by the Chandra telescope. For more details on the complete surveys, see Ueda et al. 2003. We will consider this sample to construct a general XLF for the radio galaxy population.

The (15-55 keV) X-ray survey by Ajello et al. 2009 contains X-ray detected blazars. Based on three years of date from the *Burst Alert Telescope* (BAT) (Barthelmy et al. 2005) onboard the *Swift* satellite (Gehrels et al. 2004), 38 blazars were found. Out of these 38, 12 were classified as BL Lacs and 26 as FSRQs.

The (14-195 keV) X-ray survey presented in Marcotulli et al. 2022 contains the most up-to-date BAT catalogue yet. Based on the BAT 105-month survey catalogue, in addition to the BAT AGN Spectroscopic Survey[1], 118 X-ray blazars were identified.

5.4 Gamma-ray luminosity function

The local gamma-ray luminosity function (GLF) is parameterized similar to the XLF, but with an additional photon index dependence modelled as a Gaussian (Ajello et al. 2012; Ajello et al. 2014), i.e.

$$\frac{d\Psi(L_\gamma, z=0, \rho)}{dL_\gamma} = \frac{A}{\ln(10) L_\gamma} \left[\left(\frac{L_\gamma}{L_*} \right)^{\gamma_1} + \left(\frac{L_\gamma}{L_*} \right)^{\gamma_2} \right]^{-1} \times \frac{dN(L_\gamma, \rho)}{d\rho}, \tag{5.20}$$

---

[1] `http://www.bass-survey.com/`

with

$$\frac{dN(L_\gamma, \rho)}{d\rho} = \exp\left[-\frac{(\rho - \mu(L_\gamma))^2}{2\sigma^2}\right] \tag{5.21}$$

and σ and $\mu(L_\gamma)$ being the Gaussian dispersion and mean, respectively. In our case, we assume the GLF to be independent of the photon index, i.e. setting the Gaussian distribution $dN/d\rho = 1$.

The redshift-dependent evolution term for the PLE and the PDE models takes the form

$$e(z) = (1+z)^{p_1^*(L_\gamma)} e^{z/p_2}, \tag{5.22}$$

with the luminosity-dependent index

$$p_1^*(L_\gamma) = p_1 + \tau \times (\log L_\gamma - 46). \tag{5.23}$$

The evolution term in the GLF LDDE model takes the same broken power-law shape as Equation (5.18), but with the spectral indices now being luminosity dependent, i.e.

$$p_1^*(L_\gamma) = p_1 + \tau(\log L_\gamma - \log L_p) \tag{5.24}$$

$$p_2^*(L_\gamma) = p_2 + \delta(\log L_\gamma - \log L_p), \tag{5.25}$$

and

$$z_*(L_\gamma) = z_\mathrm{c}\left(\frac{L_\gamma}{L_\mathrm{c}}\right)^\alpha . \tag{5.26}$$

5.4.1 Gamma-ray surveys

Since its launch in 2011, the *Fermi Gamma-Ray Space Telescope* has carried out all-sky surveys using its *Large Area Telescope* (LAT) imaging instrument (Atwood et al. 2009). We will focus on four different surveys. One reported in Ajello et al. 2012, containing 186 FSRQ sources, one reported in Ajello et al. 2014, containing 211 BL Lacs and one reported in Fukazawa et al. 2022 containing 61 Fermi/LAT detected radio galaxies.

CHAPTER

SIX

COSMOLOGICAL EVOLUTION AND MULTI-MESSENGER EMISSIVITY

The evolution of AGN is tightly linked to the evolution of large-scale structures in the Universe. The supermassive black hole influences the evolution of the galaxy through dynamics and feedback processes and jetted AGN are big providers of material into intergalactic regions. The activity of AGN is linked with star formation in the host galaxy, or conversely, quenching of star formation as the AGN outflows blow away the interstellar medium responsible for star formation. Thus, by studying the evolution of AGN, we can get further insight into both the evolution of general galaxies and large-scale structures of the Universe.

In the following chapter, we model the evolution and emissivity of different AGN categories based on different surveys performed in radio, X-rays and gamma rays (Section 6.1). In Section 6.2 we compare the emissivity of nearby AGN populations to the local flux of UHECRs and in Section 6.3 we compare the emissivity of individual populations to the diffuse neutrino flux. Finally, in Section 6.4 we investigate if the unification model from Chapter 3 is realizable.

6.1 AGN population evolution

6.1.1 Distance measures

To study how the different populations of AGN evolve over cosmological scales, we first need to define how we measure cosmic distances. In what follows, we adopt the distance measures presented by Hogg 1999.

We consider a flat lambda cold dark matter (FΛCDM) universe with *Hubble constant* $H_0 = 100\ h$ km s^{-1} Mpc^{-1}, where we set $h = 0.7$. The *Hubble distance* is defined as the speed of light divided by the Hubble constant,

$$D_{\mathrm{H}} \equiv \frac{c}{H_0}. \tag{6.1}$$

Following, it is useful to introduce the function

$$E(z) \equiv \sqrt{\Omega_{\mathrm{M}}(1+z)^3 + \Omega_{\mathrm{k}}(1+z)^2 + \Omega_{\Lambda}}, \tag{6.2}$$

where $\Omega_{\mathrm{M}}, \Omega_{\mathrm{k}}$ and Ω_{Λ} are the three dimensionless density parameters. For our adopted cosmology, $\Omega_{\mathrm{M}} = 0.3$, $\Omega_{\mathrm{k}} = 0$, i.e. a flat Universe, and $\Omega_{\Lambda} = 0.7$. This function is used when further considering the total *line-of-sight comoving distance*,

$$D_{\mathrm{c}} = D_{\mathrm{H}} \int_0^z \frac{dz'}{E(z')}. \tag{6.3}$$

If the Universe is considered to have some curvature, i.e. $\Omega_{\mathrm{k}} \neq 0$, the *transverse comoving distance* D_{M} becomes the relevant quantity for measuring distances properly. However, since we are assuming $\Omega_{\mathrm{k}} = 0$, the line-of-sight comoving distance and transverse comoving distance are the same,

$$D_{\mathrm{M}} = D_{\mathrm{C}}. \tag{6.4}$$

Finally, we need to consider the *angular diameter distance* D_{A}. This is the ratio of an object's transverse size to its angular size and relates to the transverse comoving distance as

$$D_{\mathrm{A}} = \frac{D_{\mathrm{M}}}{1+z}. \tag{6.5}$$

For later convenience, we also define the *luminosity distance* D_{L} as

$$D_{\mathrm{L}} = (1+z)D_{\mathrm{M}} = (1+z)^2 D_{\mathrm{A}}. \tag{6.6}$$

With all these relations in mind, we can finally express the *comoving volume* element as

$$dV = D_{\mathrm{H}} \frac{(1+z)^2 D_{\mathrm{A}}^2}{E(z)} d\Omega dz, \tag{6.7}$$

where $d\Omega$ is the solid angle. The comoving volume is a measure in which the number density of objects following exactly the Hubble flow remains constant with redshift. In the following sections, the comoving volume will be used to express the evolution features of our luminosity functions.

6.1.2 Luminosity distribution and population evolution

With our luminosity functions from Chapter 5 in hand, we can now use them to estimate how our AGN populations behave as a function of luminosity. For each population, we calculate the differential luminosity distribution by multiplying with the comoving volume, Equation (6.7), and integrating over a relevant bin in redshift,

$$\frac{dN(L)}{dL} = \int_{z_{\mathrm{min}}}^{z_{\mathrm{max}}} \frac{\Psi(L, V(z))}{dL} \frac{dV(z)}{dz} dz. \tag{6.8}$$

By additionally multiplying with the source luminosity, i.e. LdN/dL, we have a function that describes the luminosity distribution of our AGN populations.

The luminosity distribution for X-ray-selected radio galaxies and one of our X-ray-selected blazar populations is shown in Figure 6.1. The models are divided into four different bins in redshift ($0 < z < 2$, $2 < z < 4$, $4 < z < 6$, $6 < z < 8$), showing

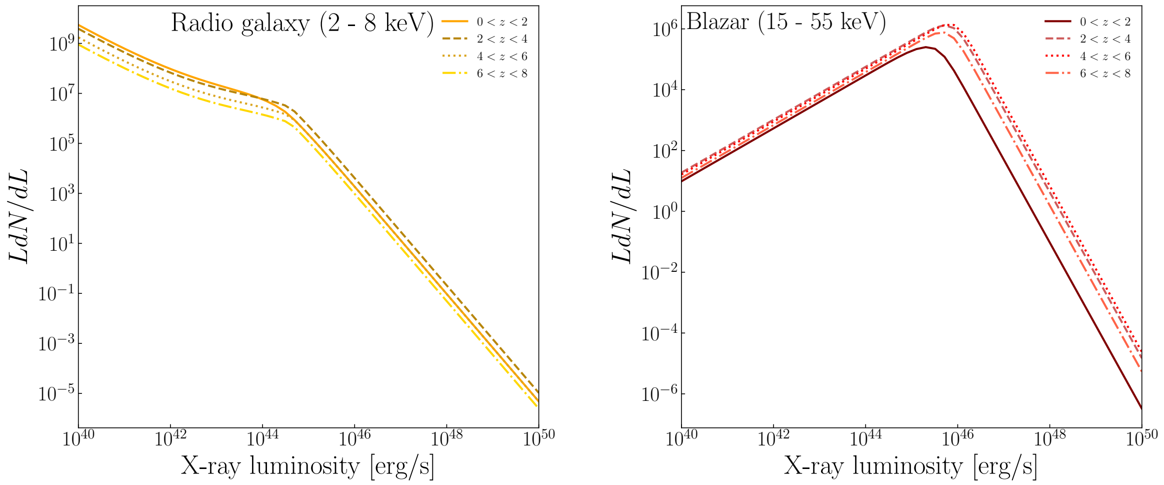

Figure 6.1: XLF of two different AGN populations from different surveys. *Left:* The radio galaxy population surveys in the 2 - 8 keV energy range from four different redshift ranges. *Right:* The blazar population surveys in the 15 - 55 keV band are shown in four different redshift ranges.

how the luminosity distribution varies at different cosmological epochs. The difference between the redshift ranges depends on the redshift evolution of the AGN population. For the remainder of this section, we consider our models for redshifts $0 < z < 10$. Figures showing the luminosity distribution for different redshift ranges can be found in Chapter B. From Figure 6.1, we note two different, distinct behaviours of our models.

The radio galaxies of Figure 6.1 show a clear break around a luminosity of $\sim 10^{45}$ erg/s in all redshift ranges. The softening of the XLF above the break means that we expect to find significantly fewer sources at higher luminosities. Below the break, despite the spectrum being flatter, it does not decrease. This means that our luminosity functions predict a continuous increase in the population at lower luminosity. Their behaviour below 10^{42} erg/s is simply an artefact of the modelling done for sources within the relevant luminosities, and its behaviour is not bound by observations. The same argument applies for luminosities above the ranges listed in Table 6.1. However, since the luminosity evolution LdN/dL drops rapidly with increasing luminosity, expanding the range to include higher luminosities does not significantly impact the population behaviour.

Model	**Luminosity range** $(\log L)$
RG (2 - 8 keV)	$42.0 < \log L < 47.0$
RG (2 - 10 keV)	$41.5 < \log L < 46.5$
Seyfert_0 (15 - 55 keV)	$41.0 < \log L < 47.0$
Seyfert (15 - 55 keV)	$41.0 < \log L < 47.0$
Blazar (15 - 55 keV)	$44.0 < \log L < 48.5$
FSRQ (15 - 55 keV)	$46.0 < \log L < 48.5$
BL Lac (15 - 55 keV)	$44.5 < \log L < 48.5$
Blazar (14 - 195 keV)	$43.7 < \log L < 48.4$
FSRQ (14 - 195 keV)	$43.7 < \log L < 48.4$
Blazar (0.1 - 100 GeV)	$43.0 < \log L < 52.0$
FSRQ (0.1 - 100 GeV)	$45.6 < \log L < 49.4$
BL Lac (0.1 - 100 GeV)	$43.8 < \log L < 48.4$
RG (0.1 - 300 GeV)	$40.5 < \log L < 46.0$
RG (151 MHz)	$24.0 < \log L < 30.0$[a]

Table 6.1: Luminosity ranges considered in the different models. The ranges are bound by observed AGN in their respective surveys. The luminosity L is in units of erg/s. [a]The 151 MHz radio galaxy model is in units of W Hz^{-1} sr^{-1}.

The luminosity distribution for all models shows a softening above a certain luminosity. This is to be expected, as at some point there must be an upper limit to how bright AGN can become. What differs is their behaviour below the break luminosity. The blazar population in Figure 6.1 shows, as opposed to the radio galaxies, a decrease in LdN/dL below the break. Thus, extending to either lower or higher luminosities only includes an insignificant amount of their population. Figure 6.2 shows that the X-ray-selected blazar populations follow this behaviour. For all other models, however, there is no clear peak in the luminosity distribution LdN/dL and we need to be considerate when selecting the lower end of the luminosity bins. The luminosity ranges of all our models are summarized in Table 6.1 We will use these for the number density and redshift evolution considered in the following sections.

The different behaviour of the blazars compared to the other AGN populations is caused by strong beaming effects. When observing the blazar population, the ultrarelativistic jet is beamed in our direction, causing the observed luminosity to be enhanced. For strongly beamed sources, the intrinsic luminosity $\mathcal{L}$ is related to the observed luminosity L through $L = \delta^{\zeta}\mathcal{L}$, where the exponent ζ depends on the jet and emission parameters (Urry & Shafer, 1984). This also alters the shape of the luminosity functions. For beamed sources, even if the intrinsic luminosity function follows a power-law distribution, it will be observed to fit a broken power-law (Urry & Padovani, 1991). Without this beaming effect, the blazar luminosity distributions below the break would follow more closely their behaviour above it. Thus, the ultrarelativistic beaming of blazar jets reduces the inferred number of sources at lower luminosities relative to unbeamed AGN.

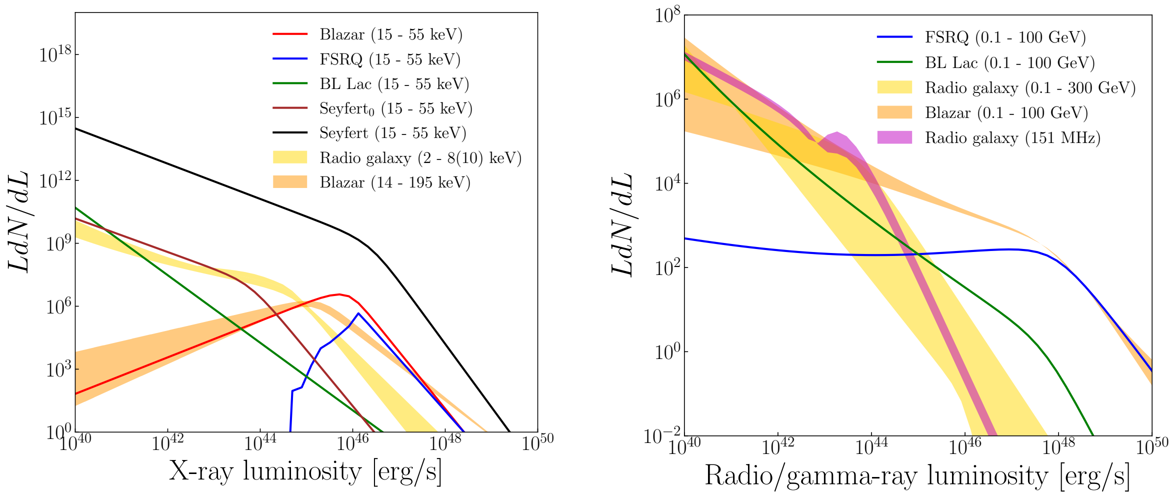

Figure 6.2: Luminosity distribution of all considered AGN populations. All models are binned in redshift between $0 < z < 10$. *Left:* Luminosity distribution of source populations selected from different X-ray surveys. The yellow and orange areas show the extent of the different XLF models for the same population sampled by the same surveys. The Seyfert population with a "0" subscript (brown) shows the model without an evolution parameter. *Right:* The luminosity distribution of both radio and gamma-ray selected populations. The yellow and orange areas indicate the spread of different GLF considered when modelling their respective population. The purple region shows the extent of the three different RLF models for the 151 MHz radio galaxy population.

Figure 6.2 shows the luminosity distribution of all our AGN populations. Except for the X-ray-selected BL Lacs, all populations show a clear break in their luminosity distribution followed by a steepening at higher luminosities. The parameters for all models are listed in Table 6.2 (XLF), Table 6.3 (GLF) and Table 6.4 (RLF).

The X-ray (left) luminosity distribution shows two models for the Seyfert population. The brown line shows a PLE model where the evolution function $e(z) = 0$, whereas the black Seyfert model evolves according to Equation (5.13). Both Seyfert models show an increase in population at lower luminosity. Due to its strong redshift evolution (see Figure 6.3), the black Seyfert model shows a much stronger luminosity density than the others. This Seyfert model dominates the X-ray luminosity and corresponds well to independent observations, which point to AGN line-emission being the dominant source of the universal X-ray background (Ajello et al. 2008). The yellow area covers the luminosity distribution of two LDDE models of radio galaxies in the 2 - 8 and 2 - 10 keV energy ranges. Both of these follow a broken power law in luminosity, Equation (5.12), with the evolution term of Equation (5.16). They both show a break above 10^{44} erg/s and steepen afterwards. The orange area covers the three different blazar models considered in the 14 - 195 keV energy range. It contains a general blazar population, as well as FSRQ and BL Lac blazar sub-populations. They all show a clear peak just above 10^{45} erg/s, with a harder spectrum above the peak. All these models consist of a broken power law with the evolution factor of Equation (5.15). Most of the population is concentrated close to the peak. The red line shows the general 15 - 55 keV blazar population. This model also shows a clear peak at luminosities slightly above the 14 - 195 keV blazar peak, and so we expect to also find the majority of this blazar population around the peak. The blue line shows the 15 - 55 keV selected FSRQ population. Similar to the other blazar populations, the FSRQs also show a clear peak, and most of their population is found around 10^{46} erg/s. Due to the low value of its γ_1-index, we need to be careful when considering its valid luminosity range. Therefore, it is strongly constrained in luminosity, with a lower limit of 10^{46} erg/s. Below this limit, the luminosity becomes too small of a number for the standard floating-point object in Python to handle, and thus the numerical integration cannot be performed. The final (green) X-ray model is for the 15 - 55 keV selected BL Lac population. For this model, we have used a simple power law, Equation (5.11), and thus no break appears. Its evolution term does not contribute to the shape of the luminosity density, and thus it remains a featureless, solid line.

The right part of Figure 6.2 shows the luminosity distribution of all gamma-ray-selected AGN populations, as well as the radio-selected population. The yellow area shows the distribution of the different 0.1 - 300 GeV selected radio galaxy models of Fukazawa et al. 2022. We will further only consider the best-fit LDDE model. The orange area covers all three (PLE, PDE, LDDE) models for the general blazar population at 0.1 - 100 GeV. We consider all three models, as there was no clear conclusion as to which one gave the best fit to observations (Ajello et al. 2015). The blue (green) lines show the luminosity density of the 0.1 - 100 GeV FSRQ (BL Lac) population. In contrast to their X-ray-selected counterparts, neither the general gamma-ray blazar population nor the FSRQs or BL Lacs show a clear peak where most of the population resides. The purple area shows the extent of the luminosity distribution of the 151 MHz radio-selected radio galaxies. For this population, we can clearly see the result of splitting the luminosity function into a low- and high-energy part by its behaviour at $L \sim 10^{43}$ erg/s.

	Power-law parameters				**Evolution parameters**					**Survey**
Model	A^{a}	L_*^{b}	γ_1	γ_2	p_1	p_2	z_{c}	$L_{\mathrm{c}}^{\mathrm{b}}$	α	**energy range**
RG (LDDE)	8.375×10^{-7}	2.14	2.15	1.10	4.00	-1.50	1.9	3.98	0.317	2 - 8 keV
RG (LDDE)	50.40×10^{-7}	0.871	0.86	2.23	4.23	-1.50	1.9	3.98	0.335	2 - 10 keV
Seyfert[c] (mPLE)	0.909×10^{-5}	0.61	0.80	2.67	0	0	–	–	–	15 - 55 keV
Seyfert (mPLE)	0.778×10^{-5}	0.61	0.84	3.01	2.62	0	–	–	–	15 - 55 keV
Blazar (mPLE)	1.379×10^{-7}	1.81	-0.87	2.73	3.45	-0.25	–	–	–	15 - 55 keV
FSRQ (mPLE)	0.175×10^{-7}	2.42	-50	2.49	3.67	-0.30	–	–	–	15 - 55 keV
BL Lac (PLE)	0.830×10^{-7}	1	–	2.61	-0.79	0	–	–	–	15 - 55 keV
Blazar (mPLE)	$^{d}1.69 \times 10^{-7}$	1.47	-0.51	1.79	2.79	-2.23	–	–	–	14 - 195 keV
FSRQ (mPLE)	$^{d}1.13 \times 10^{-7}$	1.01	-1.00	1.67	3.23	-1.62	–	–	–	14 - 195 keV

Table 6.2: Overview of the fitted parameters for all considered XLF models. The 2 - 8 keV RG model parameter fit was performed by Silverman et al. 2008 and the 2- 10 keV RG model parameter fit was performed by Ueda et al. 2003. All the 15 - 55 keV selected source population parameters were fit by Ajello et al. 2009 and the more recent 14- 195 keV populations were fitted by Marcotulli et al. 2022. LDDE is a luminosity dependent density evolution model, sPLE is a simple power-law pure luminosity evolution model and mPLE is a modified (broken power-law) pure luminosity evolution. The missing parameters are not needed for their respective models. [a]The normalization constant A has dimensions of Mpc^{-3}. [b]Luminosity in units of 10^{44} erg/s. [c]Model showing no evolution. [d]The normalization constant A differs by 10^{-7} from what was tabulated by Marcotulli et al. 2022.

	Power-law parameters				**Evolution parameters**								**Survey**
Model	A	L_*^{d}	γ_1	γ_2	p_1	p_2	z_{c}	L_{c}	α	τ	δ	L_{p}	**energy range**
Blazar (PLE)	19.3^{a}	8.75	3.19	1.14	4.41	-0.43	–	–	–	0.91	–	10^{46}	0.1 - 100 GeV
Blazar (PDE)	1.22^{a}	44.0	2.80	1.26	12.14	-0.15	–	–	–	2.79	–	10^{46}	0.1 - 100 GeV
Blazar (LDDE)	196^{a}	105	0.50	1.83	3.39	-4.96	1.25	10^{48}	0.0723	3.16	0.64	10^{46}	0.1 - 100 GeV
FSRQ (LDDE)	3.06^{b}	84.0	0.21	1.58	7.35	-6.51	1.47	10^{48}	0.21	–	–	–	0.1 - 100 GeV
BL Lac (LDDE)	1.04^{b}	50.0	0.58	1.99	2.30	-4.30	1.18	10^{48}	0.0862	4.62	–	10^{46}	0.1 - 100 GeV
RG (LDDE)	2.82^{c}	1	5.00	1.40	3.40	-13.00	$10^{-8.25}$	$10^{42.5}$	0.045	–	–	$10^{42.5}$	0.1 - 300 GeV

Table 6.3: Overview of fitted parameters for the considered GLF models. The 0.1 - 100 GeV blazar models parameter fit was performed by Ajello et al. 2015. The 0.1 - 100 GeV FSRQ model parameter fit was performed by Ajello et al. 2012. The 0.1 - 100 GeV BL Lac model parameter fit was performed by Ajello et al. 2014. The 0.1 - 300 GeV radio galaxy model parameter fit was performed by Fukazawa et al. 2022. [a]Normalization constant in units of 10^7 Mpc^{-3}. [b]In units of 10^{-9} Mpc^{-3}. [c]In units of 10^{-12} Mpc^{-3}. [d]Break luminosity in units of 10^{46} erg/s.

	Power-law parameters						**Evolution parameters**					**Survey**
Model	$A_{\mathrm{l}}^{\mathrm{a}}$	$L_{\mathrm{l*}}^{\mathrm{b}}$	α_{l}	$A_{\mathrm{h}}^{\mathrm{a}}$	$L_{\mathrm{h*}}^{\mathrm{b}}$	α_{h}	k_{l}	z_{l}	z_{h0}	z_{h1}	z_{h2}	**frequency**
$\mathrm{RG_A}$ (LDDE)	0.314	2.88	0.584	1.820	26.30	2.42	3.60	0.710	2.23	0.642	–	151 MHz
$\mathrm{RG_B}$ (LDDE)	0.328	2.95	0.581	1.528	22.91	2.40	3.11	0.580	1.77	0.0483	–	151 MHz
$\mathrm{RG_C}$ (LDDE)	0.300	3.02	0.586	1.750	24.55	2.42	3.48	0.710	2.03	0.568	0.956	151 MHz

Table 6.4: Overview of fitted parameters for all considered RLF models. All three models were parameterized by Willott et al. 2001 for a $\Omega_{\mathrm{M}} = 0$ Universe. The "l" ("h") subscript refers to the low (high) luminosity part of the combined RLF. [a]Normalization in units of 10^{-7} Mpc^{-3}. [b]Break luminosity in units of 10^{26} W Hz^{-1} sr^{-1}.

6.1.3 Number density and redshift distribution

We are now interested in studying how the number density and redshift distribution of our AGN populations change with redshift. We compute the number density of our models by performing a simple luminosity integral of our luminosity functions,

$$n(z) = \frac{dN(z)}{dV(z)} = \int_{L_{\min}}^{L_{\max}} \frac{d^2N(L, V(z))}{dLdV(z)} dL = \int_{L_{\min}}^{L_{\max}} \frac{\Psi(L, V(z))}{dL} dL. \tag{6.9}$$

Additionally, the redshift distribution is found by multiplying with the comoving volume,

$$\frac{dN(z)}{dz} = \int_{L_{\min}}^{L_{\max}} \frac{\Psi(L, V(z))}{dL} \frac{dV(z)}{dz} dL. \tag{6.10}$$

The luminosity integral limits are listed in Table 6.1.

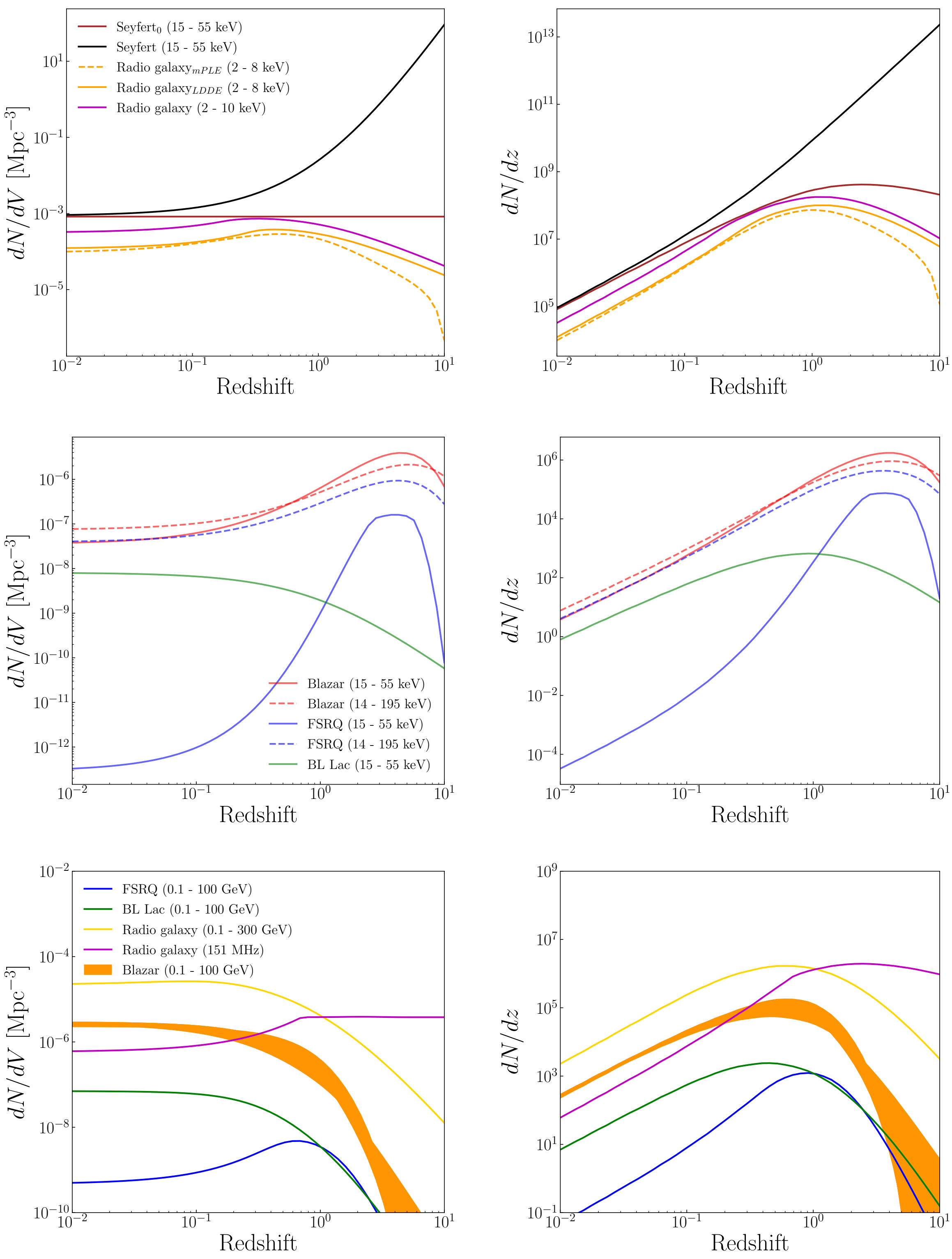

Figure 6.3: Number density (left) and redshift distribution (right) as a function of redshift for all considered AGN populations. *Upper:* X-ray selected Seyfert and radio galaxies. *Middle:* X-ray selected blazar models. The red lines show two different models for a general blazar population. The two blue lines show the two different X-ray FSRQ models. *Bottom:* Gamma-ray and radio models. The orange area covers all (PLE, PDE, LDDE) gamma-ray selected blazar models. Luminosity bins for all models are summarized in Table 6.1.

Figure 6.3 shows the number density (left) and redshift distribution (right) of all our models. The upper figures show the X-ray-selected radio galaxy and Seyfert populations. Here, it can be seen that the Seyfert model with no evolution (brown) has a constant number density, and its shape traces therefore exactly the evolution of the comoving volume. The second (black) Seyfert population shows a strong redshift evolution. The most distant sources in this survey were observed at redshift ~ 1, and thus the behaviour of the number density evolution above this redshift is not bound by observations. We note that both Seyfert modes are the most numerous AGN populations, which agrees with independent observations of the local Universe.

The upper part of Figure 6.3 shows three different models for X-ray selected radio galaxy populations. We include both the PLE and the LDDE model from the 2 - 8 keV surveys as both models fit the observation equally well (Silverman et al. 2008). All three radio galaxy models show the same behaviour, being less numerous than the Seyfert population, and increasing in number density until $z \sim 0.3$ for the 2 - 10 keV model and $z \sim 0.5$ for the 2 - 8 keV model. After which, they become less numerous as we look towards earlier epochs.

The middle plots of Figure 6.3 show the X-ray selected blazar populations. The number density of both the general blazar (red) and FSRQ (blue) models behave similarly. It is almost constant in the local ($z < 0.1$) Universe, and as we look farther away their number density increases. This increase continues to around $z \sim 3 - 4$, where we find the peak of the general blazar and FSRQ populations. Looking at even earlier epochs, they all decrease. This agrees with independent observations of FSRQs, as they are generally found at higher redshifts. We note the obvious difference in number density for the two FSRQ models. The 15 - 55 keV model shows 5 orders lower number density in the local Universe and evolves much stronger with redshift. The BL Lac population is the only X-ray model that shows a pure negative number density evolution. This is in agreement with independent observations, as most of the BL Lac AGN are found at relatively low redshift.

The bottom plots of Figure 6.3 show all gamma-ray selected populations, as well as the radio-selected radio galaxy population. The 151 MHz radio galaxy models show similar behaviour to that of the X-ray-selected radio galaxies. They evolve positively in density for a while, before reaching a maximum. The radio-selected population, however, does not drop off at earlier epochs but rather stays constant. In gamma-rays, the radio galaxy (0.1 - 300 GeV) number density evolves negatively with redshift for all epochs, meaning that the number of bright gamma-ray radio galaxies was lower in the earlier Universe. This was discussed in Fukazawa et al. 2022, where they argued that either beaming effects or the soft SED causes FRII radio galaxies to appear fainter in gamma-rays compared to X-rays and radio. If this is the case, we miss the majority of the FRII population at higher redshifts. The gamma-ray selected general blazar population (orange) shows similar behaviour to that of the (0.1 - 300 GeV) radio galaxies. Their number density is close to constant in the nearby ($z < 0.1$) Universe but softens at larger redshifts. Unexpectedly, they are more numerous in the local Universe than the radio-selected radio galaxies and this requires a couple of comments.

Firstly, from Figure 6.2 we remember that the luminosity distribution of gamma-ray blazars continues to increase with decreasing luminosity, and thus the lower limit for the luminosity integral of Equation (6.9) determines their number density. In Ajello et al.

2015, they give no clear explanation as to why they choose a luminosity limit as low as 10^{43} erg/s. It is likely that there are no blazars to be found in this region, and this limit should be set at a higher luminosity. This will generally reduce the number density of the blazar populations at all epochs. Secondly, the 151 MHz RLF as parameterized by Willott et al. 2001 cannot be constrained at higher redshifts for the low-luminosity population. Thus, their number density may evolve more strongly than what Figure 6.3 shows.

The gamma-ray selected BL Lac population show similar behaviour to the general gamma-ray blazar population. Their number density is seemingly constant at low redshifts and drops significantly when $z \gtrsim 0.3$. The FSRQ population is the only gamma-ray model with a number density that evolves positively with redshift. They peak at $z \sim 0.8$, before decreasing like the rest. As the general blazar population consists of both FSRQs and BL Lacs, the behaviour of these sub-categories should be visible in the general population. We see that the more numerous BL Lac population dominates at lower redshift, with the same shape as the general population. When the FSRQs become more numerous, the BL Lac population is decreasing, which is also the case for the general blazar population.

Finally, we note that generally, the gamma-ray-selected blazar populations seem more numerous in the local Universe than the X-ray-selected blazar populations. They evolve negatively with increasing redshift, whereas most of the X-ray populations evolve positively. At early epochs, $z \gtrsim 2$, X-ray blazars are more numerous than their gamma-ray counterparts. As discussed earlier, the lower luminosity limit might cause us to overestimate the gamma-ray blazar population. If this is the case, then we conclude instead that blazars are more numerous in X-rays than gamma-rays for all epochs. This, in addition to cosmological redshift, could explain their different behaviours. The radio galaxy populations show generally a higher number density in X-rays than gamma-rays.

6.1.4 Redshift evolution

Before we compare the prediction of our luminosity functions to the emissivity of UHECRs and neutrinos, we want to quickly compare the number density evolution of our models to the star formation rate. Over cosmological distances, the density of any astrophysical objects can be expressed as their local number density ($z = 0$) times an evolution function,

$$\rho(z) = \rho(z = 0) \times (1 + z)^{a(z)}. \tag{6.11}$$

For the star formation rate, this $a(z)$ function is well-researched and takes the form (Yüksel et al. 2008)

$$a(z) = \begin{cases} 3.4 & \text{for } z < 1 \\ -0.3 & \text{for } 1 \leq z \leq 4 \\ -3.5 & \text{for } z > 4 \end{cases} . \tag{6.12}$$

For our luminosity functions, we find the corresponding $a(z)$ function from dividing the number density evolution into ranges in redshift where a constant number characteristically describe their evolution for that range. The results of this procedure are shown in Figure 6.4, with the corresponding values of $a(z)$ listed in Table 6.5. We see that the evolving Seyfert population and the 15–55 keV FSRQ population are the only models that evolve significantly stronger compared to the star formation rate. The other models evolve comparatively with the star formation rate, or more negatively. In the somewhat

Model	**Evolution index a(z)**
Seyfert_0	0
Seyfert	5
Radio galaxy (2 - 8 keV)	4, for $z < 0.4$ -1, for $z > 0.4$
Radio galaxy (2 - 10 keV)	4, for $z < 0.3$ -1.5, for $z > 0.3$
Radio galaxy (0.1 - 300 GeV)	2, for $z < 0.1$ -3, for $z > 0.1$
Radio galaxy (151 MHz)	3.5, for $z < 0.8$ 0, for $z > 0.8$
Blazar (15 - 55 keV)	5, for $z < 0.3$ 3, for $0.3 \leq z \leq 4$ -3, for $z > 4$
Blazar (14 - 195 keV)	3.5, for $z < 0.3$ 2, for $0.3 \leq z \leq 4$ -1.5, for $z > 4$
Blazar (0.1 - 100 GeV)	-5
FSRQ (15 - 55 keV)	12, for $z < 1$ 8, for $1 \leq z \leq 5$ -7, for $z > 5$
FSRQ (14 - 195 keV)	3, for $z < 1$ 1, for $1 \leq z \leq 5$ -2, for $z > 5$
FSRQ (0.1 - 100 GeV)	5, for $z < 0.6$ -6, for $z > 0.6$
BL Lac (15 - 55 keV)	-2
BL Lac (0.1 - 10 GeV)	-5

Table 6.5: Density evolution index for all considered models.

local Universe, most of our models show similar behaviour to the star formation rate. This is not surprising, as the star formation rate is thought to be linked to the activity of the galactic nuclei (e.g. Harrison 2017).

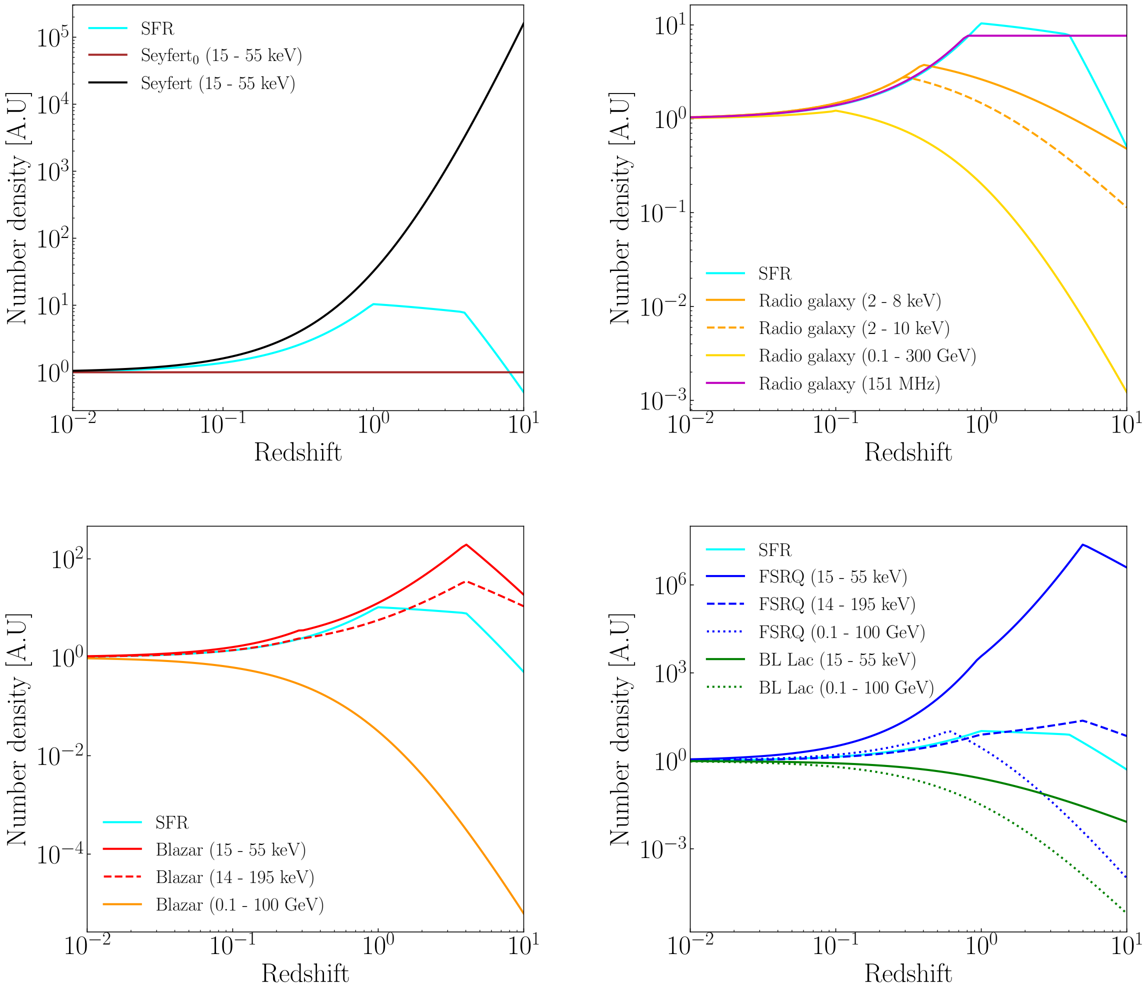

Figure 6.4: Density evolution index for different AGN categories compared to the star formation rate. *Upper left:* Both X-ray-selected Seyfert models. *Upper right:* Radio, X-ray and gamma-ray selected radio galaxy models. *Lower left:* X-ray and gamma-ray general blazar population models. *Lower right:* X-ray and gamma-ray selected FSRQ and BL Lac models.

6.1.5 Characteristic luminosity

Now that we know how our models evolve in both luminosity and density, we will consider their total energy output, also known as *emissivity*. The luminosity density is a measure of how much energy is released in total by our population per volume,

$$Q(z) = \int_{L_{\min}}^{L_{\max}} L \frac{\Psi(L, V(z))}{dL} dL. \tag{6.13}$$

Dividing by the number density $n(z)$, we define the *characteristic luminosity* as

$$\mathcal{L}(z) = \frac{Q(z)}{n(z)} = \frac{\int_{L_{\min}}^{L_{\max}} L \frac{\Psi(L, V(z))}{dL} dL}{\int_{L_{\min}}^{L_{\max}} \frac{\Psi(L, V(z)}{dL} dL}. \tag{6.14}$$

This is the expected luminosity for any of our AGN models at a given redshift. The characteristic luminosity, as well as the luminosity density, is shown in Figure 6.5 as a function of redshift. The majority of the models show an increase in characteristic luminosity towards higher redshifts. The luminosity density depends heavily on the number density evolution and their behaviour is similar. The shape of the characteristic luminosity distribution reflects the difference between the luminosity density evolution and the number density evolution. The small "bumps" at high redshift for the X-ray FSRQ and gamma-ray radio galaxies are therefore nothing but small deviations between the behaviour of the number density and luminosity density evolution. In the local Universe, all AGN populations have an almost constant characteristic luminosity, which becomes important when considering their UHECR emissivity.

Compared to the local number density and luminosity derived from other surveys and presented in Murase & Fukugita (2019), we see that the number density of our X-ray selected radio galaxies agrees with the number density range for their AGN (X) population. However, our luminosity is significantly lower. The number density of our gamma-ray selected FSRQ and BL Lac populations agrees with their lowest estimate, but our FSRQ model shows much stronger luminosity. For our gamma-ray radio galaxies, the number density agrees with the highest estimate from Murase & Fukugita (2019), however, our predicted luminosity is around a decade lower. Considering the significant uncertainty they state in their paper, and the uncertainty connected to the luminosity integration limits in our case, we cannot state any obvious disagreements.

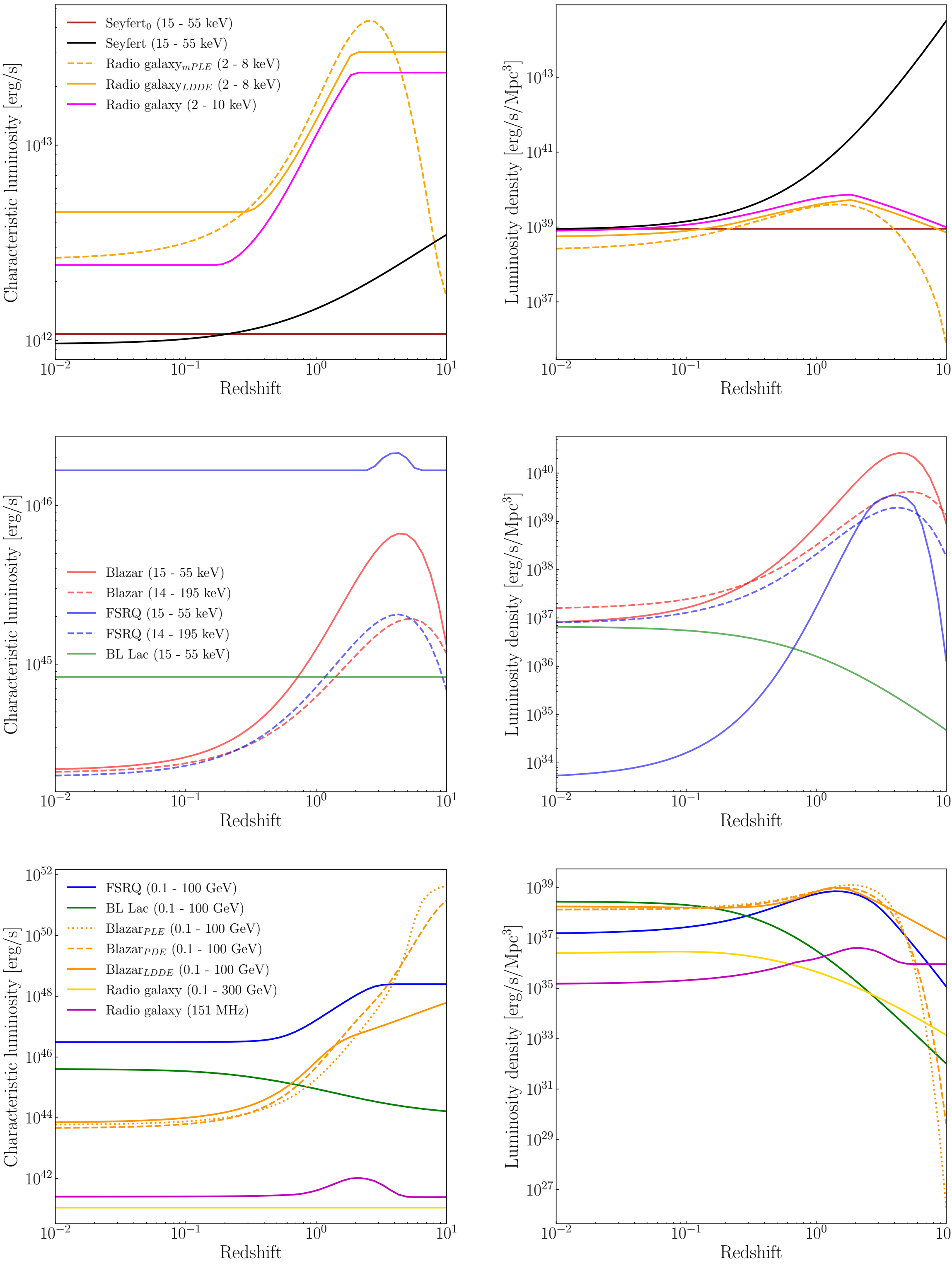

Figure 6.5: Characteristic luminosity (left) and luminosity density (right) as a function of redshift for all source populations. All models are the same as for Figure 6.3.

6.2 UHECR emissivity

Studying the non-thermal electromagnetic emission from AGN populations naturally hints at the possible emissivity of other messengers. We will therefore compare our results for the X-ray, gamma-ray and radio emission from AGN populations to the observed energy density of UHECRs. In the following, UHECRs will refer to energies above 6×10^{17} eV.

For any astrophysical object to be considered a source of UHECRs they need to fulfil the Hillas condition. As discussed in Chapter 2, AGN satisfy the condition and are considered as possible source candidates of UHECRs.

Based on observations and complementary simulations (Unger et al. 2015), the Pierre Auger Collaboration has estimated the local emissivity of UHECRs above 6×10^{17} eV (Pierr Auger Collaboration, 2023). This predicted emissivity reads

$$L \times n = 3 \times 10^{44} \frac{\text{erg}}{\text{Mpc}^3\text{yr}}, \tag{6.15}$$

and is shown as the blue diagonal line in Figure 6.6 and Figure 6.7. When studying single source populations, the product between the number density and the characteristic luminosity gives the emissivity of that population. Thus, we proceed to compare the estimated emissivity of our AGN models to the local emissivity of UHECRs.

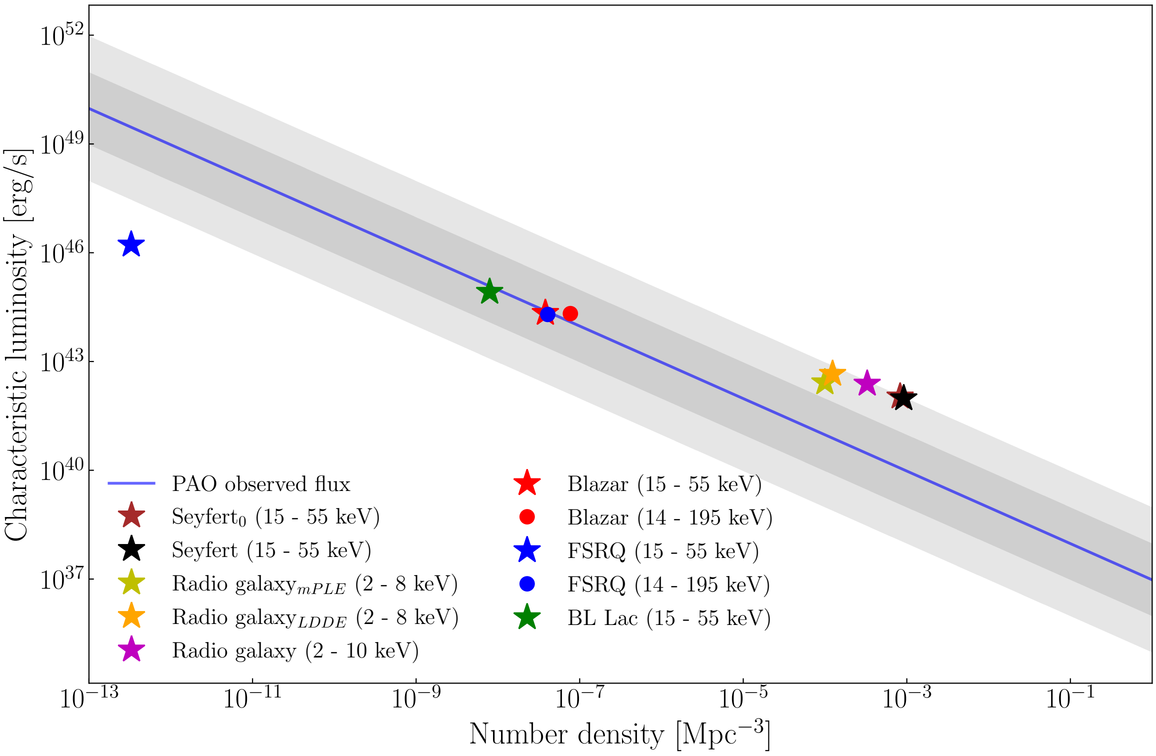

Figure 6.6: Emissivity of X-ray source populations at redshift $z = 0.01$ compared to the measured emissivity of UHECR. The diagonal blue line is the UHECR flux measured by the Pierre Auger Observatory. The dark (light) grey regions show one (two) powers above and below the UHECR flux.

Figure 6.6 shows the emissivity of all AGN X-ray populations compared to the local emissivity of UHECRs. Both the number density and the characteristic luminosity of the sources are sampled at redshift $z = 0.01$ from the number density and luminosity distributions presented earlier. As the flux of UHECRs needs to be of local origin (see Chapter 2), choosing a lower redshift is reasonable. In addition, both the characteristic luminosity (Figure 6.5) and the number density (Figure 6.3) are close to constant for $z \lesssim 0.1$. Similar plots for different redshifts are found in Chapter B.

AGN populations located within the grey region of Figure 6.6 can by themselves produce a significant amount of the local flux of UHECRs if their corresponding emissivity is comparable to that of X-rays. All our X-ray AGN population models fall within this range, except for the 15 - 55 keV FSRQs. For example, both the 15 - 55 keV general blazar model and the 14 - 195 keV FSRQ model lie on the blue line and require an emissivity of UHECRs equal to that of X-rays to account for the local flux of UHECRs. Both Seyfert models are located at the edge of the light-grey region and thus would require only $\sim 1\%$ of their X-ray emissivity in UHECRs. The three radio galaxy models appear at slightly different locations, but all show sufficient X-ray emissivity to power the local UHECR flux.

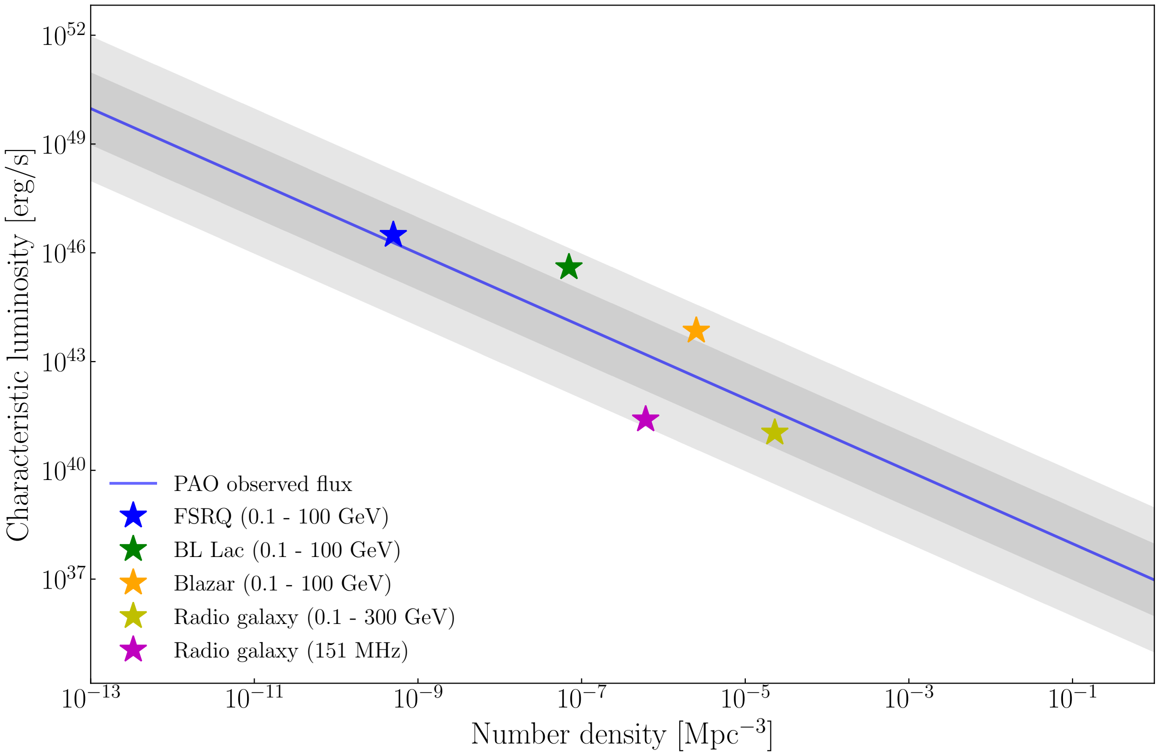

Figure 6.7: Emissivity of gamma-ray and radio source populations at redshift $z = 0.01$ compared to the measured emissivity of UHECR. The diagonal lines are the same as for Figure 6.6.

Figure 6.7 shows the emissivity of UHECRs compared to the emissivity of all gamma-ray and radio models at redshift $z = 0.01$. The source populations vary in comparison to the X-ray models in Figure 6.6. The gamma-ray selected radio galaxies fail to produce the full flux, only reaching $\sim 30{-}40\%$. The 151 MHz selected radio galaxy population (purple) can account only for $\sim 2 - 3\%$ of the UHECR population. Despite their number density being relatively high (Figure 6.3), the local, characteristic luminosity (Figure 6.5) of these sources make them insufficient standalone UHECR sources. Both blazar sub-categories can by themselves produce the local flux, with the FSRQs needing about $80-90\%$ of their gamma-ray emissivity in UHECRs, whilst the BL Lacs require only $2-3\%$. The gamma-ray sampled general blazar population requires also only a fraction of the gamma-ray energy in UHECRs.

Conclusion

If the total UHECR emissivity of AGN is comparable to their emissivity in X-rays or gamma-rays, most AGN populations can produce the observed flux of UHECRs. Within the AGN sub-populations, Seyfert galaxies and X-ray-selected radio galaxies show a higher emissivity and are more comfortably UHECR sources. The radio galaxy population constructed from radio observations can only contribute with $\sim 2-3\%$. The only other model that cannot produce the flux is the 15 - 55 keV FSRQ population, however, as their unbeamed counterpart (radio galaxies) are sufficient producers, the combined populations of high-power AGN would suffice to reach 100%.

6.3 Neutrino emissivity

The neutrino emissivity might be directly linked to the gamma rays originating from AGN, as when energetic protons decay through pions, a comparative amount of energy is carried away by both gamma rays and neutrinos. This simple argument places an upper limit on the neutrino emission, as gamma rays could also originate from the inverse Compton scattering of e.g. synchrotron photons. As the gamma-ray emission originates in the strongly beamed jets that some AGN populations lack, the X-ray and radio emission can also be used to probe the neutrino emissivity. The X-ray luminosity traces directly the accretion power of AGN, which is linked to the possible acceleration of energetic protons. The X-ray-selected populations may therefore also trace the neutrino production. For jetted AGN, their radio emissions are linked to the power of the jet which again reflects the power of the central engine. Thus, we investigate also the radio-selected population for neutrino emission. For energetic neutrinos to be produced, we require a highly energetic proton population. The Hillas criterion is therefore equally relevant for the neutrino case.

The diffuse neutrino flux is measured by IceCube (Abbasi et al. 2022) and fitted by the power law

$$E_\nu^2 \Phi_\nu = 1.44 \times 10^{-8} \times \left(\frac{E_\nu}{100\mathrm{TeV}} \right)^{-2.37} \mathrm{GeV cm^{-2} s^{-1} sr^{-1}}. \tag{6.16}$$

We compare the emissivity of our AGN populations to the observed diffuse neutrino flux through (Palladino et al. 2020)

$$E_\nu^2 \Phi_\nu = \int\limits_z \frac{D_\mathrm{H}}{E(z)} \frac{\mathcal{L}_\nu(z)}{4\pi(1+z)^2} n_0 dz, \tag{6.17}$$

where $\mathcal{L}_\nu$ is the characteristic luminosity of Equation (6.14), $E(z)$ is given by Equation (6.2) and D_H is the Hubble distance (Equation (6.1)). The number density evolution is already included in $\mathcal{L}_\nu$, and thus we multiply by the local number density $n_0 = n(z=0)$, instead of the full $n(z)$. The results of applying Equation (6.17) to all our AGN models are shown in Figure 6.8.

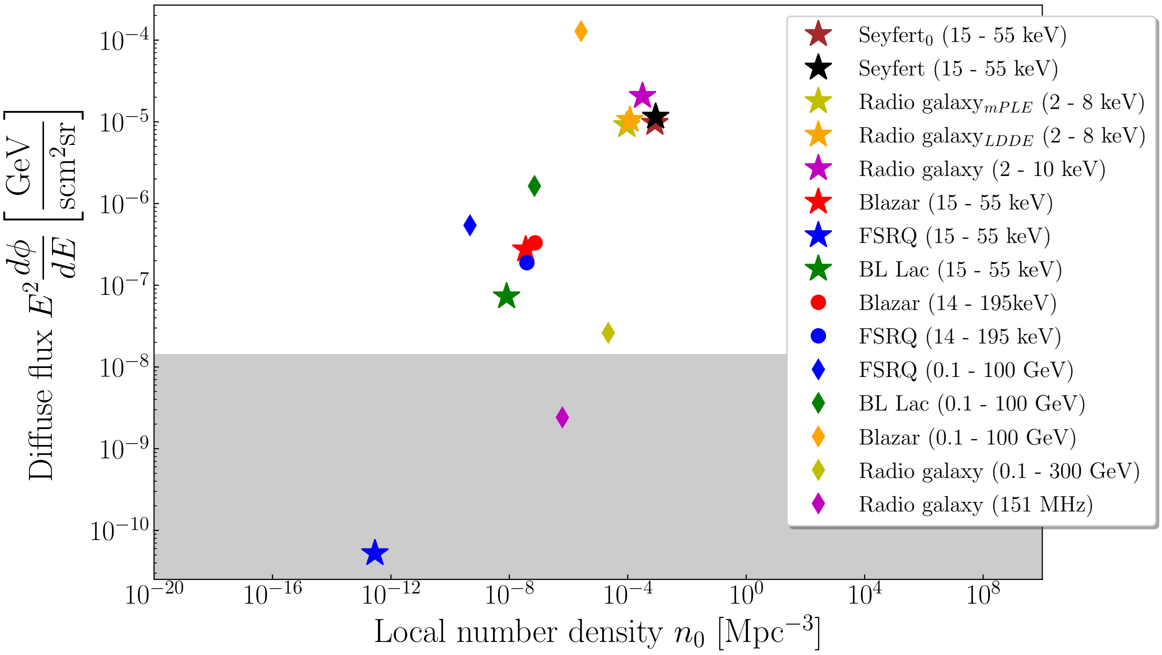

Figure 6.8: Predicted neutrino emissivity of all AGN populations up to redshift $z = 5$. The shaded area indicates a diffuse neutrino flux below the IceCube prediction at 100 TeV neutrino energy. The characteristic luminosity of all models was calculated using the energy bins listed in Table 6.1. The 0.1 - 100 GeV blazar population (orange diamond) is the LDDE model.

Figure 6.8 shows the predicted neutrino emissivity of all AGN models. The redshift integral of Equation (6.17) is performed from $z = 0$ to $z = 5$. The shaded area corresponds to a diffuse neutrino flux below the predicted IceCube limit. Only the 15 - 55 keV FSRQ and 151 MHz radio galaxy models fall within this region. Despite the strong X-ray luminosity of individual FSRQs, their low number density in the local Universe is not compensated sufficiently by their strong redshift evolution and thus they contribute an insignificant amount to the total diffuse neutrino flux. The 151 MHz selected radio galaxy population can only account for 10% if their neutrino emissivity corresponds to their respective X-ray and radio power.

By assuming all other sources have the same emissivity in neutrinos as in their respective X-rays or gamma-rays, we note the following results: The gamma-ray selected radio galaxy population would produce around twice the observed diffuse neutrino flux. The X-ray sampled BL Lac population would produce around six times the flux. The 15 - 55 keV X-ray blazar population, 14 - 195 keV X-ray blazar and FSRQ populations could produce $10-30$ times the observed neutrinos. The gamma-ray FSRQ population could produce $40-50$ times the observed neutrinos. The gamma-ray BL Lac population would produce ~100 times the diffuse neutrino flux. The X-ray radio galaxy and Seyfert populations could produce $\sim 10^3$ times the observed neutrinos. Finally, the gamma-ray predicted blazar population could produce up to $\sim 10^4$ times the observed diffuse neutrino flux. However, keeping in mind our earlier discussion regarding this blazar model, this emissivity is most likely significantly overestimated. By increasing the lower luminosity limit for this blazar model by one or two powers, the neutrino luminosity decreases correspondingly with a similar amount.

Conclusion

Assuming all AGN populations have a similar neutrino emissivity to that of either radio, X-rays or gamma-rays, all but two of our population models can by themselves produce the predicted 100 TeV diffuse neutrino flux. The numerously sparse, but strongly evolving X-ray FSRQ models and the radio-detected radio galaxy population are the only models that fall below the IceCube limit.

6.4 Population unification

As discussed in Section 3.2, there are strong reasons to believe that blazars and radio galaxies are the same astrophysical objects, differing only by their orientation relative to us. In this section, we will therefore explore the possibility of the radio galaxies being possible parent populations for the blazars.

To obtain an estimate of the possible missed blazars, we introduce a correction function Θ_{CF} to account for their misalignment. This correction factor is defined as the ratio between the solid angle of a full sphere to the solid angle the emitted jet projection covers on this sphere. We assume a viewing angle inversely proportional to the jet-boosted Lorentz factor, $\phi \sim \Gamma^{-1}$. Assuming further a bulk Lorentz factor of $\Gamma \approx 10$, the correction factor for the blazar population becomes (Jacobsen 2015)

$$\Theta_{\text{CF}} = \frac{4\pi}{\Omega} = \frac{4\pi}{2\pi(1 - \cos(\phi))} \approx \frac{4\pi}{2\pi(\phi^2/2)} = 4\Gamma^2 = 400, \tag{6.18}$$

which agrees with estimates of a few hundred (e.g. Ajello et al. 2009). In other words, for each blazar observed, we miss ∼400.

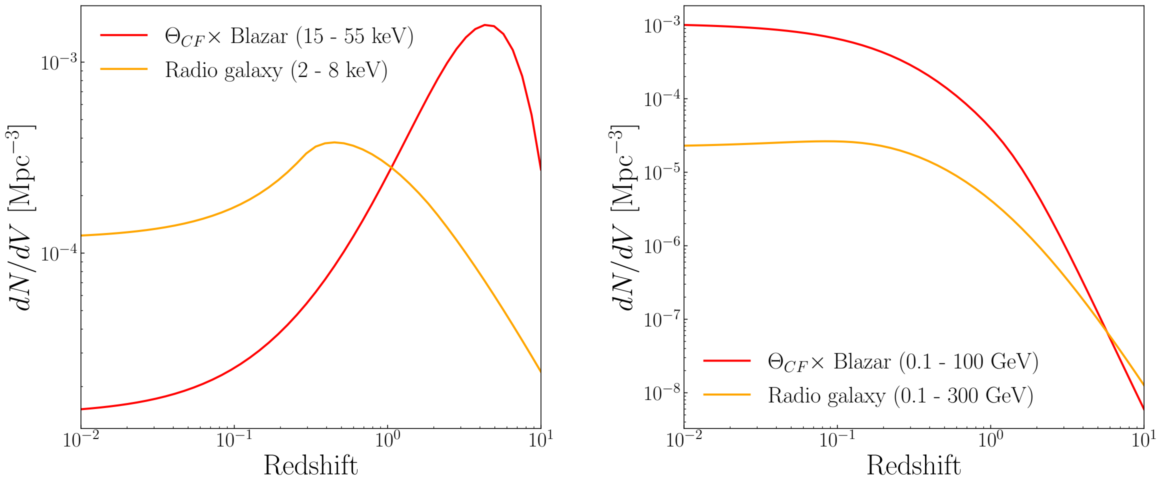

Figure 6.9: Comparison of number density evolution of X-ray (left) and gamma-ray (right) blazars and radio galaxies. The blazar models have been multiplied by the correction factor of Equation (6.18). *Left:* The radio galaxy population is the 2 - 8 keV LDDE model. *Right:* The blazar population is the 0.1 - 100 GeV LDDE model.

Figure 6.9 shows the effect of this correction factor on the X-ray and gamma-ray blazar population compared to the radio galaxies. The X-ray (left) population remains a decade less numerous at low redshift. However, in earlier epochs, it overtakes the radio galaxy model and becomes more numerous after $z \sim 1$. The gamma-ray (right) blazars now outnumber the radio galaxy parent population.

For the X-ray case, a correction factor of $\Theta_{\mathrm{CF}} = 400$ is insufficient to unify the observed blazar and radio galaxy population. For gamma-ray-detected populations, the same correction factor overestimates the number of blazar sources compared to their parent radio galaxies. This disagreement could be explained by an observation bias introduced by the strong beaming effects present in blazars. The SED of radio galaxies is double-peaked, and when observing in X-rays, we catch the part of the SED that is rising in the second peak. For blazars, the relativistic beaming moves the entire SED about a decade to higher energies and increases the energy flux by 3-4 orders. Thus, the trough between the two peaks is moved into the observed 15 - 195 keV X-ray range for the blazars, reducing their luminosity and we miss a large amount of the population. For the gamma-ray-selected sources, the situation is more ambiguous, as there is still the uncertainty of the lower luminosity limit. However, the same argument can be applied, as in gamma rays the majority of the radio galaxies may be sampled on the decrease from the high-energy peak. If the population instead would be beamed towards us, the same gamma-ray surveys would catch these sources at the peak of the high-energy bump.

CHAPTER

SEVEN

HIGH REDSHIFT BLAZAR EMISSION

Powerful blazars are of particular interest for neutrino production (see e.g. Oikonomou 2022). In this chapter, we present the results of applying our single-zone emission model to a couple of high redshift blazars. The blazars are PKS 0537-286 and PKS 0836+710 (also known as 4C 71.07). These sources have already been modelled by Ghisellini et al. (2010) and were chosen as they favour the emission region to lie within the BLR. This would make them strong emitters of all high-energy messengers. In Section 7.1 we present the SED found from our single-zone model using agnpy (Nigro et al. 2022) with the parameters of Ghisellini et al. (2010), whilst in Section 7.2 we instead perform a fit to the photometric data of our blazars to achieve greater agreement with observations. Finally, in Section 7.3 we apply the methodology introduced in Chapter 4 to estimate the total neutrino production of our blazars.

We note that due to time constraints, the results presented in this chapter are not fully satisfactory and a thorough discussion is partly omitted.

7.1 Spectral energy distribution

To construct the full SED of the two blazars, we need to take into consideration all the different regions of the AGN. This includes the thermal emission from the accretion disk and dust torus, as well as the synchrotron radiation, synchrotron self-Compton and external Compton emission from the jet blob.

7.1.1 Flux from the accretion disk and dust torus

The blackbody radiation from the accretion disk is found by inserting the blackbody intensity from Equation (4.3) into the energy flux of Equation (3.6) and reads

$$\nu_{\rm obs} F^{\rm SS}_{\nu_{\rm obs}} = \frac{4\pi}{d_{\rm L}^2} \frac{\mu_{\rm s} \nu_{\rm obs}^4 h}{c^2} \int_{R_{\rm in}}^{R_{\rm out}} dR \, \frac{R}{\exp[h\nu_{\rm obs}/k_{\rm B} T^{\rm SS}(R)] - 1}, \tag{7.1}$$

with the temperature profile $T^{\rm SS}(R)$ given by Equation (3.4).

Similarly, we find the final expression for the thermal radiation from the dust torus by inserting Equation (4.3) into Equation (4.1). This yields the final expression

$$\nu_{\mathrm{obs}} F^{\mathrm{DT}}_{\nu_{\mathrm{obs}}} = \frac{2\pi h}{c^2} \frac{\nu_{\mathrm{obs}}^4 R_{\mathrm{DT}}^2}{d_{\mathrm{L}}^2} \frac{1}{\exp(h\nu_{\mathrm{obs}}/k_{\mathrm{B}} T^{\mathrm{DT}}) - 1}, \tag{7.2}$$

with the sublimation temperature $T^{\mathrm{DT}} = 1500$ K.

7.1.2 Flux from synchrotron emission

The observed energy flux from the synchrotron and additional synchrotron self-absorption processes within the jet blob is given by Equation (4.8) and Equation (4.12). We want to compare with the modelling done by Ghisellini et al. (2010), where they used a broken power law for the electron distribution. Thus, instead of using the log-parabola distribution of Equation (4.4), we use a broken power law of the form

$$\underline{n}'_{\mathrm{e}}(\gamma') = k \left[\left(\frac{\gamma'}{\gamma'_b}\right)^{-s_1} H(\gamma'; \gamma'_{\mathrm{min}}, \gamma'_{\mathrm{b}}) + \left(\frac{\gamma'}{\gamma'_b}\right)^{-s_2} H(\gamma'; \gamma'_{\mathrm{b}}, \gamma'_{\mathrm{max}}) \right], \tag{7.3}$$

where once again H is the Heaviside function. This expression differs slightly from the one used by Ghisellini et al. (2010) (equation 2 therein), but this difference is not noticeable in the SED. With this particle distribution, we also calculate the synchrotron self-Compton radiation using Equation (4.15).

7.1.3 Flux from external Compton processes

For external Compton processes, we consider the radiation fields discussed in Chapter 3. In combination with Equation (4.20), we calculate the observed external Compton energy flux as

$$\nu_{\mathrm{obs}} F^{\mathrm{EC,SS}}_{\nu_{\mathrm{obs}}} = \frac{3^2}{2^9 \pi^3} \frac{\sigma_{\mathrm{T}} G M \dot{m}}{d_{\mathrm{L}}^2 r^3} \epsilon_s^2 \delta_D^3 \int_0^{2\pi} d\phi \int_{\mu_{\mathrm{min}}}^{\mu_{\mathrm{max}}} d\mu \frac{\varphi(\mu; r)}{\epsilon_0^2(\mu; r)(\mu^{-2} - 1)^{3/2}} \int_{\gamma_{\mathrm{low}}}^{\infty} d\gamma \frac{\underline{N}'_{\mathrm{e}}(\gamma/\delta_{\mathrm{D}})}{\gamma^2} \Xi_{\mathrm{C}} \tag{7.4}$$

form the accretion disk,

$$\nu_{\mathrm{obs}} F^{\mathrm{EC,BLR}}_{\nu_{\mathrm{obs}}} = \frac{3}{2^9 \pi^3} \frac{\sigma_{\mathrm{T}} \xi_{\mathrm{BLR}} L_{\mathrm{disk}}}{d_{\mathrm{L}}^2} \left(\frac{\epsilon_{\mathrm{s}}}{\epsilon_{\mathrm{BLR}}}\right)^2 \delta_{\mathrm{D}}^3 \int_0^{2\pi} d\phi \int_{-1}^{1} \frac{d\mu_{\mathrm{s}}}{x^2} \int_{\gamma_{\mathrm{low}}}^{\infty} d\gamma \frac{\underline{N}'_{\mathrm{e}}(\gamma/\delta_{\mathrm{D}})}{\gamma^2} \Xi_{\mathrm{C}} \tag{7.5}$$

from the BLR and

$$\nu_{\mathrm{obs}} F^{\mathrm{EC,DT}}_{\nu_{\mathrm{obs}}} = \frac{3}{2^8 \pi^3} \frac{\sigma_{\mathrm{T}} \xi_{\mathrm{DT}} L_{\mathrm{disk}}}{d_{\mathrm{L}} x^2} \left(\frac{\epsilon_{\mathrm{s}}}{\epsilon_{\mathrm{DT}}}\right)^2 \delta_{\mathrm{D}}^3 \int_0^{2\pi} d\phi \int_{\gamma_{\mathrm{low}}}^{\infty} d\gamma \frac{\underline{N}'_{\mathrm{e}}(\gamma/\delta_{\mathrm{D}})}{\gamma^2} \Xi_{\mathrm{C}} \tag{7.6}$$

from the dust torus. Out of these, the external Compton from the BLR radiation field dominates for both blazars. The X-ray corona accompanying the accretion disk is not taken into consideration, as it is not yet implemented in agnpy. Even if taken into consideration, its contribution would not significantly alter the shape of the SED.

Blazar	z	r^{a}	$M_{\mathrm{BH}}^{\mathrm{b}}$	$R_{\mathrm{BLR}}^{\mathrm{c}}$	$\log P_{\mathrm{e}}^{\mathrm{d}}$	$L_{\mathrm{disk}}^{\mathrm{e}}$	B	Γ	γ_0	γ_{max}	s_1	s_2
PKS 0537-286	3.104	420	2e9	735	45.52	54	1.92	15	50	2e3	-1	3
PKS 0836+710	2.172	540	3e9	1.5e3	45.54	225	3.28	14	90	2e3	-1	3.6

Table 7.1: Parameters used to construct the SED of the two considered blazars. [a]Distance to emitting blob in units of 10^{15} cm. [b]Mass of the black hole in solar masses. [c]Distance to (radius of) the BLR in units of 10^{15} cm. [d]Logarithm of the power injected into the jet for electrons with P_{e} in units of erg/s. [e]Accretion disk luminosity in 10^{45} erg/s.

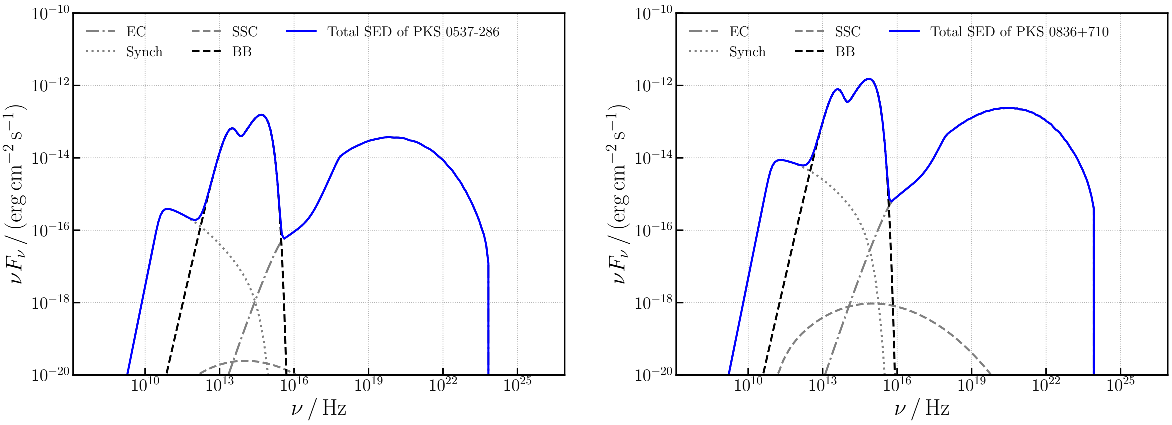

Figure 7.1: SED of PKS 0537-286 (left) and PKS 0836+710 (right). The parameters used are listed in Table 7.1.

Using the parameters listed in Table 7.1, the full SED of both blazars is shown in Figure 7.1. Compared to the model of Ghisellini et al. (2010), we see that our SEDs disagree significantly. Thus, even though Ghisellini et al. (2010) also uses a simple single-zone model, the difference between the models is substantial and our model requires a change in the parameterization. Details on the model used by Ghisellini et al. (2010) are found in Ghisellini & Tavecchio, 2009. In light of this mismatch, we need to determine the parameters of our model from observational data.

7.2 Data fit

To calculate a SED that more accurately describes the two blazars using our single-zone model, we use the parameters of Table 7.1 as initial parameters to perform a fit to observations. For both PKS 0357-286 and PKS 0836+710, we use the publicly available NASA/IPAC Extragalactic Database[1] to acquire photometric data points across the full SED. Varying only the parameters listed in Table 7.2, the fit is performed using *gammapy* (Deil et al. (2017)) with *iminuit* as a backend, a Python interface for the C library Minuit (James & Roos, 1975).

The results of performing this fit are shown in Figure 7.2. The large error bars along the energy axis are an unwanted artefact of the modelling software with no intuitive way of being removed. They should therefore be ignored when examining the SEDs. The data

---

[1] `https://ned.ipac.caltech.edu/`

Blazar	k^{a}	δ_{D}	B	p^{b}	q^{b}	$L_{\mathrm{disk}}^{\mathrm{c}}$
PKS 0537-286	1.29	20	1.32	2.41	0.56	150
PKS 0836+710	0.10	17.47	0.23	2.47	0.001	225

Table 7.2: Parameters modified by the fitting procedure described in the text. [a]Electron distribution normalization factor in units of cm^{-3}. [b]The spectral indices p and q determine the behaviour of the log-parabolic distribution of Equation (4.4). [c]Accretion disk luminosity is in Table 7.1. Disk luminosity is not a fit parameter, but is modified for PKS 0537-286 (see text).

points below 10^{-2} eV are not considered in the fit, as this region is likely dominated by synchrotron radiation in the large, extended jet, i.e. significantly further out than the blob. Including this region in the fit would therefore worsen it at higher energies. From the fitting procedure, we found that the log-parabolic electron distribution introduced in Chapter 4 describes the observed SED better than the previously assumed broken power law. To better fit the thermal spectrum of the accretion disk and the dust torus for PKS 0537-286, the luminosity of the accretion disk was increased from 54×10^{45} erg/s to 150×10^{45} erg/s. An alternative would have been to instead increase the accretion efficiency η, which would also improve the accretion disk fit of PKS 0836+710. However, to stay consistent with our assumption of a Schwarzschild black hole, we keep $\eta \simeq 1/12$.

The only parameters varied in the fit were the spectral indices of the electron distribution p and q, the normalization constant k, the magnetic field B and the doppler factor δ_{D}. The initial parameters, listed in Table 7.1, were sufficient enough to perform the 5-parameter fit within a reasonable time, without requiring extensive computational resources. Allowing more parameters to vary would ultimately give a better fit but at a much greater computational cost.

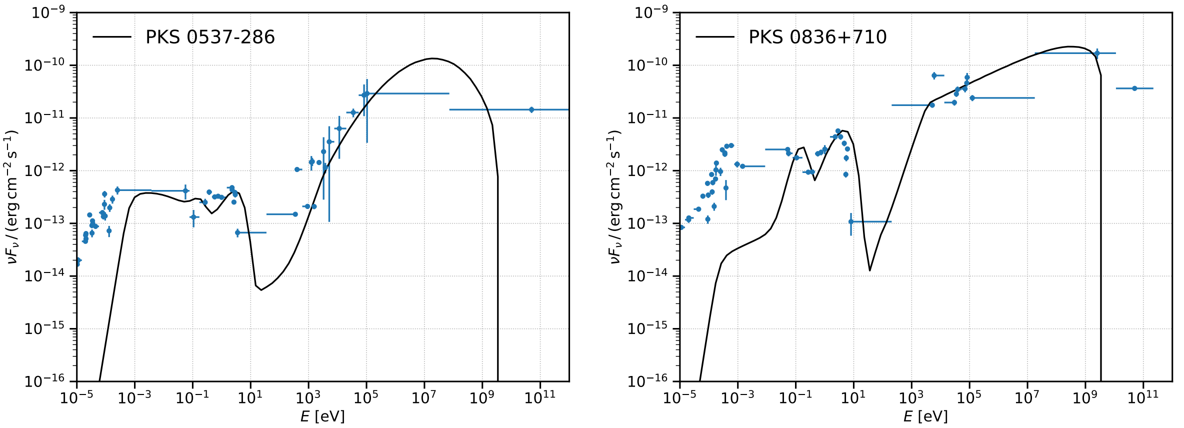

Figure 7.2: SED after performing the fit to observational data for PKS0537-286 (left) and PKS0836+710 (right). The large errorbars along the energy axis is an unwanted artefact of the fitting software and should be ignored.

7.3 Neutrino production

In the previous sections of this chapter, we have considered a pure electron distribution travelling down the jet, entering our blob and producing non-thermal radiation. For neutrinos to be produced in purely leptonic interactions, the conditions need to be right for the subsequent gamma rays to produce muon-antimuon pairs. This is not thought to be realizable in most astrophysical environments, and thus we instead introduce a population of protons into our emitting zone.

To achieve this, we assume an equal amount of protons and electrons. The protons population is then injected following the same log-parabola distribution of the electrons, namely

$$f_{\mathrm{p}}(E_{\mathrm{p}}) = n_{\mathrm{p}}(E) = k\left(\frac{E_{\mathrm{p}}}{E_0}\right)^{-[p+q\log(E_{\mathrm{p}}/E_0)]}, \tag{7.7}$$

parameterized instead by the proton energy $E_{\mathrm{p}} = \gamma_{\mathrm{p}} m_{\mathrm{p}} c^2$. As we changed from considering the distribution in Lorentz factors to instead the particle energy, the normalization constant now has dimensions $\mathrm{eV}^{-1}\ \mathrm{cm}^{-3}$.

For the spectral energy density of the photon field, we first estimate the energy density from the accretion disk, BLR and dust torus photon field at the blob position as described in Chapter 3. For both PKS 0537-286 and PKS 0836+710, the BLR photon field dominates and thus we consider only this field. This energy density is given by Equation (3.19) and equals 6.8 $\mathrm{erg/cm^3}$ for PKS 0537-286 and 2.04 $\mathrm{erg/cm^3}$ for PKS 0836+710. In what follows, we will consider only PKS 0537-286, but the procedure is the same for other sources.

To apply this energy density to Equation (4.48) and estimate the subsequent neutrinos, we first make one last simplification. Instead of using the energy density just calculated, we will consider the target photon field to be a diluted blackbody (also known as a greybody). This is done by considering the Lyman alpha line emission of a general BLR to be a blackbody at energy $E_{\mathrm{L}\alpha} = 10.2$ eV. As a consequence of Wien's displacement law, this corresponds to a blackbody with a peak frequency at $T_{\mathrm{L}\alpha} = E_{\mathrm{L}\alpha}/(2.8k_{\mathrm{B}})$, where k_{B} is the Boltzmann constant. Inserting this temperature into Equation (4.1), we find the expected blackbody energy density as

$$u_{\mathrm{ph}} = 24161.62\ \mathrm{erg/cm^3}. \tag{7.8}$$

The final step is to normalize this according to the energy density of our model. This is done by dividing with the energy density found from Equation (3.19) and equals

$$A_{\mathrm{norm}} = \frac{24161.26\ \mathrm{erg/cm^3}}{6.8\ \mathrm{erg/cm^3}} \simeq 3553. \tag{7.9}$$

With this normalization, we calculate the final diluted blackbody spectral energy density as

$$f_{\mathrm{ph}}(\epsilon_{\mathrm{ph}}) = \frac{1}{A_{\mathrm{norm}}}\frac{\epsilon_{\mathrm{ph}}^2}{2\pi^2 c^3 \hbar^3}\frac{1}{\exp(\epsilon_{\mathrm{ph}}/k_{\mathrm{B}}T_{\mathrm{L}\alpha}) - 1}, \tag{7.10}$$

where ϵ_{ph} is the energy of the target photon.

Inserting these proton and photon distributions into Equation (4.48), the resulting production spectra of photons and different leptons from PKS 0537-286 are shown in Figure 7.3 and Figure 7.4. We note that the normalization procedure of the photon field considered in Kelner & Anaronian (2008) is unclear, and thus, to calibrate the normalization in line with their work, we multiply with an additional factor between 40–80 depending on the final particles and energies.

Figure 7.3 and Figure 7.4 shows the resulting production spectra of photons and leptons. For the lowest $E_0 = 10^{17}$ eV break energy, the numerical integration procedure has encountered problems and the illustrated electron and electron anti-neutrino spectra are not accurate. For the three other cases ($E_0 = 10^{18}$ eV, $E_0 = 10^{19}$ eV and $E_0 = 10^{21}$ eV), the spectra are representative of the model predictions. We see that for all different values of E_0, the photon production surpasses the electron production, especially at higher energies. For the neutrinos, all but the electron anti-neutrino are produced at similar rates, except for at the highest cutoff energy, where the electron anti-neutrino is produced at a similar rate to the others. As the production of both electrons and electron anti-neutrinos require an anti-muon, which subsequently requires an π^--meson only produced when the interactions produce two or more muons, we would expect the production of these particles to be lower than the others. At higher energies, however, the majority of protons are energetic enough to produce multiple pions at each interaction, and the production rate of electrons and electron anti-neutrinos resembles the other leptons.

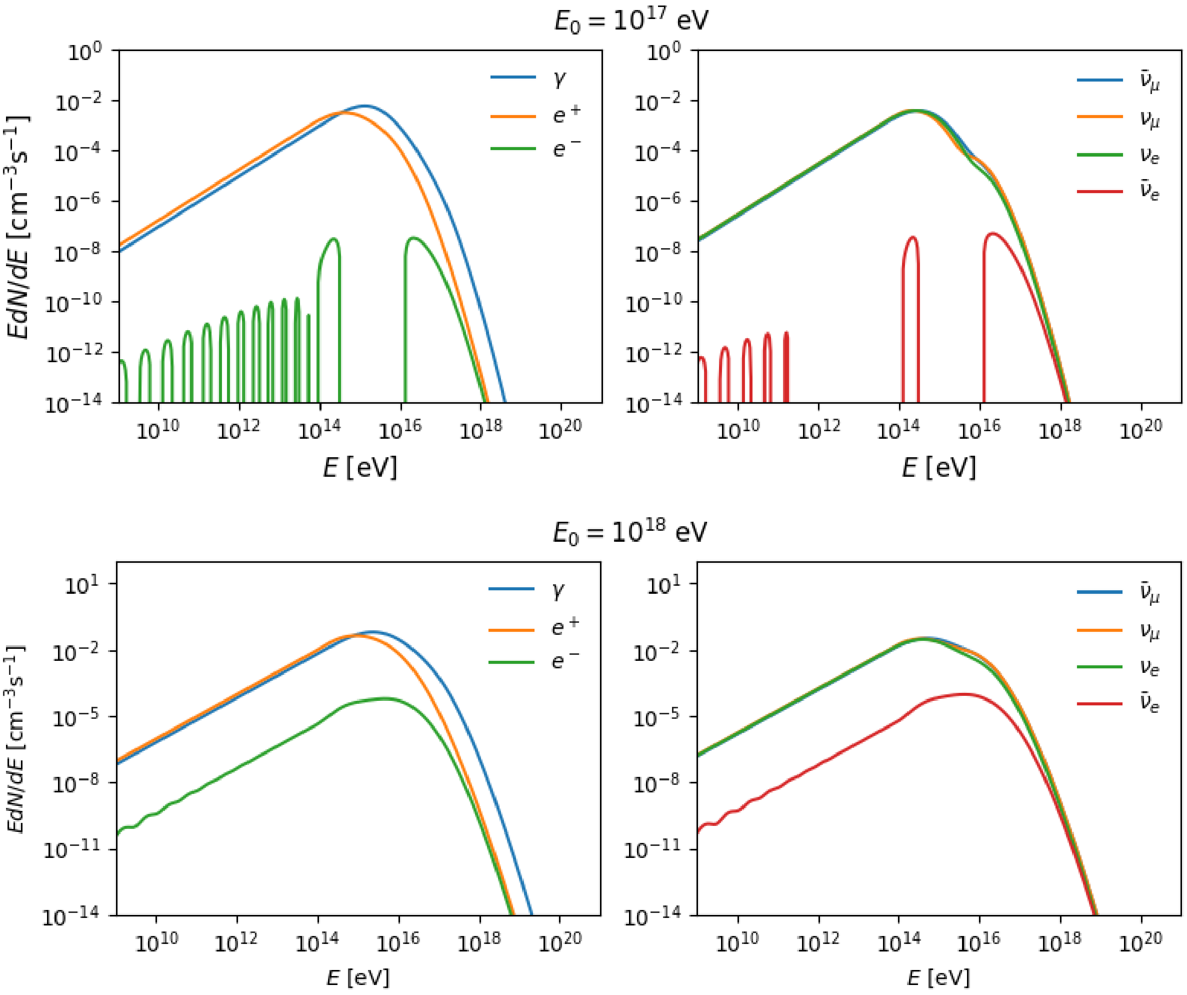

Figure 7.3: Production spectra of electrons and photons (left) and neutrinos (right) from PKS 0537-286. E_0 is the cutoff energy in the log-parabola proton distribution.

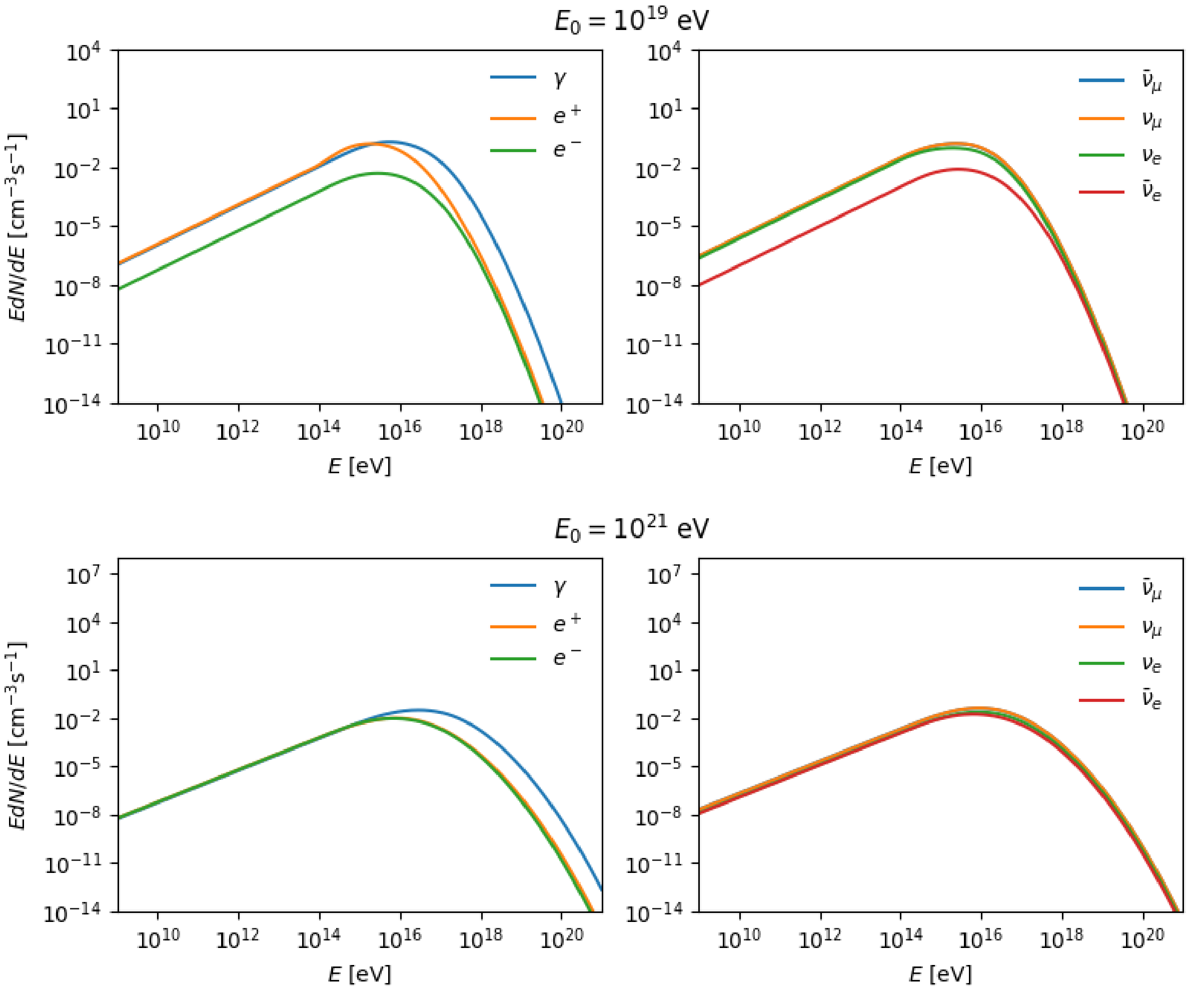

Figure 7.4: The same as for Figure 7.3 but for different values of E_0.

Now that we know the production rate of neutrinos for our blazars, we can additionally estimate the expected flux of these neutrinos on Earth. For this, we multiply by the volume of the blob to find the total number of neutrinos produced per second. Subsequently, we find the total neutrino energy flux on Earth as

$$E_{\rm obs}\frac{dN}{dE_{\rm obs}} = E\frac{dN}{dE} \times \frac{V_{\rm blob}}{4\pi d_{\rm L}^2}, \tag{7.11}$$

where $d_{\rm L}$ is the luminosity distance and the energy changes as $E_{\rm obs} = E/(1+z)$.

The resulting local flux for both PKS 0537-286 and PKS 0836+710 is shown in Figure 7.5. The figures show the summed contribution from all neutrinos of Figure 7.3 and Figure 7.4 for four different cutoffs in proton energy. For both sources, the total energy flux increases with increasing E_0. This behaviour is stronger for PKS 0836+710. The spectrum of PKS 0537-286 additionally moves towards higher energies for the increased cutoff. The neutrino energy flux from PKS 0836+710 is greater at higher cutoff energies than for the PKS 0537-286 case. In Aartsen et al. (2018), the authors note a predicted $\nu_\mu + \bar{\nu}_\mu$ energy flux of 1.8×10^{-10}erg/cm^2/s $= 1.12 \times 10^{-7}$GeV/cm^2/s for the flaring blazar TXS 0506+056 incident with the IceCube-170922A neutrino alert. When compared to our predicted neutrino flux, we see a relatively close match for neutrinos of energies $\sim 10^{12} - 10^{13}$ eV for PKS 0537-286, and for PKS 0836+710 excluding the most energetic proton distribution case. In the case of PKS 0537-286 however, our model predicts a significantly larger neutrino flux at higher energies.

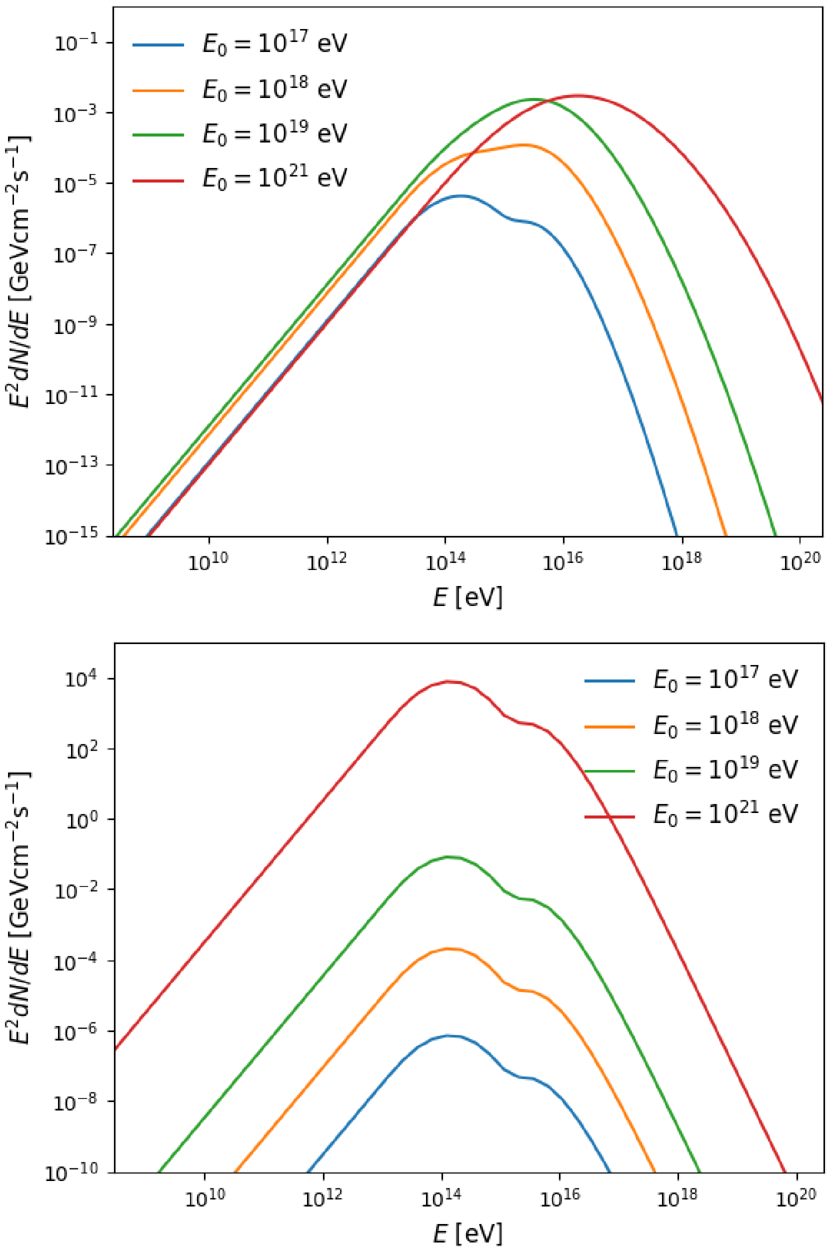

Figure 7.5: Predicted neutrino energy flux on Earth from PKS 0537-286 (upper) and PKS 0836+710 (lower).

Conclusion

When compared to estimates found from relevant literature, our single-zone emission model overproduces the neutrino energy flux. Whether this is caused mainly by inaccuracies within the model or by oversights in our approach cannot be fully settled, however, the limited time dedicated to this procedure strongly favours the latter. With this being said, we fully realize that the considered single-zone model is an unrealistic simplification and would likely fail to predict reasonable results despite greater efforts.

CHAPTER

EIGHT

TAKE-HOME MULTI-MESSAGES

8.1 Conclusion

Using luminosity functions, we have modelled different AGN populations. We found that the X-ray-selected blazar populations peak in luminosity around $10^{45} - 10^{46}$ erg/s. The X-ray-selected Seyfert and radio galaxy populations show a steady increase in their luminosity distribution at lower luminosities and thus the majority of these populations are expected to be found at lower ($< 10^{43}$ erg/s) luminosities. The gamma-ray-selected blazars, radio galaxies and RLF displayed the same behaviour as the X-ray radio galaxies and Seyferts.

The luminosity function models show that the number density of X-ray selected radio galaxies evolves positively with redshift until $z \sim 0.3$, before steepening at higher z. The evolving Seyfert model exhibits a continuous positive evolution with redshift. The number density of the X-ray selected general blazar and FSRQ populations were all found to evolve positively with redshift until $z \sim 3 - 4$. The BL Lac model was the only X-ray population with a negative evolution at all redshifts. The gamma-ray selected populations of radio galaxies, blazars and BL Lacs display a continuous negative evolution in number density with increasing redshift. The gamma-ray FSRQ population evolved positively until $z \sim 0.6 - 0.7$, and negatively afterwards. The 151 MHz RLF describing the behaviour of radio galaxies shows a positive number density evolution for $z \lesssim 0.7$ and turns constant for larger z.

The characteristic luminosity peaked at high redshift ($z \sim 3 - 4$) for all X-ray selected radio galaxy models, the 151 MHz radio galaxy model, gamma-ray FSRQ model and the general X-ray blazar and FSRQ populations. The X-ray BL Lac model, the non-evolving Seyfert model and the 0.1-300 GeV gamma-ray radio galaxy model exhibit a constant characteristic luminosity. The characteristic luminosity for the gamma-ray BL Lac population shows a negative evolution with increasing redshift. The 0.1-100 GeV gamma-ray radio galaxy population and the X-ray evolving Seyfert population display an increase in characteristic luminosity until $z > 10$.

Assuming that the AGN populations have the same emissivity in UHECRs as in radio, X-ray or gamma-rays, only the X-ray selected FSRQ population fails to produce ($< 0.1\%$) a significant amount of the local flux of UHECRs. The 151 MHz (0.1 - 300 GeV) radio galaxy population could produce $2 - 3\%$ ($30 - 40\%$) of the local UHECRs. All other models showed local production of UHECRs $> 100\%$, and thus we conclude that their UHECR emissivity must be lower than for X-rays and gamma-rays.

We compared the emissivity of our population models to the diffuse neutrino flux predicted and found that all AGN populations except the 15-55 keV selected FSRQs and 151 MHz selected radio galaxies would produce more neutrinos than observed if their neutrino emissivity is comparable to that of X-rays and gamma-rays. We conclude that the high-energy neutrino emissivity of AGN must be far less than X-rays and gamma-rays, which favours a more leptonic process. Finally, we discussed the unification of blazars and radio galaxies in light of geometry and beaming effects.

For the second part of this thesis, we applied a single-zone model for the emission from high-redshift blazars. The non-thermal emission from the jet blob consists of the synchrotron, synchrotron self-absorption, synchrotron self-Compton and external Compton radiation. Using a pure electron distribution we fit the SED of our model to observations within reasonable limits. By considering an equivalent distribution of protons, we predicted the secondary neutrinos produced through proton-photon interactions and conclude that the model overestimates the neutrino production at high energies.

8.2 Future outlook

To build a more complete understanding of AGN and other energetic astrophysical objects, the detection of high-energy, non-thermal photons, cosmic rays and neutrinos will be of great importance. With upgrades of equipment in our best observatories like Pierre Auger and IceCube, in addition to continuously improving software and statistical methods used to analyse the data, multi-messenger astronomy and astrophysics are steadily moving forward. With plans in the works for next-generation neutrino detectors, like the KM3NeT observatory under construction in the Mediterranean Sea, or the RNO-G currently under construction in Greenland (J. Aguilar et al. 2021), the next few years will bring yet another leap forward for neutrino research. With increased statistics and new observatories, the uncertainties around the diffuse neutrino flux and its connection to the local flux of cosmic rays might be put to rest. Future high-energy telescopes, like the Cherenkov Telescope Array (Actis et al. 2011), will survey the sky in gamma rays up to 300 TeV, probing photon energies that have never previously been explored.

This work has focused on the importance of considering objects like AGN across all messengers. By simultaneously studying non-thermal photons, UHECRs and high-energy neutrinos, stronger constraints on mechanisms driving AGN can be unveiled. Further studies into luminosity functions for different high-energy objects, like neutron stars or GRBs, and comparing them to the local flux of UHECRs and the diffuse neutrino flux would be an interesting undertaking. It will also be interesting to construct possible neutrino luminosity functions and to study how these change over different cosmic epochs. This will enable us to construct a more complete view of the contents of the Universe and how the epoch of structure formation proceeded.

APPENDIX

A

COORDINATE TRANSFORMATIONS

A.1 Coordinate transforms

We list in Table A.1 the most useful relativistic transformations between the reference frame at rest with respect to the black hole and host galaxy (unmarked), the reference frame comoving with the jet blob (primed) and the observer rest frame ("obs"). The relative velocity between the frames is β, and is connected to the doppler factor δ and the Lorentz factor Γ through

$$\delta = \frac{1}{\Gamma(1-\beta\cos\theta)}, \tag{A.1}$$

where θ is the relative angle between the reference frames.

Table A.1: Relativistic transformations between the host galaxy, blob comoving and observer rest frames.

Quantity	**Transformations**
Time	$t = t'/\delta$
Frequency	$\nu = \nu'\delta$
Energy	$\epsilon = \epsilon'\delta = \epsilon_{\rm obs}(1+z)$
Lorentz factor	$\gamma = \gamma'\delta$
Volume	$V = V'\delta$
Sine	$\sin\theta = \sin\theta'/\delta$
Cosine	$\cos\theta = (\cos\theta' + \beta)/(1+\beta\cos\theta')$
Total intensity	$I = I'\delta^4$
Specific intensity	$I(\nu) = I'(\nu')\delta^3$
Radiation energy density	$u = \Gamma^{-2}u'/(1+\beta+\beta^2/3)$
Energy flux	$\epsilon_{\rm obs}F_{\epsilon_{\rm obs}} = \delta^4\epsilon' F'_{\epsilon'}$

A.2 Covariant electrodynamics

A proper, covariant description of the dynamics of particles in electromagnetic fields requires a consideration of the force in four-vector form. The relevant four-vector takes the form

$$F^{\mu} = \frac{dp^{\mu}}{d\tau}, \tag{A.2}$$

where the 4-vector momentum $p^{\mu} = mu^{\mu} = m\gamma(c, \vec{v})$ and $d\tau = dt/\gamma$ is the proper time. The Lorentz force in manifestly covariant form is

$$\frac{dp^{\mu}}{d\tau} = \frac{Q}{mc} F^{\mu\nu} p_{\nu}. \tag{A.3}$$

Neglecting the electric permittivity and magnetic permeability, the field-strength tensor in Euclidean space is

$$F^{\mu\nu} = \begin{pmatrix} 0 & E^1 & E^2 & E^3 \\ -E^1 & 0 & -B^3 & -B^2 \\ -E^2 & -B^3 & 0 & B^1 \\ -E^3 & B^2 & -B^1 & 0 \end{pmatrix}. \tag{A.4}$$

By assuming zero electric field ($\vec{E} = 0$) and a uniform magnetic field, we set, without loss of generality, $\vec{B} = B\vec{z}$. Thus, the Lorentz force becomes

$$\frac{dp^{\mu}}{d\tau} = mc \begin{pmatrix} d\gamma/d\tau \\ d(\gamma\beta_x)/d\tau \\ d(\gamma\beta_x)/d\tau \\ d(\gamma\beta_z)/d\tau \end{pmatrix} = \frac{Q}{mc} F^{\mu\nu} p_{\nu} = QB \begin{pmatrix} 0 \\ \gamma\beta_y \\ -\gamma\beta_x \\ 0 \end{pmatrix}. \tag{A.5}$$

From this, the Lorentz force of Equation (4.6) is restored for $dt = \gamma d\tau$.

A.3 Whittaker functions

The Whittaker functions are solutions to the Whittaker equation

$$\frac{d^2 W_{\kappa,\lambda}(x)}{dz^2} + \left(-\frac{1}{4} + \frac{\kappa}{z} + \frac{1/4 - \lambda^2}{z^2} \right) W_{\kappa,\lambda}(x) = 0 \tag{A.6}$$

and are related to the confluent hypergeometric functions.

APPENDIX

B

SUPPLEMENTARY PLOTS

B.1 Luminosity distribution for varying redshift bins

As discussed in Chapter 6, we attach here the luminosity distribution of the AGN subpopulations for different redshift bins. For positively evolving sources, the more distant ones dominate, and vice-versa for a negative redshift evolution.

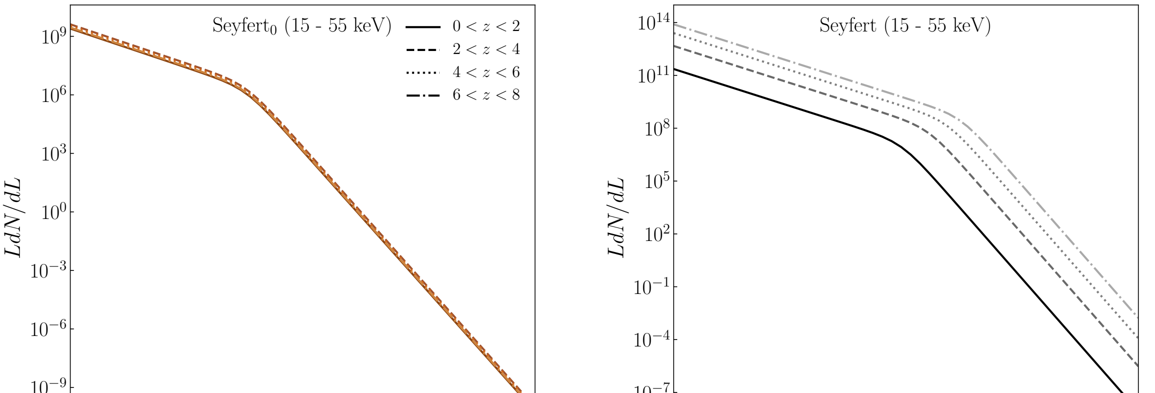

Figure B.1: Luminosity distribution of the non-evolving (left) and evolving (right) Seyfert populations for different bins in redshifts. The redshift bins are $0 < z < 2$ (solid line), $2 < z < 4$ (dashed line), $4 < z < 6$ (dotted line) and $6 < z < 8$ (dash-dotted line).

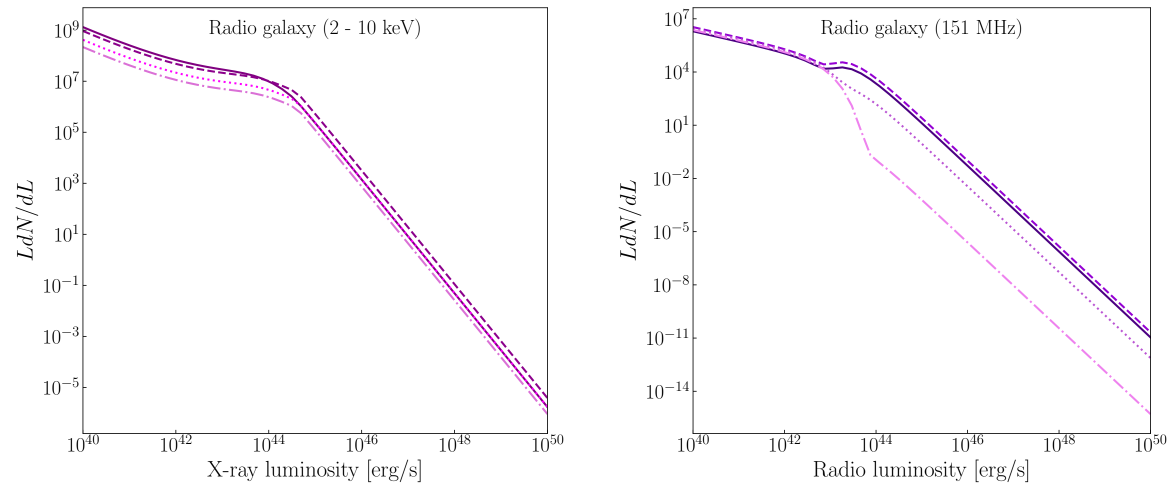

Figure B.2: The same as for Figure B.1 but for the 2 - 10 keV (left) and 151MHz (right) radio galaxy populations.

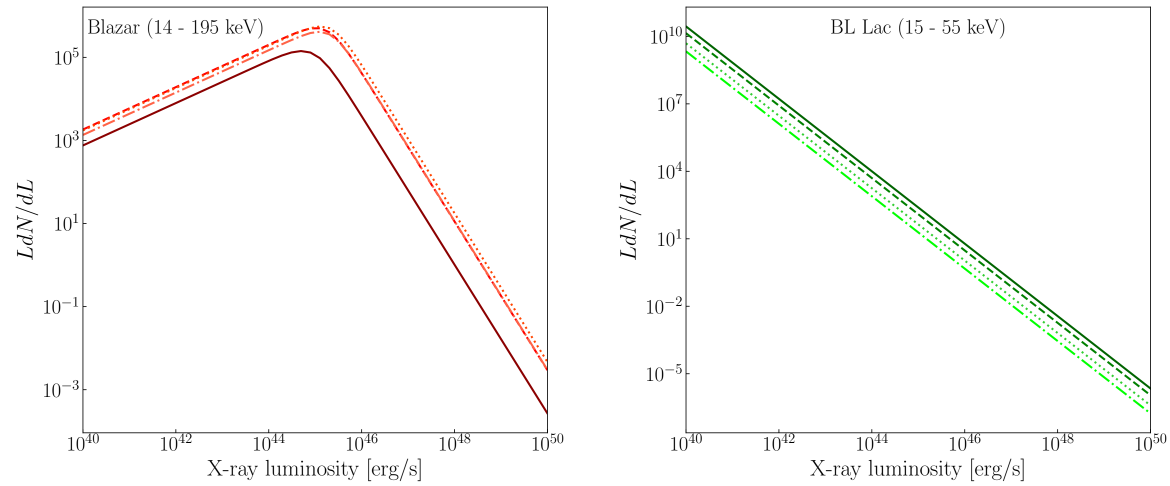

Figure B.3: The same as for Figure B.1 but for the 14–195 keV blazar (left) and 15–55 keV BL Lac (right) populations.

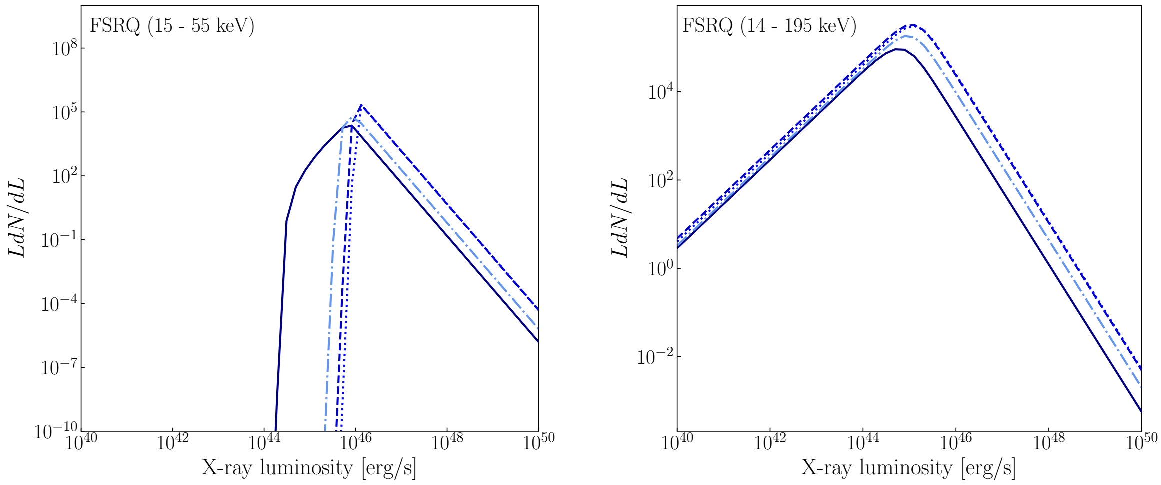

Figure B.4: The same as for Figure B.1 but for the 15–55 keV (left) and 14–195 keV (right) FSRQ populations.

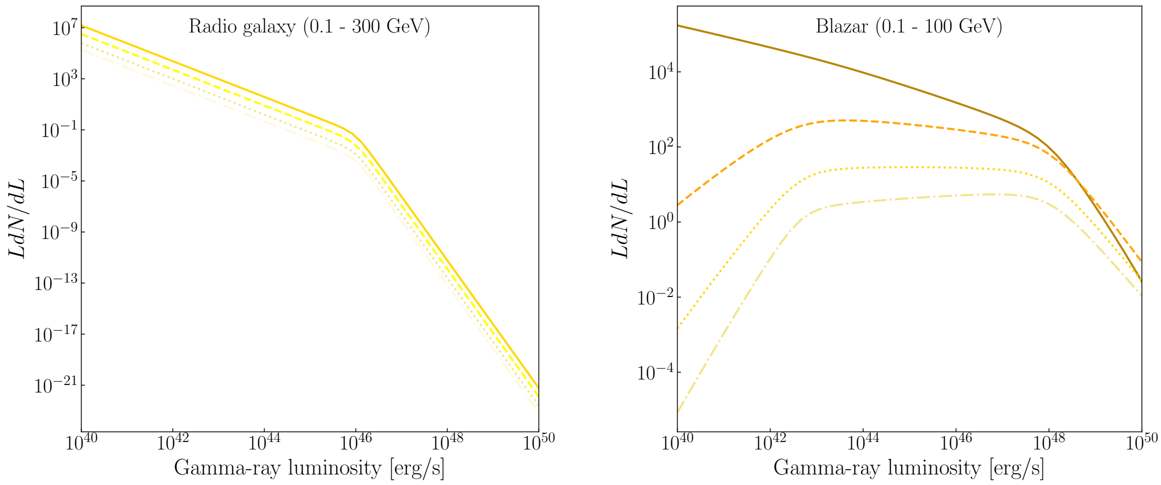

Figure B.5: The same as for Figure B.1 but for the 0.1–300 GeV radio galaxy (left) and 0.1–100 GeV blazar (right) populations.

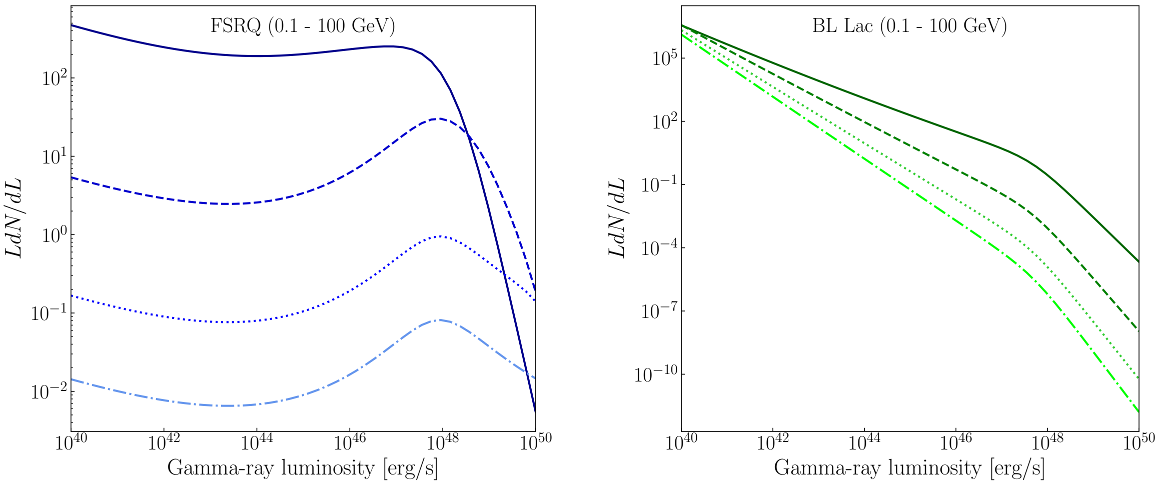

Figure B.6: The same as for Figure B.1 but for the 0.1–100 GeV FSRQ (left) and 0.1–100 GeV BL Lac (right) populations.

B.2 Cosmic ray emissivity at higher redshifts

In the main text, we considered only UHECRs emitted by sources located around $z = 0.01$ as the highest energy cosmic rays need to be produced in the local Universe. Despite this, UHECRs may originate from sources up to $z = 1$. Due to the slow evolution of the populations in the local ($z < 1$) Universe, the results do not change much between $z = 0.01$ and $z = 0.1$. For $z = 1$, there are some visible variations, but it is only for $z = 5$ that the evolution really changes the predicted UHECR emissivity. See the following plots for visualization.

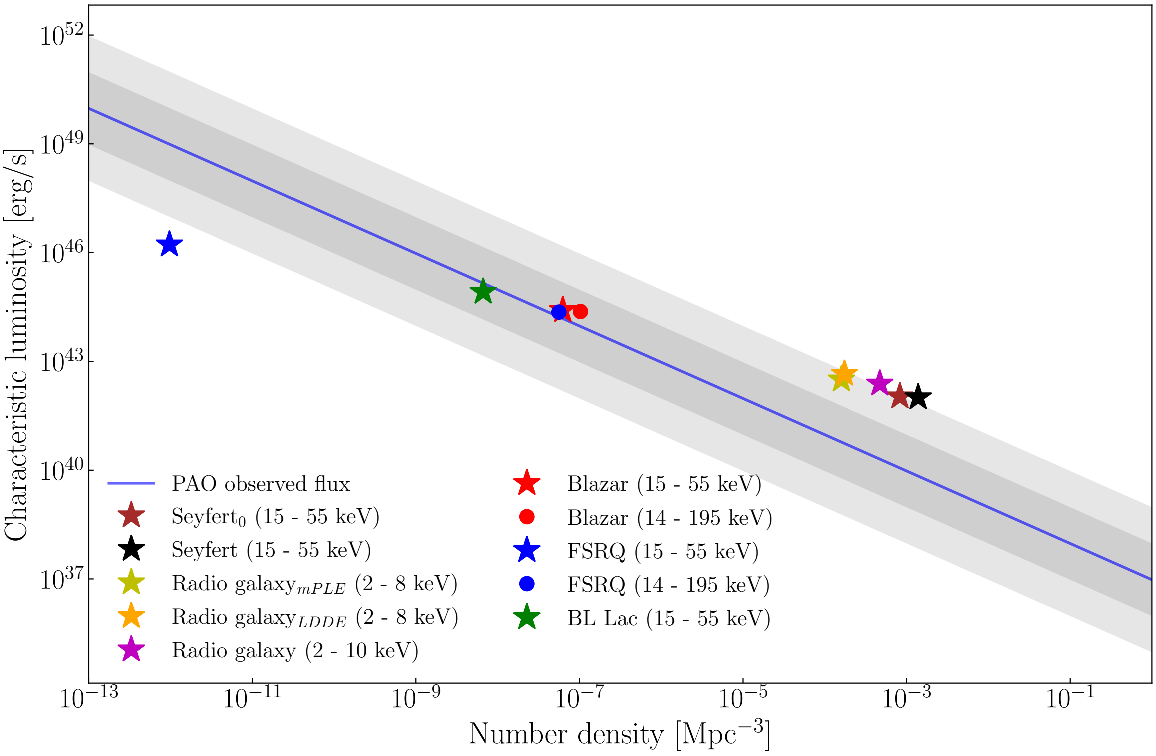

Figure B.7: Cosmic ray emissivity for all X-ray-detected populations at z=0.1

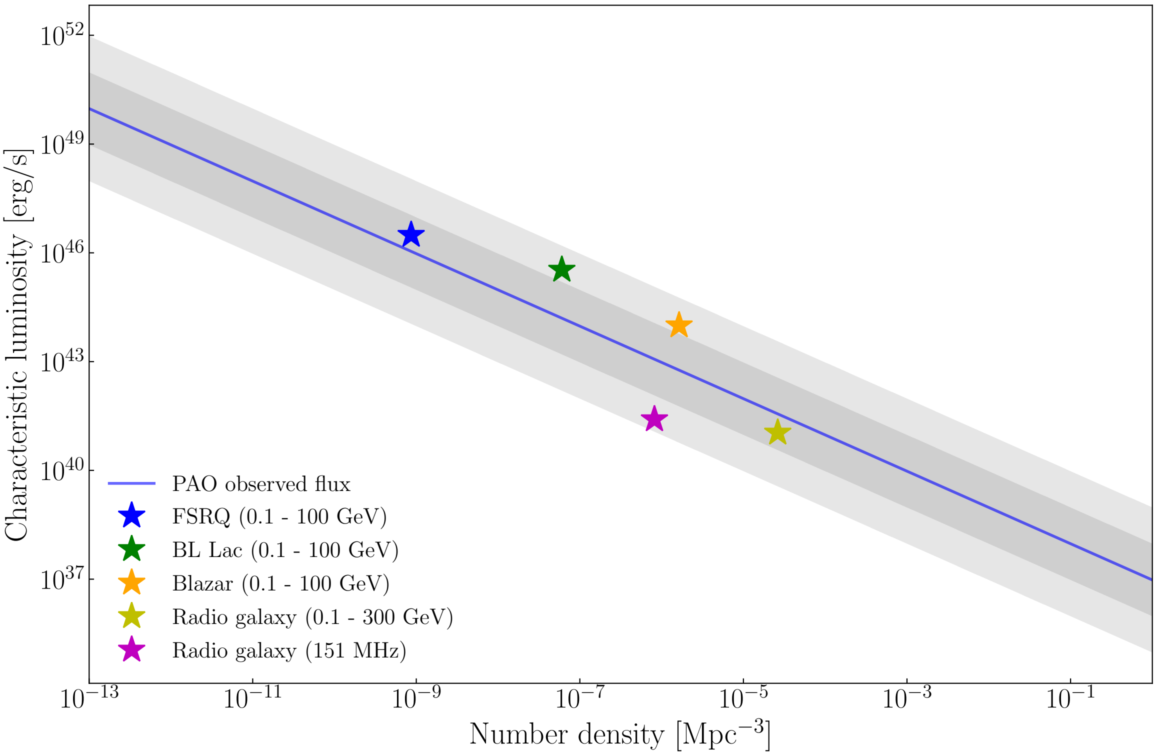

Figure B.8: Cosmic ray emissivity for radio and gamma-ray sources at z=0.1

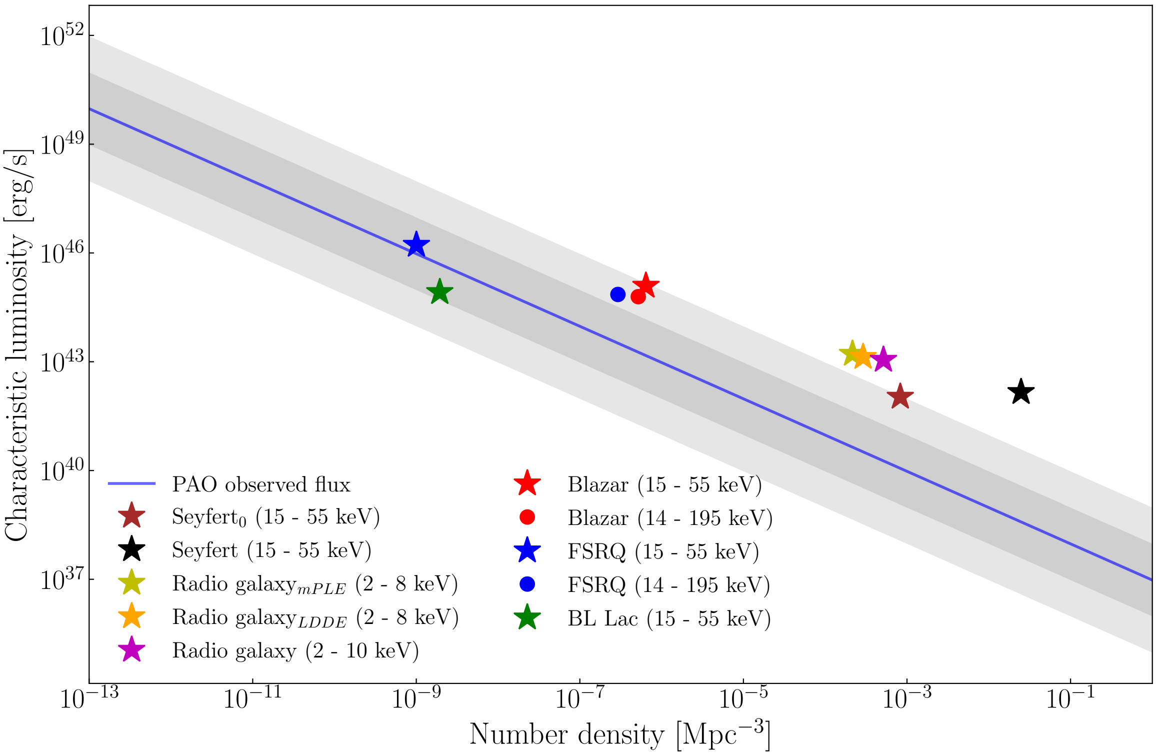

Figure B.9: Cosmic ray emissivity for all X-ray-detected populations at z=1

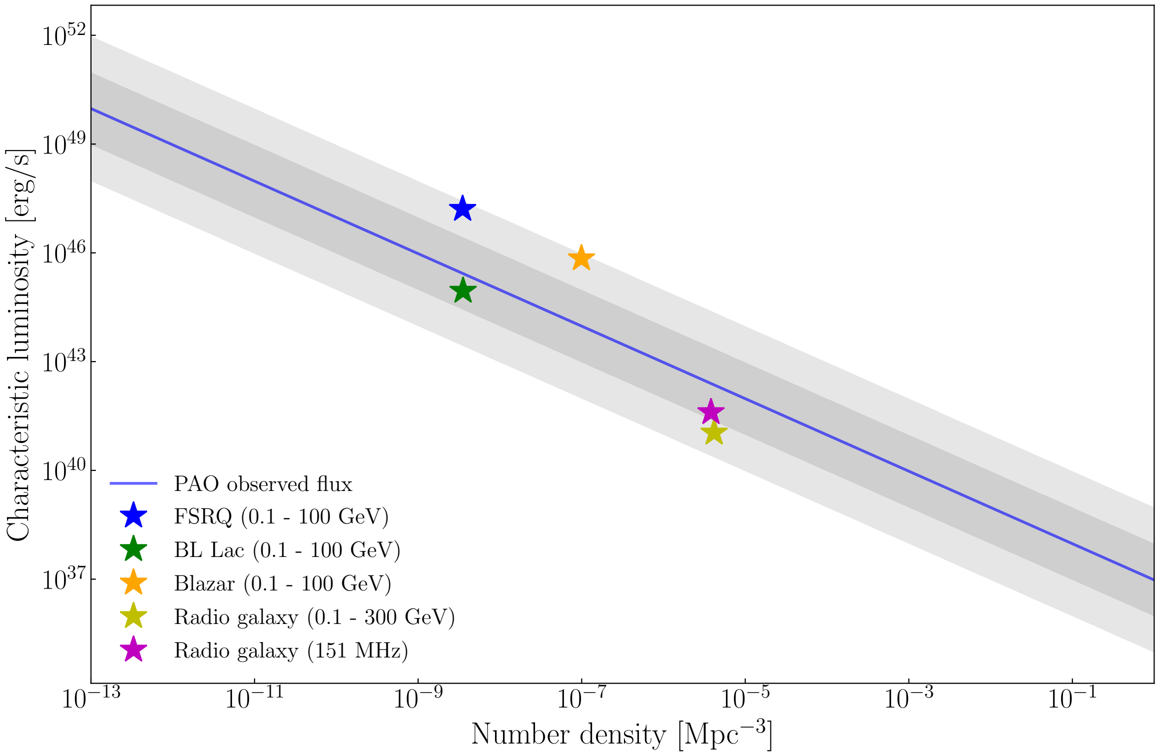

Figure B.10: Cosmic ray emissivity for radio and gamma-ray sources at z=1

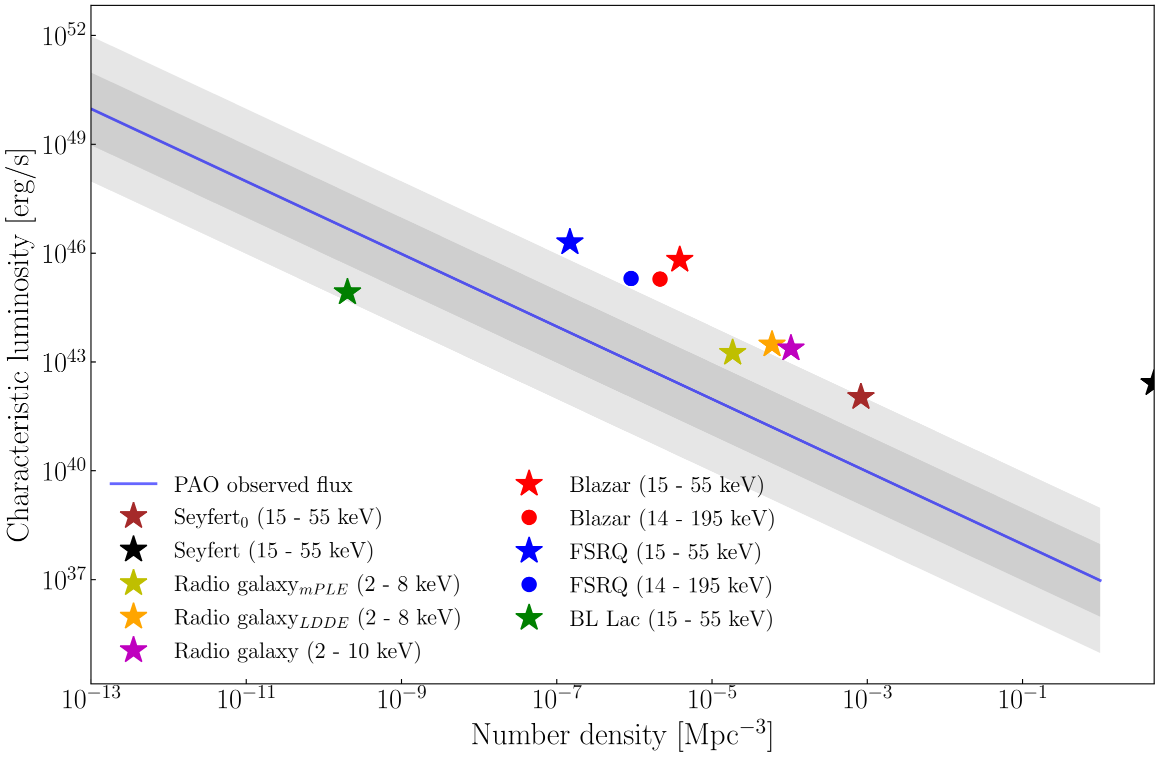

Figure B.11: Cosmic ray emissivity for all X-ray-detected populations at z=5

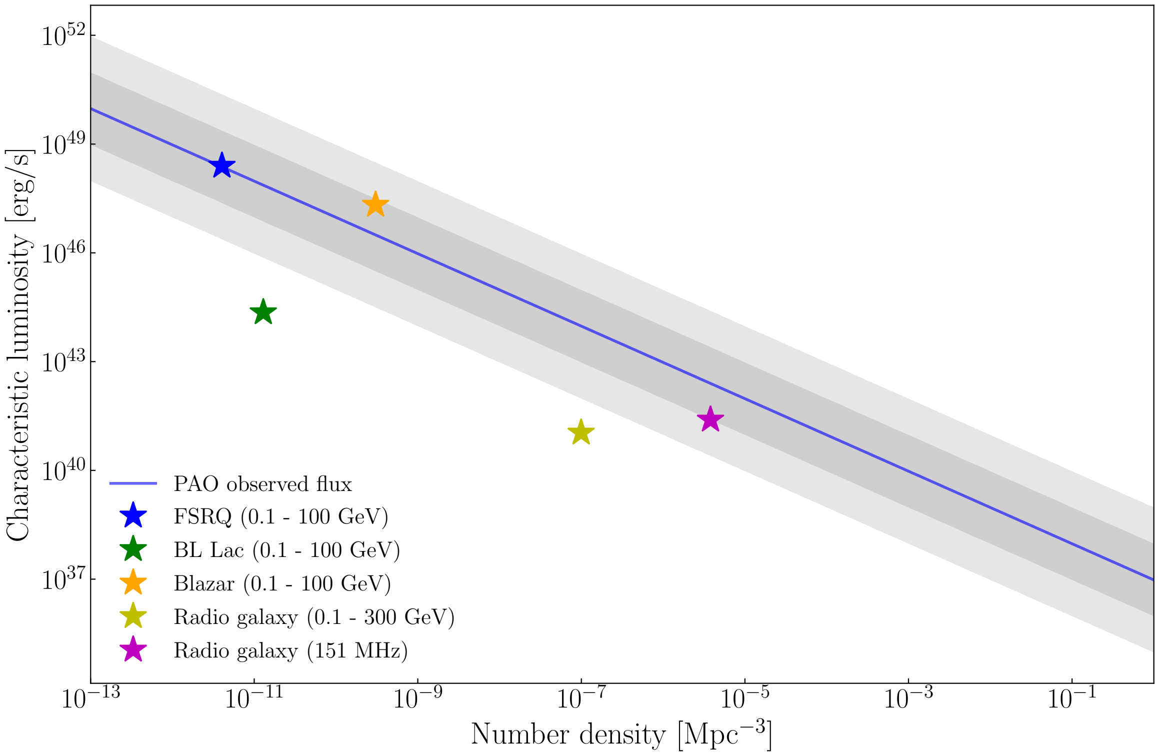

Figure B.12: Cosmic ray emissivity for radio and gamma-ray sources at z=5

BIBLIOGRAPHY

Aartsen, M. G., M. Ackermann, J. Adams, J. A. Aguilar, M. Ahlers, M. Ahrens, D. Altmann, et al. (May 2015). “SEARCH FOR PROMPT NEUTRINO EMISSION FROM GAMMA-RAY BURSTS WITH ICECUBE”. In: *The Astrophysical Journal Letters* 805.1, p. L5. DOI: `10.1088/2041-8205/805/1/L5`. URL: `https://dx.doi.org/10.1088/2041-8205/805/1/L5`.

Aartsen, M. G., M. Ackermann, J. Adams, J. A. Aguilar, M. Ahlers, M. Ahrens, I. Al Samarai, et al. (July 2017). “Extending the Search for Muon Neutrinos Coincident with Gamma-Ray Bursts in IceCube Data”. In: *The Astrophysical Journal* 843.2, p. 112. DOI: `10.3847/1538-4357/aa7569`. URL: `https://dx.doi.org/10.3847/1538-4357/aa7569`.

Abbasi, R. et al. (Mar. 2022). “Improved Characterization of the Astrophysical Muon–neutrino Flux with 9.5 Years of IceCube Data”. In: *The Astrophysical Journal* 928.1, p. 50. DOI: `10.3847/1538-4357/ac4d29`. URL: `https://dx.doi.org/10.3847/1538-4357/ac4d29`.

Abreu, P. et al. (Aug. 2022). “Arrival Directions of Cosmic Rays above 32 EeV from Phase One of the Pierre Auger Observatory”. In: *The Astrophysical Journal* 935.2, p. 170. DOI: `10.3847/1538-4357/ac7d4e`. URL: `https://dx.doi.org/10.3847/1538-4357/ac7d4e`.

Abu-Zayyad, T. et al. (2012). “The surface detector array of the Telescope Array experiment”. In: *Nuclear Instruments and Methods in Physics Research Section A: Accelerators, Spectrometers, Detectors and Associated Equipment* 689, pp. 87–97. ISSN: 0168-9002. DOI: `https://doi.org/10.1016/j.nima.2012.05.079`. URL: `https://www.sciencedirect.com/science/article/pii/S0168900212005931`.

Actis, M et al. (2011). “Design concepts for the Cherenkov Telescope Array CTA: an advanced facility for ground-based high-energy gamma-ray astronomy”. In: *Experimental Astronomy* 32, pp. 193–316.

Adam, J. et al. (2016). “Multiplicity dependence of charged pion, kaon, and (anti)proton production at large transverse momentum in p–Pb collisions at sNN=5.02 TeV”. In: *Physics Letters B* 760, pp. 720–735. ISSN: 0370-2693. DOI: `https://doi.org/10.1016/j.physletb.2016.07.050`. URL: `https://www.sciencedirect.com/science/article/pii/S0370269316303914`.

Adrián-Martínez, S et al. (June 2016). “Letter of intent for KM3NeT 2.0”. In: *Journal of Physics G: Nuclear and Particle Physics* 43.8, p. 084001. DOI: `10.1088/0954-3899/43/8/084001`. URL: `https://dx.doi.org/10.1088/0954-3899/43/8/084001`.

Aguilar, J.A. et al. (Mar. 2021). “Design and sensitivity of the Radio Neutrino Observatory in Greenland (RNO-G)”. In: *Journal of Instrumentation* 16.03, P03025. DOI: `10.1088/1748-0221/16/03/P03025`. URL: `https://dx.doi.org/10.1088/1748-0221/16/03/P03025`.

Aharonian, F. A., S. R. Kelner, and A. Yu. Prosekin (Aug. 2010). “Angular, spectral, and time distributions of highest energy protons and associated secondary gamma rays and neutrinos propagating through extragalactic magnetic and radiation fields”. In: *Phys. Rev. D* 82 (4), p. 043002. DOI: `10.1103/PhysRevD.82.043002`. URL: `https://link.aps.org/doi/10.1103/PhysRevD.82.043002`.

Ahlers, Markus and Francis Halzen (Sept. 2018). “Opening a new window onto the universe with IceCube”. In: *Progress in Particle and Nuclear Physics* 102, pp. 73–88. DOI: `10.1016/j.ppnp.2018.05.001`. URL: `https://doi.org/10.1016%2Fj.ppnp.2018.05.001`.

Ahlers, Markus, Klaus Helbing, and Carlos Pérez de los Heros (Nov. 2018). “Probing particle physics with IceCube”. In: *The European Physical Journal C* 78.11. DOI: `10.1140/epjc/s10052-018-6369-9`. URL: `https://doi.org/10.1140%2Fepjc%2Fs10052-018-6369-9`.

Ajello, M., L. Costamante, et al. (June 2009). “THE EVOLUTION OF SWIFT/BAT BLAZARS AND THE ORIGIN OF THE MeV BACKGROUND”. In: *The Astrophysical Journal* 699.1, p. 603. DOI: `10.1088/0004-637X/699/1/603`. URL: `https://dx.doi.org/10.1088/0004-637X/699/1/603`.

Ajello, M., D. Gasparrini, et al. (Feb. 2015). “THE ORIGIN OF THE EXTRAGALACTIC GAMMA-RAY BACKGROUND AND IMPLICATIONS FOR DARK MATTER ANNIHILATION”. In: *The Astrophysical Journal Letters* 800.2, p. L27. DOI: `10.1088/2041-8205/800/2/L27`. URL: `https://dx.doi.org/10.1088/2041-8205/800/2/L27`.

Ajello, M., J. Greiner, et al. (Dec. 2008). “Cosmic X-Ray Background and Earth Albedo Spectra with Swift BAT”. In: *The Astrophysical Journal* 689.2, p. 666. DOI: `10.1086/592595`. URL: `https://dx.doi.org/10.1086/592595`.

Ajello, M., R. W. Romani, et al. (Dec. 2014). “THE COSMIC EVOLUTION OF FERMI BL LACERTAE OBJECTS”. In: *The Astrophysical Journal* 780.1, p. 73. DOI: `10.1088/0004-637X/780/1/73`. URL: `https://dx.doi.org/10.1088/0004-637X/780/1/73`.

Ajello, M., M. S. Shaw, et al. (May 2012). “THE LUMINOSITY FUNCTION OF FERMI-DETECTED FLAT-SPECTRUM RADIO QUASARS”. In: *The Astrophysical Journal* 751.2, p. 108. DOI: `10.1088/0004-637X/751/2/108`. URL: `https://dx.doi.org/10.1088/0004-637X/751/2/108`.

Andres, Elkin et al. (Apr. 2001). “Observation of high-energy neutrinos using Cerenkov detectors embedded deep in Antarctic ice”. In: *Nature* 410, pp. 441–3. DOI: `10.1038/35068509`.

Antonucci, R. R. J. and J. S. Ulvestad (July 1985). “Extended radio emission and the nature of blazars.” In: 294, pp. 158–182. DOI: `10.1086/163284`.

Asano, K. and S. Nagataki (Mar. 2006). “Very High Energy Neutrinos Originating from Kaons in Gamma-Ray Bursts”. In: *The Astrophysical Journal* 640.1, pp. L9–L12. DOI: `10.1086/503291`. URL: `https://doi.org/10.1086%2F503291`.

Athar, M. Sajjad et al. (May 2022). “Status and perspectives of neutrino physics”. In: *Progress in Particle and Nuclear Physics* 124, p. 103947. DOI: `10.1016/j.ppnp.2022.103947`. URL: `https://doi.org/10.1016%2Fj.ppnp.2022.103947`.

Atwood, W. B. et al. (May 2009). “THE LARGE AREA TELESCOPE ON THE FERMI GAMMA-RAY SPACE TELESCOPE MISSION”. In: *The Astrophysical Journal* 697.2, p. 1071. DOI: `10.1088/0004-637X/697/2/1071`. URL: `https://dx.doi.org/10.1088/0004-637X/697/2/1071`.

Axford, W. I., E. Leer, and G. Skadron (Jan. 1977). “The Acceleration of Cosmic Rays by Shock Waves”. In: *International Cosmic Ray Conference*. Vol. 11. International Cosmic Ray Conference, p. 132.

Bahcall, John N. (Mar. 1964). “Solar Neutrinos. I. Theoretical”. In: *Phys. Rev. Lett.* 12 (11), pp. 300–302. DOI: `10.1103/PhysRevLett.12.300`. URL: `https://link.aps.org/doi/10.1103/PhysRevLett.12.300`.

— (1969). “NEUTRINOS FROM THE SUN”. In: *Scientific American* 221.1, pp. 28–37. ISSN: 00368733, 19467087. URL: `http://www.jstor.org/stable/24926407` (visited on 04/03/2023).

Baldi, Ranieri D. et al. (2019). *The High Energy View of FR0 Radio Galaxies*. arXiv: `1909.04113 [astro-ph.HE]`.

Bambynek, W. et al. (Jan. 1977). “Orbital electron capture by the nucleus”. In: *Rev. Mod. Phys.* 49 (1), pp. 77–221. DOI: `10.1103/RevModPhys.49.77`. URL: `https://link.aps.org/doi/10.1103/RevModPhys.49.77`.

Barthelmy, Scott D et al. (2005). “The burst alert telescope (BAT) on the SWIFT midex mission”. In: *Space Science Reviews* 120, pp. 143–164.

Beckmann, Volker and Chris R. Shrader (2013). *The AGN phenomenon: open issues*. arXiv: `1302.1397 [astro-ph.HE]`.

Bell, A. R. (Feb. 1978). “The acceleration of cosmic rays in shock fronts – I”. In: *Monthly Notices of the Royal Astronomical Society* 182.2, pp. 147–156. ISSN: 0035-8711. DOI: `10.1093/mnras/182.2.147`. eprint: `https://academic.oup.com/mnras/article-pdf/182/2/147/3710138/mnras182-0147.pdf`. URL: `https://doi.org/10.1093/mnras/182.2.147`.

Bethe, H. and W. Heitler (1934). “On the Stopping of Fast Particles and on the Creation of Positive Electrons”. In: *Proceedings of the Royal Society of London. Series A, Containing Papers of a Mathematical and Physical Character* 146.856, pp. 83–112. ISSN: 09501207. URL: `http://www.jstor.org/stable/2935479` (visited on 03/29/2023).

Bhattacharjee, Pijushpani and Günter Sigl (Apr. 2000). “Origin and propagation of extremely high-energy cosmic rays”. In: *Physics Reports* 327.3-4, pp. 109–247. DOI: `10.1016/s0370-1573(99)00101-5`. URL: `https://doi.org/10.1016%2Fs0370-1573%2899%2900101-5`.

Biteau, Jonathan and Manuel Meyer (Feb. 2022). “Gamma-Ray Cosmology and Tests of Fundamental Physics”. In: *Galaxies* 10.2, p. 39. DOI: `10.3390/galaxies10020039`. URL: `https://doi.org/10.3390%2Fgalaxies10020039`.

Blandford, R. D. and A. Königl (Aug. 1979). “Relativistic jets as compact radio sources.” In: 232, pp. 34–48. DOI: `10.1086/157262`.

Blandford, R. D. and R. L. Znajek (July 1977). “Electromagnetic extraction of energy from Kerr black holes”. In: *Monthly Notices of the Royal Astronomical Society* 179.3, pp. 433–456. ISSN: 0035-8711. DOI: `10.1093/mnras/179.3.433`. eprint: `https://academic.oup.com/mnras/article-pdf/179/3/433/9333653/mnras179-0433.pdf`. URL: `https://doi.org/10.1093/mnras/179.3.433`.

Blasi, P., R. I. Epstein, and A. V. Olinto (Apr. 2000). “Ultra-High-Energy Cosmic Rays from Young Neutron Star Winds”. In: *The Astrophysical Journal* 533.2, p. L123. DOI: `10.1086/312626`. URL: `https://dx.doi.org/10.1086/312626`.

Collaboration, The IceCube et al. (2018). “Multimessenger observations of a flaring blazar coincident with high-energy neutrino IceCube-170922A”. In: *Science* 361.6398, eaat1378. DOI: `10.1126/science.aat1378`. eprint: `https://www.science.org/doi/pdf/10.1126/science.aat1378`. URL: `https://www.science.org/doi/abs/10.1126/science.aat1378`.

Collaboration, The Pierre Auger et al. (2023). *Constraining the sources of ultra-high-energy cosmic rays across and above the ankle with the spectrum and composition data measured at the Pierre Auger Observatory.* arXiv: `2211.02857 [astro-ph.HE]`.

Collaboration*, IceCube (2013). “Evidence for High-Energy Extraterrestrial Neutrinos at the IceCube Detector”. In: *Science* 342.6161, p. 1242856. DOI: `10.1126/science.1242856`. eprint: `https://www.science.org/doi/pdf/10.1126/science.1242856`. URL: `https://www.science.org/doi/abs/10.1126/science.1242856`.

Cowan C. L., Jr. et al. (July 1956). “Detection of the Free Neutrino: A Confirmation”. In: *Science* 124.3212, pp. 103–104. DOI: `10.1126/science.124.3212.103`.

Dado, Shlomo and Arnon Dar (May 2015). “Common Solution Of Three Cosmic Puzzles”. In.

Deil, C. et al. (Jan. 2017). “Gammapy - A prototype for the CTA science tools”. In: *35th International Cosmic Ray Conference (ICRC2017).* Vol. 301. International Cosmic Ray Conference, 766, p. 766. arXiv: `1709.01751 [astro-ph.IM]`.

Dermer, Charles D., Justin D. Finke, et al. (Feb. 2009). "GAMMA-RAY STUDIES OF BLAZARS: SYNCHRO-COMPTON ANALYSIS OF FLAT SPECTRUM RADIO QUASARS". In: *The Astrophysical Journal* 692.1, pp. 32–46. DOI: `10.1088/0004-637x/692/1/32`. URL: `https://doi.org/10.1088%2F0004-637x%2F692%2F1%2F32`.

Dermer, Charles D. and Govind Menon (2009). *High energy radiation from black holes.* Prinston University Press.

Du, Pu et al. (June 2015). "SUPERMASSIVE BLACK HOLES WITH HIGH ACCRETION RATES IN ACTIVE GALACTIC NUCLEI. IV. H TIME LAGS AND IMPLICATIONS FOR SUPER-EDDINGTON ACCRETION". In: *The Astrophysical Journal* 806.1, p. 22. DOI: `10.1088/0004-637X/806/1/22`. URL: `https://dx.doi.org/10.1088/0004-637X/806/1/22`.

Dunlop, J. S. et al. (Apr. 2003). "Quasars, their host galaxies and their central black holes". In: *Monthly Notices of the Royal Astronomical Society* 340.4, pp. 1095–1135. ISSN: 0035-8711. DOI: `10.1046/j.1365-8711.2003.06333.x`. eprint: `https://academic.oup.com/mnras/article-pdf/340/4/1095/4146137/340-4-1095.pdf`. URL: `https://doi.org/10.1046/j.1365-8711.2003.06333.x`.

Eales, Stephen Anthony (1985). "A sample of 6C radio sources selected at the peak of the source counts–I. A search for extended sources and multifrequency radio observations". In: *Monthly Notices of the Royal Astronomical Society* 217.1, pp. 149–166.

Eddington, A. S. (Mar. 1925). "On the Mass-Luminosity Relation; a reply to Dr. Jeans". In: *Monthly Notices of the Royal Astronomical Society* 85.5, pp. 403–408. ISSN: 0035-8711. DOI: `10.1093/mnras/85.5.403`. URL: `https://doi.org/10.1093/mnras/85.5.403`.

Fanaroff, B. L. and J. M. Riley (Apr. 1974). "The Morphology of Extragalactic Radio Sources of High and Low Luminosity". In: *Monthly Notices of the Royal Astronomical Society* 167.1, 31P–36P. ISSN: 0035-8711. DOI: `10.1093/mnras/167.1.31P`. eprint: `https://academic.oup.com/mnras/article-pdf/167/1/31P/8079923/mnras167-031P.pdf`. URL: `https://doi.org/10.1093/mnras/167.1.31P`.

Fang, Ke, Kumiko Kotera, Kohta Murase, et al. (Apr. 2016). "IceCube constraints on fast-spinning pulsars as high-energy neutrino sources". In: *Journal of Cosmology and Astroparticle Physics* 2016.04, p. 010. DOI: `10.1088/1475-7516/2016/04/010`. URL: `https://dx.doi.org/10.1088/1475-7516/2016/04/010`.

Fang, Ke, Kumiko Kotera, and Angela V. Olinto (Apr. 2012). "NEWLY BORN PULSARS AS SOURCES OF ULTRAHIGH ENERGY COSMIC RAYS". In: *The Astrophysical Journal* 750.2, p. 118. DOI: `10.1088/0004-637X/750/2/118`. URL: `https://dx.doi.org/10.1088/0004-637X/750/2/118`.

Farzan, Yasaman and Alexei Yu. Smirnov (Dec. 2008). "Coherence and oscillations of cosmic neutrinos". In: *Nuclear Physics B* 805.1-2, pp. 356–376. DOI: `10.1016/j.nuclphysb.2008.07.028`. URL: `https://doi.org/10.1016%2Fj.nuclphysb.2008.07.028`.

Finke, Justin D. (Oct. 2016). “EXTERNAL COMPTON SCATTERING IN BLAZAR JETS AND THE LOCATION OF THE GAMMA-RAY EMITTING REGION”. In: *The Astrophysical Journal* 830.2, p. 94. DOI: `10.3847/0004-637X/830/2/94`. URL: `https://dx.doi.org/10.3847/0004-637X/830/2/94`.

Finke, Justin D., Charles D. Dermer, and Markus Böttcher (Oct. 2008). “Synchrotron Self-Compton Analysis of TeV X-Ray-Selected BL Lacertae Objects”. In: 686.1, pp. 181–194. DOI: `10.1086/590900`. arXiv: `0802.1529 [astro-ph]`.

Fixsen, D. J. (Nov. 2009). “THE TEMPERATURE OF THE COSMIC MICROWAVE BACKGROUND”. In: *The Astrophysical Journal* 707.2, p. 916. DOI: `10.1088/0004-637X/707/2/916`. URL: `https://dx.doi.org/10.1088/0004-637X/707/2/916`.

Fukazawa, Yasushi et al. (June 2022). “High-energy Emission Component, Population, and Contribution to the Extragalactic Gamma-Ray Background of Gamma-Ray-emitting Radio Galaxies”. In: *The Astrophysical Journal* 931.2, p. 138. DOI: `10.3847/1538-4357/ac6acb`. URL: `https://dx.doi.org/10.3847/1538-4357/ac6acb`.

Fukuda, S. et al. (2003). “The Super-Kamiokande detector”. In: *Nuclear Instruments and Methods in Physics Research Section A: Accelerators, Spectrometers, Detectors and Associated Equipment* 501.2, pp. 418–462. ISSN: 0168-9002. DOI: `https://doi.org/10.1016/S0168-9002(03)00425-X`. URL: `https://www.sciencedirect.com/science/article/pii/S016890020300425X`.

Gaisser, T. K. et al. (Oct. 1978). “Cosmic ray showers and particle physics at energies 10^{15}-10^{18} eV”. In: *Rev. Mod. Phys.* 50 (4), pp. 859–880. DOI: `10.1103/RevModPhys.50.859`. URL: `https://link.aps.org/doi/10.1103/RevModPhys.50.859`.

Gehrels, N. et al. (Aug. 2004). “The Swift Gamma-Ray Burst Mission”. In: *The Astrophysical Journal* 611.2, p. 1005. DOI: `10.1086/422091`. URL: `https://dx.doi.org/10.1086/422091`.

Ghisellini, G., R. Della Ceca, et al. (June 2010). “Chasing the heaviest black holes of jetted active galactic nuclei”. In: *Monthly Notices of the Royal Astronomical Society* 405.1, pp. 387–400. ISSN: 0035-8711. DOI: `10.1111/j.1365-2966.2010.16449.x`. eprint: `https://academic.oup.com/mnras/article-pdf/405/1/387/3369181/mnras0405-0387.pdf`. URL: `https://doi.org/10.1111/j.1365-2966.2010.16449.x`.

Ghisellini, G., A. Celotti, et al. (Dec. 1998). “A theoretical unifying scheme for gamma-ray bright blazars”. In: *Monthly Notices of the Royal Astronomical Society* 301.2, pp. 451–468. ISSN: 0035-8711. DOI: `10.1046/j.1365-8711.1998.02032.x`. URL: `https://doi.org/10.1046/j.1365-8711.1998.02032.x`.

Ghisellini, G. and F. Tavecchio (Aug. 2009). “Canonical high-power blazars”. In: *Monthly Notices of the Royal Astronomical Society* 397.2, pp. 985–1002. DOI: `10.1111/j.1365-2966.2009.15007.x`. URL: `https://doi.org/10.1111%2Fj.1365-2966.2009.15007.x`.

Ghisellini, Gabriele et al. (2014). “The power of relativistic jets is larger than the luminosity of their accretion disks”. In: *Nature* 515.7527, pp. 376–378.

Ghisellini, G., Haardt, F., and Matt, G. (2004). “Aborted jets and the X-ray emission of radio-quiet AGNs”. In: *A&A* 413.2, pp. 535–545. DOI: `10.1051/0004-6361:20031562`. URL: `https://doi.org/10.1051/0004-6361:20031562`.

Greisen, Kenneth (Apr. 1966). “End to the Cosmic-Ray Spectrum?” In: *Phys. Rev. Lett.* 16 (17), pp. 748–750. DOI: `10.1103/PhysRevLett.16.748`. URL: `https://link.aps.org/doi/10.1103/PhysRevLett.16.748`.

Guérard, C. K. (Jan. 1999). “The Auger project and the detection of UHECRs”. In: *Vulcano Workshop 1998: Frontier Objects in Astrophysics and Particle Physics.* Ed. by F. Giovannelli and G. Mannocchi. Vol. 65, p. 485.

Gunn, James E. and Jeremiah P. Ostriker (Apr. 1969). “Acceleration of High-Energy Cosmic Rays by Pulsars”. In: *Phys. Rev. Lett.* 22 (14), pp. 728–731. DOI: `10.1103/PhysRevLett.22.728`. URL: `https://link.aps.org/doi/10.1103/PhysRevLett.22.728`.

Harrison, C. M. (2017). *Impact of supermassive black hole growth on star formation.* arXiv: `1703.06889 [astro-ph.GA]`.

Heckman, Timothy M. and Philip N. Best (Aug. 2014). “The Coevolution of Galaxies and Supermassive Black Holes: Insights from Surveys of the Contemporary Universe”. In: *Annual Review of Astronomy and Astrophysics* 52.1, pp. 589–660. DOI: `10.1146/annurev-astro-081913-035722`. URL: `https://doi.org/10.1146%2Fannurev-astro-081913-035722`.

Hill, Ryley, Kiyoshi W. Masui, and Douglas Scott (Apr. 2018). “The Spectrum of the Universe”. In: *Applied Spectroscopy* 72.5, pp. 663–688. DOI: `10.1177/0003702818767133`. URL: `https://doi.org/10.1177%2F0003702818767133`.

Hillas, A. M. (Jan. 1984). “The Origin of Ultra-High-Energy Cosmic Rays”. In: 22, pp. 425–444. DOI: `10.1146/annurev.aa.22.090184.002233`.

Hogg, David W. (2000). *Distance measures in cosmology.* arXiv: `astro-ph/9905116 [astro-ph]`.

Jacobsen, Idunn Blindheim (2015). “Spectra of High-Energy Neutrinos and AGN Population Evolution inferred by X-ray/γ-ray Surveys”. PhD thesis. University College London. URL: `https://discovery.ucl.ac.uk/id/eprint/1471526/`.

James, Fred and Matts Roos (1975). “MINUIT: a system for function minimization and analysis of the parameter errors and corrections”. In: *Comput. Phys. Commun.* 10.CERN-DD-75-20, pp. 343–367.

Kachelriess, M. (2008). *Lecture notes on high energy cosmic rays.* arXiv: `0801.4376 [astro-ph]`.

Kachelrieß, M. (2019). “Transition from Galactic to Extragalactic Cosmic Rays”. In: *EPJ Web Conf.* 210, p. 04003. DOI: `10.1051/epjconf/201921004003`. URL: `https://doi.org/10.1051/epjconf/201921004003`.

Kampert, Karl-Heinz and Michael Unger (2012). “Measurements of the cosmic ray composition with air shower experiments”. In: *Astroparticle Physics* 35.10, pp. 660–678. ISSN: 0927-6505. DOI: `https://doi.org/10.1016/j.astropartphys.2012.02.004`. URL: `https://www.sciencedirect.com/science/article/pii/S0927650512000382`.

Karachentsev, I. D. (Jan. 2005). “The Local Group and Other Neighboring Galaxy Groups*”. In: *The Astronomical Journal* 129.1, p. 178. DOI: `10.1086/426368`. URL: `https://dx.doi.org/10.1086/426368`.

Kelner, S. R. and F. A. Aharonian (Aug. 2008). “Energy spectra of gamma rays, electrons, and neutrinos produced at interactions of relativistic protons with low energy radiation”. In: *Phys. Rev. D* 78 (3), p. 034013. DOI: `10.1103/PhysRevD.78.034013`. URL: `https://link.aps.org/doi/10.1103/PhysRevD.78.034013`.

Kishimoto, Makoto et al. (2007). “The innermost region of AGN tori: implications from the HST/NICMOS type 1 point sources and near-IR reverberation”. In: *Astronomy & Astrophysics* 476.2, pp. 713–721.

Kotera, Kumiko and Angela V. Olinto (2011). “The Astrophysics of Ultrahigh-Energy Cosmic Rays”. In: *Annual Review of Astronomy and Astrophysics* 49.1, pp. 119–153. DOI: `10.1146/annurev-astro-081710-102620`. eprint: `https://doi.org/10.1146/annurev-astro-081710-102620`. URL: `https://doi.org/10.1146/annurev-astro-081710-102620`.

Krane, Kenneth S. (1988). *Introduction to Nuclear Physics.* John Wiley & Sons.

Lacy, Mark et al. (Oct. 1999). “Optical spectroscopy of two overlapping, flux-density-limited samples of radio sources in the North Ecliptic Cap, selected at 38 and 151 MHz”. In: *Monthly Notices of the Royal Astronomical Society* 308.4, pp. 1096–1116. ISSN: 0035-8711. DOI: `10.1046/j.1365-8711.1999.02790.x`. eprint: `https://academic.oup.com/mnras/article-pdf/308/4/1096/3428795/308-4-1096.pdf`. URL: `https://doi.org/10.1046/j.1365-8711.1999.02790.x`.

Laing, RA, JM Riley, and MS Longair (1983). “Bright radio sources at 178 MHz-Flux densities, optical identifications and the cosmological evolution of powerful radio galaxies”. In: *Monthly Notices of the Royal Astronomical Society* 204, pp. 151–187.

Lichtenberg, A.J., M.A. Lieberman, and R.H. Cohen (1980). “Fermi acceleration revisited”. In: *Physica D: Nonlinear Phenomena* 1.3, pp. 291–305. ISSN: 0167-2789. DOI: `https://doi.org/10.1016/0167-2789(80)90027-5`. URL: `https://www.sciencedirect.com/science/article/pii/0167278980900275`.

Longair, Malcolm S. (2011). *High Energy Astrophysics.* Cambridge University Press.

Maiolino, R. and G. H. Rieke (Nov. 1995). “Low-Luminosity and Obscured Seyfert Nuclei in Nearby Galaxies”. In: 454, p. 95. DOI: `10.1086/176468`.

Malesani, D. B. et al. (2023). *The brightest GRB ever detected: GRB 221009A as a highly luminous event at z = 0.151.* arXiv: `2302.07891 [astro-ph.HE]`.

Marcotulli, L. et al. (Nov. 2022). “BASS. XXXIII. Swift-BAT Blazars and Their Jets through Cosmic Time”. In: *The Astrophysical Journal* 940.1, p. 77. DOI: `10.3847/1538-4357/ac937f`.

Murase, Kohta and Masataka Fukugita (Mar. 2019). “Energetics of high-energy cosmic radiations”. In: *Phys. Rev. D* 99 (6), p. 063012. DOI: `10.1103/PhysRevD.99.063012`. URL: `https://link.aps.org/doi/10.1103/PhysRevD.99.063012`.

Nigro, C. et al. (2022). “agnpy: An open-source python package modelling the radiative processes of jetted active galactic nuclei”. In: *A&A* 660, A18. DOI: `10.1051/0004-6361/202142000`. URL: `https://doi.org/10.1051/0004-6361/202142000`.

Norman, Colin A., Donald B. Melrose, and Abraham Achterberg (Nov. 1995). “The Origin of Cosmic Rays above 10 18.5 eV”. In: 454, p. 60. DOI: `10.1086/176465`.

Oikonomou, Foteini (2022). “High-energy neutrino emission from blazars”. In: *PoS* ICRC2021, p. 030. DOI: `10.22323/1.395.0030`. arXiv: `2201.05623 [astro-ph.HE]`.

Palladino, Andrea et al. (Apr. 2020). “Can astrophysical neutrinos trace the origin of the detected ultra-high energy cosmic rays?” In: *Monthly Notices of the Royal Astronomical Society* 494.3, pp. 4255–4265. ISSN: 0035-8711. DOI: `10.1093/mnras/staa1003`. eprint: `https://academic.oup.com/mnras/article-pdf/494/3/4255/33155582/staa1003.pdf`. URL: `https://doi.org/10.1093/mnras/staa1003`.

Peterson, Bradley M. and Amri Wandel (Aug. 1999). “Keplerian Motion of Broad-Line Region Gas as Evidence for Supermassive Black Holes in Active Galactic Nuclei”. In: *The Astrophysical Journal* 521.2, pp. L95–L98. DOI: `10.1086/312190`. URL: `https://doi.org/10.1086%2F312190`.

Potter, William J. and Garret Cotter (May 2012). “Synchrotron and inverse-Compton emission from blazar jets – I. A uniform conical jet model”. In: *Monthly Notices of the Royal Astronomical Society* 423.1, pp. 756–765. ISSN: 0035-8711. DOI: `10.1111/j.1365-2966.2012.20918.x`. eprint: `https://academic.oup.com/mnras/article-pdf/423/1/756/18611634/mnras0423-0756.pdf`. URL: `https://doi.org/10.1111/j.1365-2966.2012.20918.x`.

Radecke, H.-D and G. Kanbach (1992). “The Egret High Energy Gamma Ray Telescope on GRO: Instrument Description and Scientific Mission”. In: *Data Analysis in Astronomy IV*. Ed. by V. Di Gesù et al. Boston, MA: Springer US, pp. 303–310. ISBN: 978-1-4615-3388-7. DOI: `10.1007/978-1-4615-3388-7_31`. URL: `https://doi.org/10.1007/978-1-4615-3388-7_31`.

Romero, Gustavo E et al. (2017). “Relativistic jets in active galactic nuclei and microquasars”. In: *Space Science Reviews* 207, pp. 5–61.

Schechter, P. (Jan. 1976). “An analytic expression for the luminosity function for galaxies.” In: 203, pp. 297–306. DOI: `10.1086/154079`.

Schwetz, Thomas, Mariam Tórtola, and José W F Valle (Nov. 2008). “Three-flavour neutrino oscillation update”. In: *New Journal of Physics* 10.11, p. 113011. DOI: `10.1088/1367-2630/10/11/113011`. URL: `https://dx.doi.org/10.1088/1367-2630/10/11/113011`.

Shakura, N. I. and R. A. Sunyaev (1973). “Black Holes in Binary Systems: Observational Appearances”. In: *Symposium - International Astronomical Union* 55, pp. 155–164. DOI: `10.1017/S007418090010035X`.

Silverman, J. D. et al. (May 2008). “The Luminosity Function of X-Ray–selected Active Galactic Nuclei: Evolution of Supermassive Black Holes at High Redshift”. In: *The Astrophysical Journal* 679.1, pp. 118–139. DOI: `10.1086/529572`.

Singh, V., P. Shastri, and G. Risaliti (July 2011). “X-ray spectral properties of Seyfert galaxies and the unification scheme”. In: *Astronomy &amp Astrophysics* 532, A84. DOI: `10.1051/0004-6361/201016387`. URL: `https://doi.org/10.1051%2F0004-6361%2F201016387`.

Spiering, Christian (July 2012). “Towards high-energy neutrino astronomy”. In: *The European Physical Journal H* 37.3, pp. 515–565. DOI: `10.1140/epjh/e2012-30014-2`. URL: `https://doi.org/10.1140%2Fepjh%2Fe2012-30014-2`.

Springel, Volker, Carlos S. Frenk, and Simon D. M. White (Apr. 2006). “The large-scale structure of the Universe”. In: *Nature* 440.7088, pp. 1137–1144. DOI: `10.1038/nature04805`. URL: `https://doi.org/10.1038%2Fnature04805`.

Stecker, F. W. and M. H. Salamon (Feb. 1999). “Photodisintegration of Ultra-High-Energy Cosmic Rays: A New Determination”. In: *The Astrophysical Journal* 512.2, p. 521. DOI: `10.1086/306816`. URL: `https://dx.doi.org/10.1086/306816`.

Tadhunter, Clive (2008). “An introduction to active galactic nuclei: Classification and unification”. In: *New Astronomy Reviews* 52.6. Active Galactic Nuclei at the Highest Angular Resolution: Theory and Observations, pp. 227–239. ISSN: 1387-6473. DOI: `https://doi.org/10.1016/j.newar.2008.06.004`. URL: `https://www.sciencedirect.com/science/article/pii/S1387647308001012`.

Tchekhovskoy, Alexander, Ramesh Narayan, and Jonathan C. McKinney (Nov. 2011). “Efficient generation of jets from magnetically arrested accretion on a rapidly spinning black hole”. In: *Monthly Notices of the Royal Astronomical Society: Letters* 418.1, pp. L79–L83. ISSN: 1745-3925. DOI: `10.1111/j.1745-3933.2011.01147.x`. eprint: `https://academic.oup.com/mnrasl/article-pdf/418/1/L79/6418189/418-1-L79.pdf`. URL: `https://doi.org/10.1111/j.1745-3933.2011.01147.x`.

“The Pierre Auger Cosmic Ray Observatory” (2015). In: *Nuclear Instruments and Methods in Physics Research Section A: Accelerators, Spectrometers, Detectors and Associated Equipment* 798, pp. 172–213. ISSN: 0168-9002. DOI: `https://doi.org/10.1016/j.nima.2015.06.058`. URL: `https://www.sciencedirect.com/science/article/pii/S0168900215008086`.

Ueda, Yoshihiro et al. (Dec. 2003). “Cosmological Evolution of the Hard X-Ray Active Galactic Nucleus Luminosity Function and the Origin of the Hard X-Ray Background”. In: *The Astrophysical Journal* 598.2, p. 886. DOI: `10.1086/378940`. URL: `https://dx.doi.org/10.1086/378940`.

Unger, Michael, Glennys R. Farrar, and Luis A. Anchordoqui (Dec. 2015). “Origin of the ankle in the ultrahigh energy cosmic ray spectrum, and of the extragalactic protons below it”. In: *Physical Review D* 92.12. DOI: `10.1103/physrevd.92.123001`.

Urry, C (2004). “AGN Unification: An Update”. In: *AGN Physics with the Sloan Digital Sky Survey*. Vol. 311, p. 49.

Urry, C. M. and P. Padovani (Apr. 1991). “Altered Luminosity Functions for Relativistically Beamed Objects. II. Distribution of Lorentz Factors and Parent Populations with Complex Luminosity Functions”. In: 371, p. 60. DOI: `10.1086/169870`.

Urry, C. M. and R. A. Shafer (May 1984). “Luminosity enhancement in relativistic jets and altered luminosity functions for beamed objects”. In: 280, pp. 569–573. DOI: `10.1086/162027`.

Urry, C. Megan and Paolo Padovani (Sept. 1995). “Unified Schemes for Radio-Loud Active Galactic Nuclei”. In: *Publications of the Astronomical Society of the Pacific* 107, p. 803. DOI: `10.1086/133630`. URL: `https://doi.org/10.1086%2F133630`.

Waxman, Eli and John Bahcall (Dec. 1998). “High energy neutrinos from astrophysical sources: An upper bound”. In: *Physical Review D* 59.2. DOI: `10.1103/physrevd.59.023002`. URL: `https://doi.org/10.1103%2Fphysrevd.59.023002`.

Weisskopf, M. C. et al. (Jan. 2002). “An Overview of the Performance and Scientific Results from the Chandra X-Ray Observatory”. In: *Publications of the Astronomical Society of the Pacific* 114.791, p. 1. DOI: `10.1086/338108`. URL: `https://dx.doi.org/10.1086/338108`.

Willott, C. J. et al. (Apr. 2001). “The radio luminosity function from the low-frequency 3CRR, 6CE and 7CRS complete samples”. In: *Monthly Notices of the Royal Astronomical Society* 322.3, pp. 536–552. DOI: `10.1046/j.1365-8711.2001.04101.x`.

Willott, Chris J. et al. (Oct. 2002). “Optical spectroscopy of radio galaxies in the 7C Redshift Survey”. In: *Monthly Notices of the Royal Astronomical Society* 335.4, pp. 1120–1132. ISSN: 0035-8711. DOI: `10.1046/j.1365-8711.2002.05718.x`. eprint: `https://academic.oup.com/mnras/article-pdf/335/4/1120/2856915/335-4-1120.pdf`. URL: `https://doi.org/10.1046/j.1365-8711.2002.05718.x`.

Workman, R. L. et al. (2022). “Review of Particle Physics”. In: *PTEP* 2022, p. 083C01. DOI: `10.1093/ptep/ptac097`.

Yüksel, Hasan et al. (July 2008). “Revealing the High-Redshift Star Formation Rate with Gamma-Ray Bursts”. In: *The Astrophysical Journal* 683.1, p. L5. DOI: `10.1086/591449`. URL: `https://dx.doi.org/10.1086/591449`.

Zatsepin, G. T. and V. A. Kuz’min (Aug. 1966). “Upper Limit of the Spectrum of Cosmic Rays”. In: *Soviet Journal of Experimental and Theoretical Physics Letters* 4, p. 78.

Zweibel, Ellen G. (2013). “The microphysics and macrophysics of cosmic rays”. In: *Physics of Plasmas* 20.5, p. 055501. DOI: `10.1063/1.4807033`. URL: `https://doi.org/10.1063/1.4807033`.

NTNU

Norwegian University of
Science and Technology